Inaugural dissertation
for
obtaining the doctoral degree
of the
Combined Faculty of Mathematics, Engineering and Natural Sciences
of the
Ruprecht – Karls – University
Heidelberg

Presented by

M.Sc. Lena Olivia Thiess

born in: Heidelberg

Oral examination: 13th of June 2023

Dysregulation of junctional proteins controls Hippo/YAP pathway activity *via* specific mechanisms in liver cancer

Referees: Prof. Dr. Peter Angel

Prof. Dr. Kai Breuhahn

Table of Contents

Summary

Cell-cell connections, in part mediated by adherens junctions, play an important role in the formation of cell polarity and tissue homeostasis. Their dysregulation is associated with the development of several diseases, including cancer formation. Exemplary, the function of liver hepatocytes strictly depends on a high degree of spatial organization and disturbance of hepatocellular polarity is a key feature in hepatocarcinogenesis. Indeed, hepatocellular carcinoma (HCC) is characterized by limited treatment options, illustrating the urgent need to identify novel target structures to improve diagnostics and the development of therapeutic strategies for HCC patients. A frequently dysregulated pathway in HCC is the cell-cell contact-sensing and organ size-controlling Hippo/yes-associated protein (YAP) signaling cascade. Regarding Hippo/YAP pathway, it has been demonstrated that junctional proteins like E-cadherin can influence its activity with direct impact on tumor formation. However, it is unknown if Hippo/YAP unspecifically responds to any kind of cell contact alteration or if specific molecular mechanisms connect the aberrant expression of junctional proteins with this pathway.

To identify junctional structures which are aberrantly expressed in HCC, and which may control the Hippo/YAP signaling cascade, I systematically screened expression data derived from human HCC patient cohorts. Based on clinical (e.g., patient survival) and molecular (e.g., correlation with YAP target genes) selection parameters, five junctional candidates were identified including the desmoglein 1 (DSG1), desmoglein 2 (DSG2) and vasodilator stimulated phosphoprotein (VASP). Induction (DSG2, VASP) and reduction (DSG1) in HCCs compared to non-malignant livers was confirmed in independent cohorts and by different techniques (e.g., immunofluorescence). While DSG1 does not affect HCC cell biology, silencing of DSG2 and VASP by RNA*interference* in HCC cell lines revealed that these proteins support HCC cell viability and proliferation, as well as migration and invasion. Subsequent hydrodynamic gene delivery experiments disclosed that DSG2 and VASP do not act as liver oncogenes in this experimental setup. According to my working hypothesis, YAP abundance and activity is affected by DSG2 and VASP: while DSG2 supports the accumulation of YAP in HCC cells, VASP reduces YAP phosphorylation, which is associated with its activation. To further investigate how dysregulated DSG2 and VASP affect YAP activity, I applied the unbiased BioID approach, followed by mass spectrometry, to identify exclusive DSG2 or VASP interaction partners. Confirmatory, co-immunoprecipitation and proximity ligation experiments demonstrated that VASP directly binds YAP, while DSG2 interacts with the Hippo pathway constituents neurofibromin 2 (NF2, synonym: Merlin) and large tumor suppressor kinase 2 (LATS2).

This study shows that altered expression of adherens junction constituents in liver cancer contribute to the aberrant activity of cancer-relevant signaling as illustrated for the Hippo/YAP pathway. Distinct molecular processes control YAP activity after DSG2 and VASP dysregulation with impact of pro-tumorigenic features for HCC cells. My study not only identifies DSG2 and VASP as potential biomarkers for HCC patients that are characterized by YAP activation and poor clinical outcome, but also broadens the view on how cell-cell contact structures transmit information into cell under pathological conditions.

Zusammenfassung

Zell-Zell-Verbindungen, welche unter anderem durch Adherens Junctions vermittelt werden, spielen eine wichtige Rolle bei der Ausbildung von Zellpolarität und Gewebehomöostase. Fehlregulierung dieser Verbindungen wird mit der Entstehung verschiedener Krankheiten in Verbindung gebracht, darunter auch der Entstehung von Krebs. So hängt beispielsweise die Funktion der Leber Hepatozyten von deren hohen Maß an räumlicher Organisation ab und eine Störung dieser Polarität stellt ein Schlüsselmerkmal bei der Hepatokarzinogenese dar. Das hepatozelluläre Karzinom (HCC) ist durch begrenzte Behandlungsmöglichkeiten gekennzeichnet. Das verdeutlicht die dringende Notwendigkeit neue Zielstrukturen zu identifizieren, um die Diagnostik und die Entwicklung von Therapiestrategien für HCC-Patienten zu verbessern. Ein häufig fehlregulierter Signalweg in HCC ist der Hippo/YAP-Signalweg. Hier wurde nachgewiesen, dass Zellkontaktproteine wie E-Cadherin dessen Aktivität beeinflussen können, was sich direkt auf die Tumorbildung auswirkt. Es ist jedoch unbekannt, ob Hippo/YAP unspezifisch auf jede Art von Veränderungen der Zellkontakte reagiert oder ob spezifische molekulare Mechanismen die fehlregulierte Expression von Zellkontaktproteinen mit diesem Signalweg verbinden.

Um funktionelle Zellkontakt-Strukturen zu identifizieren die in HCC abnormal exprimiert werden und die möglicherweise die Hippo/YAP-Signalkaskade regulieren, habe ich systematisch humane HCC-Expressionsdaten untersucht. Auf der Grundlage von klinischen (z. B. Überleben der Patienten) und molekularen (z. B. Korrelation mit YAP-Zielgenen) Auswahlparametern habe ich fünf Kandidaten identifiziert, darunter Desmoglein 1 (DSG1), Desmoglein 2 (DSG2) und vasodilator-stimuliertes Phosphoprotein (VASP). Die Induktion (DSG2, VASP) und Reduktion (DSG1) der Kandidaten in HCCs im Vergleich zu nicht-malignen Lebern wurde in unabhängigen Kohorten und mit verschiedenen Techniken bestätigt. Während DSG1 keinen Einfluss auf die Biologie von HCC-Zellen hat, zeigte die Inhibierung von DSG2 und VASP durch RNA-Interferenz, dass diese Proteine die Vitalität und die Proliferation sowie die Migration und Invasion von HCC-Zellen unterstützen. Anschließende hydrodynamischen Genverabreichung in Mäuse ergab, dass DSG2 und VASP in diesem Versuchsaufbau nicht als Leber-Onkogene wirken. Meine Arbeitshypothese besagt, dass die Häufigkeit und Aktivität von YAP durch DSG2 und VASP beeinflusst wird: Während DSG2 die Akkumulation von YAP in HCC-Zellen fördert, reduziert VASP die YAP-Phosphorylierung, welche mit seiner Aktivierung korreliert. Um weiter zu untersuchen, wie sich fehlreguliertes DSG2 und VASP auf die YAP-Aktivität auswirken, verwendete ich die BioID Methode gefolgt von Massenspektrometrie, um exklusive DSG2- oder VASP-Interaktionspartner zu identifizieren. Bestätigende Co-Immunpräzipitation und der ‚Proximity Ligation Assay' zeigten, dass VASP direkt

an YAP bindet, während DSG2 mit den Hippo/YAP-Regulatoren Neurofibromin 2 (NF2, Synonym: Merlin) und Large Tumor Suppressor Kinase 2 (LATS2) interagiert.

Diese Studie zeigt, dass eine veränderte Expression von Bestandteilen der Zellkontakte in Leberkrebs zur abweichenden Aktivität krebsrelevanter Signalwege beiträgt, wie dies für den Hippo/YAP-Signalweg dargestellt wird. Unterschiedliche molekulare Prozesse steuern die YAP-Aktivität nach einer DSG2- und VASP-Fehlregulierung mit Auswirkungen auf pro-tumorigene Eigenschaften von HCC-Zellen. Meine Studie identifiziert nicht nur DSG2 und VASP als potenzielle Biomarker für HCC-Patienten, welche durch YAP-Aktivierung und schlechte Prognose gekennzeichnet sind, sondern erweitert auch die Sichtweise darauf, wie Zell-Zell-Kontaktstrukturen unter pathologischen Bedingungen Informationen in die Zelle übertragen.

1 Introduction

1.1 Cell junctions

1.1.1 Cell junctions - Types and function

The formation of contacts between neighboring cells and cells and extracellular matrix (ECM) is essential for the development, the architectonic stabilization and the function of complex tissues, like epithelia. In principle, cell-cell contacts are formed by four distinct major types of cell junctions (figure 1): tight junctions (TJs), adherens junctions (AJs), desmosomes and gap junctions (GJs). While the first three junctional structures facilitate properties that allow cell attachment, the last group serves mainly for communication and only contributes to adhesion marginally [1] [2].

Tight junctions

The subapical TJs (or *Zonulae occludentes*) are formed by the transmembrane proteins occludin, claudin, junctional adhesion molecule (JAM) and several associated cytoplasmic adaptor proteins (figure 1). They exclusively appear in epithelial and endothelial cells, where they form homotypic interacting transmembrane protein complexes between neighboring cells and thereby control paracellular transport and passive flow of ions and solutes [1]. Next to this so-called 'gate-function', TJs also contribute to the maintenance of cell polarity since they prevent the uncontrolled distribution of apical and basolateral polarity complex proteins in the cell membrane. This is known as 'fence-function' [2] [3]. Especially, the cytoplasmic zonula occludens-1/2/3 proteins (ZO-1/2/3) act as scaffolds between the transmembrane proteins and cytoplasmic interacting proteins. ZO proteins regulate the paracellular seal, integrate external and internal signals and link the TJs to the actin cytoskeleton through direct interaction or through additional protein interactions [4]. Further they are physically linked to cell polarity complexes such as PAR3/6. It was shown that ZO-1 also interacts with AJ proteins afadin and α-catenin (CTNNA1), thereby linking the function of both junctional complexes in epithelial cells [5] [6].

Adherens junctions

AJs are spatial located 'under' the TJs and form the so-called *Zonulae adherentes*. Their structural core consists of classical calcium-dependent transmembrane glycoproteins of the cadherin superfamily, which are on the cytoplasmic part of the membrane associated with members of the catenin family [7] (figure 1). Extracellularly, the ectodomain of the cadherins forms homophilic interactions with cadherins from neighboring cells, while the highly conserved cytoplasmic domain

interacts intracellularly with their adapter proteins like α-catenin and β-catenin, which connect the AJ complex to actin filaments and diverse signaling pathways. Such AJ complexes are known to be highly heterogenous and dynamic as more than 170 proteins have been described to either affect AJ dynamics or bind AJ structures [4] [8]. Depending on the cell type, individual cadherins are expressed as illustrated for the 'classical' E-cadherin, which is primarily detectable in epithelial cells [9]. In great detail, this cadherin is required for the initiation and stabilization of cell-cell adhesion, thereby promoting cell polarization and tissue homeostasis, the modulation of intracellular signaling pathways that control gene transcription, and the linkage and control of the actin cytoskeletal network [10].

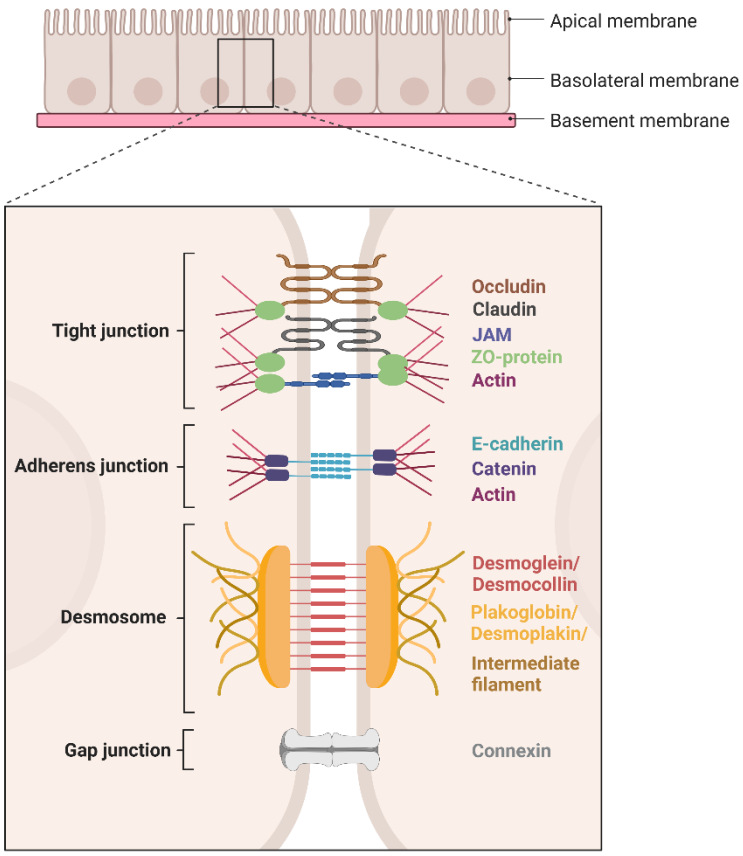

Figure 1: Schematic overview of different types of cell junctions. Adapted from "Cell Junction Types", by BioRender.com (2023). Retrieved from https://app.biorender.com/biorender-templates.

Desmosomes

Desmosomes or *Maculae adherentes* are junctions that mediate strong cell-cell adhesion. They are formed by the non-classical, desmosomal cadherins desmoglein-1/2/3/4 (DSG-1/2/3/4) and desmocollin-1/2/3 (DSC-1/2/3), which form homophilic (DSG-DSG/DSC-DSC) or heterophilic (DSG-DSC) dimers that facilitate interactions between neighboring cells (figure 1) [3]. However, as most junctional structures, desmosomes are not static complexes. Depending on the

environmental requirements, their composition undergoes constant remodeling to allow plasticity what makes them to a highly dynamic system [11] [12]. Importantly, it is so far not well understood how structural changes in desmosomes may change the cell behavior in 'normal' cells and under disease conditions. Interestingly, all DSG genes are located on the same chromosomal arm 18q12.1, suggesting that these genes are evolutionary created by gene duplication. Again, the relevance of individual DSGs in cellular maintenance or the distinct functions of DSGs have not been comparatively investigated, yet. Intracellularly, desmogleins interact with adaptor proteins such as plakoglobin, desmoplakin and plakophilin. Plakoglobin directly binds and clusters the desmosomal cadherins and is thereby essential for desmosome assembly. In addition, it interacts with desmoplakin, which links the membrane-associated desmosomes to intermediate filaments and plakophilin, which modulates the strengths of this interaction [1] [13]. Due to their physical connection with the intermediate filaments, desmosomes provide tensile strength and preserve structural tissue integrity during homeostasis [12] [11]. Further it is shown, that desmosomes can contribute to proliferation-control via EGFR/MEK/ERK, for example, DSG1 can promote differentiation through suppression of EGFR and ERK1/2 signaling [14] [15]. In addition, plakoglobin is described to regulate gene expression by enhancing p53 transcriptional activity, but also by suppression of c-MYC [16] [17].

Gap junctions

Another important type of cell-cell connections are the GJs (figure 1), which have a different function compared to TJs, AJs and desmosomes. They consist of clusters of integral membrane proteins (connexins 1-21), which form communication channels between neighboring cells. By using these channels, adjacent cells can directly exchange information and molecules such as ions, metabolites and signaling molecules. Thus, GJs allow paracellular communication via the physical connection of the cytosol. GJs are present in all kinds of tissue-forming cells, however, the mentioned 'low-resistant' transport of ions is of special importance for the function of electrically excitable cells like neurons or heart muscle cells [1] [18]. Further, GJs can also contribute to the regulation of cell growth and gene expression due to selected transfer of growth and gene regulatory factors like Ca^{2+}, cAMP, inositol triphosphate and siRNAs [19].

Together, cellular junctions create a continues connection through pairs of cells or even cell groups and are essential to maintain tissue homeostasis. They contribute to the structural integrity of epithelia and affect paracellular communication via physical forces and the diffusion of small molecules. Due to their role in many cellular processes, it is not surprising that junctional dysregulation has been described to cause a large number of disorders such as cancer [3].

1.1.2 Junctions control epithelial cell polarity and contribute to cancer development

Epithelial cells form a continuous sheet of tightly connected cells, which line the external-facing surface of organs and tissues, thereby providing structural support and a barrier to protect the internal environment from external stressors like mechanical forces and the entry of pathogens and toxins. These properties of organs and tissues depend to a great extent on the availability of intracellular junctions, which are mostly present in epithelial cells. Irrespective of the underlying challenges, cell junctions directly and indirectly adjust to these stimuli and affect cellular properties due to changes of the cell architecture and transcriptional programs, for example via different signaling pathways [2] [3].

Cell junctions are organized as a lateral belt that allows the separation of apical and basolateral membrane domains, which themselves vary in protein and lipid content and which are characterized by the presence of distinct polarity factor complexes. This spatial organization of cell junctions is therefore central for a high polarization of epithelial cells, which itself is crucial for normal cell behavior under physiological conditions [20] [21]. For example, the outer apical site of the cells is orientated to the lumen (e.g., cavities of organs) of a tissue and often forms specialized structures like microvilli or cilia. In contrast, the basal surface has direct contact with the basal lamina or the ECM and is therefore important for the 'sedentariness' of cells. This junction-based spatial organization enables directional transport of nutrients between the extracellular environment and cells within tissues [2] [22].

Due to the central role of junctional structures in the maintenance of cell polarity and tissue organization, the dysfunctions, mislocalization or aberrant expression of junctional proteins can lead to disturbed epithelial cell polarity and dysregulation of downstream signaling pathways, which is associated with the development of several human diseases or even cancer [23] [21]. For example, increased expression of claudin-1 is shown to activate Notch/PI3K/Akt signaling pathway and thereby promotes colitis-associated cancer [24], while claudin-2 increases the tumorigenicity of colon cancer cells via the EGFR-ERK1/2 axis [25]. Overexpression of DSG2 in epidermal keratinocytes leads to a hyperproliferative and apoptosis-resistant phenotype due to enhanced PI3K/AKT, MEK-MAPK, STAT3 and NF-κB activity, what further associates with the development of skin tumors [26]. In contrast, loss of DSC2 activates Akt and ERK/c-MYC signaling pathway and thereby promotes cell proliferation and tumor growth in liver cancer [27]. However, decreased E-cadherin expression leads to deficiency of functional AJs, which results in loss of cell polarity, cell detachment from epithelial clusters and a change to a more migratory phenotype [21]. Frequently, reduced E-cadherin expression corresponds with elevated N-cadherin expression, which

independently contributes to motility and invasion [28]. This process is termed as epithelial-to-mesenchymal transition (EMT) and can be found in many epithelial-derived tumors like pancreatic or gastric cancer [29] [30]. Another example of how AJ proteins may contribute to cancer disease formation is β-catenin. Interestingly, β-catenin can be found at the membrane, in the cytosol and in cell nuclei under physiological conditions; thus, different subcellular localization of β-catenin should not be considered as 'dysregulation'. Instead, enrichment at the membrane illustrates its importance in AJ functionality, while its nuclear enrichment allows β-catenin to function as transcriptional co-activator [31]. Subcellular trafficking of β-catenin is regulated by the Wingless (Wnt) signaling pathway whose activation leads to the inhibition of β-catenin degradation, followed by nuclear accumulation. Here it stimulates the transcription of pro-proliferative target genes like Cyclin D1 and MYC. However, mutations in β-catenin or Wnt pathway components, which are commonly detected in intestinal cancer, can prevent its degradation and lead to aberrant activation of target gene expression [32] [33].

To conclude, establishment and maintenance of cell junctions and cell polarity are of great importance for the functionality of epithelial cells. Dysregulation of cell-cell contacts and loss of cellular polarity are key events in the formation and progression of several human cancers. Although, first underlying molecular mechanism have been described, it is still not understood which junctional alterations represent tumor-supporting events.

1.1.3 Disturbance of hepatocellular polarity can lead to cancer progression

Many studies on cell polarity focus on the liver as parenchymal hepatocytes, which represent the major cell type in the liver, are highly organized in a three-dimensional network. The main functions of hepatocytes are protein synthesis (e.g., hormones and growth factors), carbohydrate metabolism (e.g., glycogen storage) and synthesis/secretion of bile [34]. However, these functions strictly depend on intense cell-cell contact with neighboring hepatocytes as well as their high degree of polarity. In this context, the unique spatial organization of hepatocytes is characterized by multiple luminal and basal domains. In particular, the apical domains of adjacent hepatocytes are oriented towards each other with small, capillary-like lumens, which are 'sealed' by TJs. These bile canaliculi collect the secreted bile and transport the 'toxic' bile salts into bile ducts. The baso-lateral domain of hepatocytes forms protrusions for an efficient exchange of macromolecules with the sinusoidal blood. This is possible since hepatocytes are not attached to a basal lamina but are surrounded by a low-density ECM material. This spatial structure leads to a directional flow of molecules through apical and basolateral membranes. It is known that these hepatocellular properties are negatively affected in case of disturbed 3-dimensional organization [35] [34].

The relevance of cell-cell contacts and polarity on hepatocyte performance is supported by genetic experiments. For example, downregulation of hepatocyte nuclear factor 4-alpha (HNF-4α), which is a transcription factors that induces the expression of E-cadherin, claudin-1 and ZO-1, results in a dysregulation of TJ and AJ composition. Indeed, in hepatocellular carcinoma (HCC) these changes are frequently observed and serve as a hallmark for EMT and tumor progression [36]. Further, mutations in claudin or ZO-1 and subsequent abnormal TJ formation can lead to increased paracellular permeability resulting in liver injury due to bile reflux [35]. Moreover, it is suggested that ZO-1 acts as tumor suppressor as it controls cellular signal transduction and cell proliferation [37] [38] [39]. Another example is the basolateral polarity complex Scribble, which mislocalization leads to a less pronounced cell polarity and diminished canalicular networks *in vitro* and further supports tumor formation *in vivo* [40].

These observations suggest that the disturbance of cell-cell contact and hepatocellular polarity impairs liver functionality and further plays an important role in the pathogenesis of liver cancer.

1.2 Hepatocellular carcinoma

1.2.1 HCC - Epidemiology, etiology, pathogenesis and therapy

Parenchymal hepatocytes, which account for 60% of all liver cells, are the major cell type of the liver and mediate the metabolic functions [41]. Despite them, the liver also consists of non-parenchymal cells: first, liver sinusoidal endothelial cells, which separate hepatocytes from blood stream and facilitate the porto-central blood flow [42]; second, Kupffer cells (liver-specific macrophages), which are localized in the sinusoids and act as central regulators of immune responses in case of infections [43]; and third, hepatic Stellate cells, which are located in the subendothelial space of Disse and are responsible for the storage of vitamin A and the production of ECM material and collagen in case of liver damage [44]. The liver itself is the main detoxifying organ and further plays important toles in in metabolism, digestion, immune response and synthesis processes [45].

With more than 900,000 new cases and 830,000 death per year, primary liver cancer is the sixth most common cancer and the third most common cause of cancer-related death worldwide, with HCC as the most prevalent primary liver cancer (75-85% of all cases). Incidence and mortality are two- to three-fold higher among men compared to women and the majority of cases can be found in Asia and Africa due to local risk factors [46]. Indeed, risk factors for HCC differ between geographical regions (figure 2). In developing countries such as Egypt or China, most cases arise on

the basis of chronic hepatitis B or C virus (HBV or HCV) infections or aflatoxin-B1 exposure due to *Aspergillus* contaminated food, which causes mutations in the tumor suppressor gene TP53 [47] [48]. In industrialized countries leading risk factors are excessive alcohol abuse and fatty diets associated with excess body weight and type-2 diabetes, which can lead to alcoholic liver disease (ALD) or non-alcoholic fatty liver disease (NAFLD). Other known HCC promoting factors are autoimmune diseases or metabolic disorders like inherited hemochromatosis or tyrosinemia type 1 [48] [49].

However, development of HCC is a multi-step, long-lasting process in response to chronic liver disease (figure 2). Chronic disease conditions are characterized by development of ALD or NAFLD, which can progress to alcoholic steatohepatitis (ASH) or non-alcoholic steatohepatitis (NASH) [48]. Under these conditions, continuous cycles of liver damage (hepatocellular death) and regeneration (hepatocellular proliferation) lead to excess deposition of extracellular connective tissue, produced by hepatic stellate cells. Indeed, liver fibrosis is considered to be a premalignant condition as it represents the basis for additional liver damage processes, mostly associated with severe inflammation (hepatitis). Fibrosis and hepatitis (ASH and NASH) are associated with changes of liver architecture and impairment of liver function, endorsing the development of liver cirrhosis, which further promotes hepatocarcinogenesis. More important, continuous regenerative processes lead to the accumulation of mutations due to the enforced compensatory proliferation, which are one cause for the high genetic heterogeneity of HCC [50].

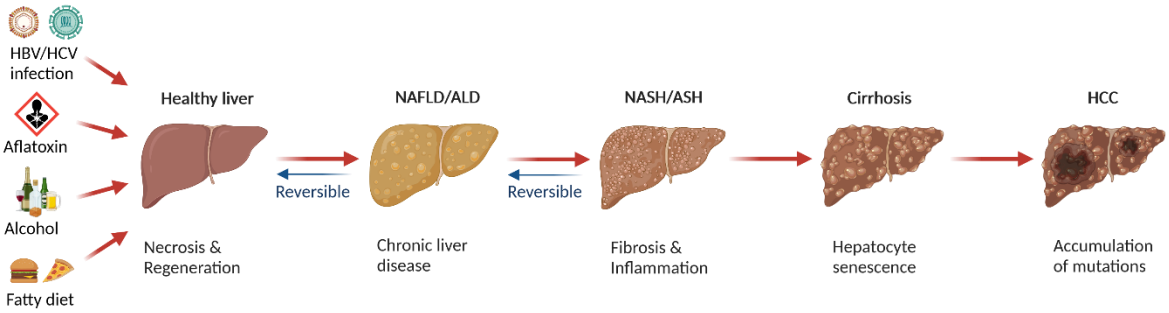

Figure 2: Risk factors and development of HCC. The schema illustrated the risk factors which promote the development of liver disease like NALD or ALD, which can develop to steatosis, hepatitis, cirrhosis and finally HCC. Adapted from "Non-Alcoholic Fatty Liver Disease (NAFLD) Spectrum", by BioRender.com (2023). Retrieved from https://app.biorender.com/biorender-templates.

The overall 5-year survival rate of patients diagnosed with HCC is less than 20% [51]. That's on the one hand because HCC is often late diagnosed what's due to missing symptoms at early stages. On the other hand, treatment is extremely difficult because of the heterogeneity of the tumor and the underlying cirrhosis, what leads to recurrence rates of up to 70% [52] [53]. Depending on the stage

of the disease different treatment options are considered. At early phases, which are characterized by less than three nodules with a diameter <3 cm and preserved liver function, surgical tumor resection represents the gold standard for liver cancer patients. However, when patients already developed cirrhosis liver transplantation is suggested. Other locoregional therapies with curative potential are for example radiofrequency ablation, trans-arterial chemoembolization, radioembolization or percutaneous ethanol injection [53] [52]. At advanced stages, which is characterized by impaired liver function, portal tumor cell invasion and metastasis, the only treatment options are systemic therapies. These strategies include the administration of cytotoxic drugs (e.g., 5-fluoruracil, gemcitabine), treatment with the multi-kinase inhibitors (e.g., sorafenib, regorafenib) or novel immunotherapy (e.g., the combination of the PD-L1 targeting antibody atezolizumab with VEGF-targeting bevacizumab) [54]. However, these therapies moderately prolong patient survival and even with therapy the survival time for most late-stage patients is around one year [55]. These data illustrate that, despite the progress of the last decade, only limited options exist for the systemic and efficient therapy of HCC patients.

Taken together, HCC is characterized by poor clinical outcome due to late diagnosis and limited treatment options. Therefore, it is of importance to gain further mechanistic insight in the underlying processes that cause tumor initiation and that support tumor progression.

1.2.2 Common molecular alterations in HCC

Hepatocarcinogenesis is a multistep process with stepwise accumulation of genetic alterations, making HCC to a genetically and phenotypically heterogenous disease. Genetic alterations found in HCC include activating or silencing point mutations, gene copy number alterations and chromosomal translocations affecting oncogenes or tumor suppressor genes, respectively [56]. Next to these genetic alterations, epigenetic changes are described to change gene activity, such as increased gene promoter methylation, which can lead to silencing of gene expression while DNA hypomethylation can promote gene expression [57] [56]. In general, these genetic and epigenetic changes affect the activity of tumor relevant signaling pathways such as the PI3K/AKT pathway, the MAPK kinase pathway, the Hippo pathway and the TGF-beta pathway with direct impact on (tumor) cell proliferation, apoptosis, migration and differentiation [58].

For the liver it has been shown that the continuous proliferation of hepatocytes in chronic liver disease increases the probability of accumulating genetic alterations. In addition, permanent mitotic activity leads to a steady shortening of chromosome telomeres. Together with the stochastic occurrence of mutations in tumor-relevant genes, this cell cycle-associated shortening of chromosomes is associated with chromosomal instability (CIN) [59]. Indeed, it was shown that

about 30% of HCC patients show high degree of CIN as illustrated by the presence of gene signature that serves as proxy for CIN in six solid cancers including HCC (called CIN25 gene signature) [60]. Interestingly, CIN positive HCC patients not only revealed a higher frequency of chromosomal alteration, but it was also demonstrated that several of the CIN25 signature genes are transcriptionally controlled by the Hippo pathway and its transcriptional effector yes-associated protein (YAP). In this context, the presence of YAP and of the CIN25 gene signature in human HCCs correlated with high tumor cell proliferation, tumor progression and poor clinical outcome of HCC patients [60] [61]. Importantly, increased expression of the enzyme telomerase reverse transcriptase (TERT) leads to the protection of chromosomal telomeres, resulting in unlimited proliferation potential of the cell. This 'cell-protective' mechanism is reasonable for tumor cells in later phases of tumor progression as severe telomer shortening and CIN leads to the induction of senescence and cell death [62]. Indeed, activation mutations in the TERT promoter, providing a new consensus binding site for transcription factors, or gene amplification of TERT can be found in almost 90% of HCC cases and therefore represents one of the top three 'driver mutations' in hepatocarcinogenesis [62] [57] [56]. Next to changes in TERT activity, alterations of other important oncogenes and tumor-suppressor genes have been demonstrated to be of functional relevance for liver carcinogenesis. These include the tumor-suppressor gene TP53, which harbors point-mutations in 12-48% of HCC patients. Since the protein p53 is a key regulator of cell cycle arrest upon DNA damage, deletion or silencing of the TP53 gene may cause uncontrolled cell proliferation [57] [56]. Another example is the homozygous deletion of CDKN2A (2-12%) or mutation in RB1 (3-8%), what results in an inactivation of the retinoblastoma pathway which controls progression from G1 to S phase of the cell cycle [56].

Increasing evidence now illustrate that changes of tissue architecture in HCC can be attributed to a disturbance of cellular polarity, corresponding to dysregulation of cell junctions [39]. Indeed, for several junctional structures heterogenous expression is demonstrated. These expression changes are ranging from low to very high and may differ between tumor samples and even between within a tumor mass. While in well differentiated HCCs a proportion of tumor cells still reveal expression of junctional molecules, poorly differentiated HCC cells are characterized by a partial or complete loss. This has been illustrated for E-cadherin for which the reduction in adjacent tumor cells promotes invasive growth and proliferation of tumor cells, due to loss of cell adhesion and induction of a EMT phenotype [63] [39]. Interestingly, E-cadherin does not only promote HCC progression via junction-forming properties, but also through the modulation of growth inhibitory signals like regulation of tumor-suppressive Hippo signaling pathway [64]. *In vivo* E-cadherin inhibition results in increased liver tumor formation and studies using human HCC material illustrate that diminished E-cadherin levels correlate with intrahepatic metastasis in HCC patients [34] [65] [66]. In contrast,

expression of the large atypical cadherin FAT1 is increased in HCC cell lines and tissues and further correlates with tumor stage and HCC cell proliferation [67]. Next to the aberrant expression, the incorrect intracellular distribution of junctional structures and proteins is observed in HCC cells. As described before, the WNT effector β-catenin is characterized by variable subcellular localization under physiological conditions: the membrane, the cytoplasm and the nucleus. However, mutation in exon 3 of the CTNNB1 gene in 27% of all HCC cases is associated with elevated stability of the protein and artificial nuclear enrichment in HCCs [68]. In addition, other molecular mechanism for the incorrect enrichment of β-catenin has been described for liver cancer. For example, inactivating mutations of negative WNT pathway regulators AXIN-1/2 (3-16%) or APC (1-3%) have been described [56] [39] [68].

However, the situation is probably more complex as most signaling pathways are directly or indirectly connected with cell junction structures and therefore contribute to the composition of junctional complexes and their cell-cell connection properties. For example, dysregulation of oncogenic PI3K/AKT, RAS/MAPK or Notch pathways further promotes cell proliferation and metastasis and are linked to reduced HCC patient survival [56]. Indeed, for all these pathway mechanistic links with cell-cell junctions have been demonstrated in different cell types and organisms. For example, the Notch pathway controls the composition of adherens junctions and cell differentiation in Drosophila melanogaster [69]. If this connection is also of relevance for human cells, especially liver cancer, has not been investigated, yet. However, it illustrates the needs to investigate how junctional structures and cancer-relevant signaling pathways regulate each other in hepatocarcinogenesis.

1.3 The Hippo/YAP signaling pathway

1.3.1 Structure and regulation of the Hippo/YAP pathway

One central hub that connects cell-cell contacts with cell biology under physiological and pathological conditions is the Hippo signaling pathway (figure 3). This pathway represents a conserved cell-density sensing cellular ‘tool’ that regulates cell and organ growth [70]. The major downstream effectors are the transcriptional co-activators yes-associated protein 1 (YAP) and transcription co-activator with PDZ-binding motif (TAZ; synonym: WWTR1) [71]. In case of pathway inactivation, YAP and TAZ are hypo-phosphorylated and translocate into the nucleus where they activate the expression of genes required for proliferation, anti-apoptosis and migration. By doing so, the pathway is of central importance for regenerative processes and contributes to cellular

stemness [72]. Since YAP/TAZ lack DNA binding domains, they mediate the target gene expression via interaction with distinct transcription factors (TFs) like TEA domain family members-1-4 (TEAD-1-4) [73], runt-related transcription factor-1/2 (RUNX-1/2) [74] or mothers against decapentaplegic homolog-2/3 (SMAD-2/3) [75]. However, TEADs are the most important mediators of YAP/TAZ activity and promote activity of pro-proliferative and anti-apoptotic target genes like connective tissue growth factor (CTGF), cysteine-rich angiogenic inducer 61 (CYR61) or ankyrin repeat domain 1 (ANKRD1) [76] [73]. Absence of YAP/TAZ in the nucleus enables the interaction between TEADs and the tumor suppressor vestigial-like protein 4 (VGLL4), leading to inhibition of downstream target gene expression [71] [77].

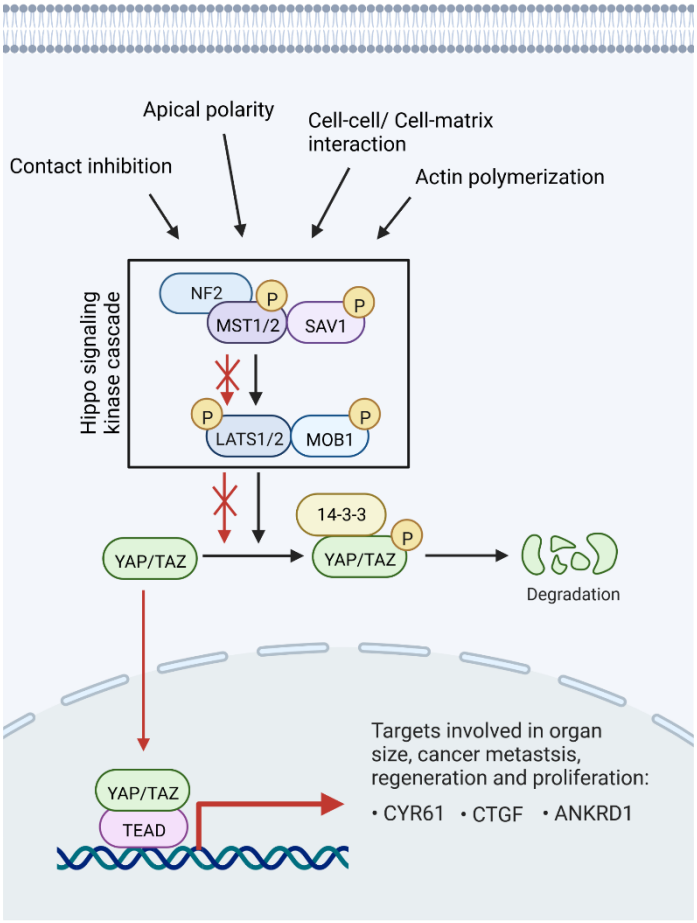

Figure 3: Schematic overview of the Hippo signaling pathway. Adapted from "Hippo Pathway in Mammals", by BioRender.com (2023). Retrieved from https://app.biorender.com/biorender-templates.

When the Hippo signaling pathway is active the central kinase cassette leads to hyper-phosphorylation of YAP/TAZ proteins, resulting in their cytoplasmic retention and degradation, thereby preventing target gene expression. This core Hippo cassette consists of two types of serine-threonine kinases, mammalian STE20-like protein kinase 1/2 (MST1/2) and large tumor suppressor kinases 1/2 (LATS1/2), as well as two adaptor proteins, Salvador family WW domain-containing

protein 1 (SAV1) and mps one binder kinase activator-like 1 (MOB1) [78]. When MST1/2 gets activated, it phosphorylates SAV1 and MOB1, which are required for LATS1/2 recruitment and phosphorylation [78] [79]. In turn, LAST1/2 phosphorylates YAP and TAZ at multiple serine/threonine residues. Phosphorylation at Serine 127 (YAP) or Serine 89 (TAZ) serves as binding site for 14-3-3 proteins, which prevent their shuttling to the nucleus and mediate cytoplasmic retention [80]. In addition, phosphorylation at YAP Serine 381 or TAZ Serine 311 leads to subsequent phosphorylation by Casein kinase 1δ/ε resulting in a phosphodegron formation. This structure recruits the SCF E3 ubiquitin ligase of the beta-TRCP family, which leads to polyubiquitination and proteasomal degradation of YAP/TAZ [81].

Importantly, multiple upstream signals like cell-cell interactions, cell polarity or actin polymerization control Hippo activity. For example it is shown that high cell density in cell culture experiments leads to Hippo pathway activation and nuclear exclusion of YAP/TAZ, pointing to a direct role of this signaling axis in contact inhibition [80] [64]. Therefore, several cell polarity and cell contact proteins are described as Hippo pathway activators, which promote LATS1/2 phosphorylation or directly bind YAP/TAZ and thereby preventing their nuclear enrichment [82]. Another important upstream regulator is the tumor suppressor neurofibromatosis type 2 (NF2; synonym: merlin), which is localized in proximity of AJs and TJs. Due to its close spatial orientation to the outer membrane, NF2 links membrane components with the cytoskeleton structures. For example, NF2 associates with the cytoplasmic phosphoprotein Kibra and recruits LATS1/2 to the plasma membrane, where LATS1/2 gets phosphorylated by MST1/2 and SAV1 [83]. Next to the 'canonical' regulation through conventional cell-cell contact, YAP/TAZ are regulated by mechanical signals like cell polarity, cell stretching and changes in ECM composition. Those signals activate Rho-GTPase signaling, which leads to F-actin assembly and LATS1/2 silencing. Lastly, soluble factors like hormones or growth factors can directly and indirectly modulate Hippo/YAP activity via binding to G protein-coupled receptors (GPCRs). Depending on the ligand, different types of G proteins are coupled to the respective receptors and thereby positively or negatively control YAP/TAZ activity [84]. Mechanistically GPCRs lead to Rho-GTPase activation/silencing, which affects F-actin assembly and thereby mediates the phosphorylation status of LATS1/2. First results also illustrate that secreted factors can also act independently of the GPCRs [84].

Together, these results illustrate that several sources of external information can control this intracellular pathway. There is no distinct ligand-receptor pair, rather the ability of physical forces, extracellular stiffness, cytoskeletal dynamics and cell-cell contacts, that modulates Hippo/YAP activity. As YAP promotes the expression of pro-proliferative target genes, this pathway represents a hub essential in the regulation of tissue development, homeostasis and regeneration.

1.3.2 Hippo signaling in cancer and HCC

During cancer development cells undergo a multitude of changes leading to an aberrant phenotype, which can be characterized by the hallmarks of cancer, including uncontrolled proliferation, escape of cell death, evading growth inhibition and metastasis [85]. Since the Hippo/YAP axis regulates the expression of pro-proliferative target genes and is important for tissue homeostasis and regeneration, it also plays a central role in tumor development. Indeed, it has been shown that this tumor-suppressive pathway is dysregulated in a broad range of human cancers [86]. For example, nuclear YAP enrichment and elevated target gene expression associates with poor clinical outcome and histological dedifferentiation in colorectal, gastric and breast cancers [87] [82]. *In vivo*, elevated YAP activity was reported to promote tumor formation, for example in $KRAS^{G12D}$ lung cancer mouse models, where overexpression of YAP leads to increased lung adenocarcinoma formation [88]. YAP overexpression in YAP-lacking gastric cancer cell line revels enhanced cell proliferation and colony formation *in vitro* and tumor formation *in vivo.* Conversely, inhibition of YAP leads to decreased proliferation and invasion in gastric cancer cells [89]. Since YAP neo expression in cells that are usually lacking YAP activity cause rapid tumor formation, YAP is considered to be a potent oncogene [90] [91]. As YAP is negatively regulated by LATS1/2 and MST1/2 kinases, the Hippo pathway represents a tumor suppressor pathway [86]. This is confirmed by independent mouse models, showing that the knock-down of Hippo pathway components like LATS1 or MOB1 results in a YAP-dependent pro-tumorigenic phenotype in different cell types [92] [93].

Interestingly, somatic mutations affecting Hippo/YAP activity are rare. An exception is NF2, which is reported to be inactivated by mutation in 60% of meningiomas and 55% of schwannomas [87]. In mesotheliomas inactivation by mutation or deletion of NF2, LATS1/2 and MST1/2 is reported in 40%, 7-21% and 2-16% of cases, respectively. However, next to meningiomas and schwannomas, NF2 mutations are only few cases of other solid tumor types (<3%) [94] [87]. Activating mutations in YAP have not been reported in human cancers [76] [95]. However, amplification of genomic regions coding for YAP at chromosome 11q22 is observed in melanomas, ovarian and non-small cell lung cancers with low frequency [96] [82]. Next to these genetic changes, epigenetic alteration may also contribute to the dysregulation of the Hippo/YAP signaling axis. For example hypermethylation of the LATS1/2 promoter, leading to its downregulation and subsequent YAP activation, has been reported in 50% of breast cancers, while hypermethylation of the MST1/2 promoter was detected in 37% of soft tissue sarcomas [86].

Together, these data demonstrate that YAP activity is in most cases not regulated by transcriptional processes. In contrast, it is mainly regulated by alterations via posttranscriptional phosphorylation pattern and changes in subcellular localization. Especially for HCC, more than 60% of patients reveal

an accumulation of YAP in tumor cell nuclei, which statistically correlates with worse overall survival [97] [98]. Moreover, a meta-analysis of HCC patient cohorts indicates that overexpression of YAP is associated with vascular invasion, tumor cell dedifferentiation, tumor size and tumor stage [99]. Therefore, it is now well accepted that YAP is a central oncogenic 'driver' in about 30-50% of human HCCs [97] [100] [61]. As illustrated for other organs, hepatocyte-specific overexpression of constitutively active YAP (S127A mutant) leads to massive liver overgrowth and rapid formation of tumors with HCC characteristics [101] [102]. Equally, deletion of Hippo kinase components/regulators promotes HCC formation and these effects can be abrogated by YAP inactivation. For example, NF2 knockout mice develop hyperplasia and HCC. Simultaneous deletion of YAP in these NF2-deficient models abolishes tumor initiation, illustrating a very linear mechanistic relationship between the Hippo cassette and oncogenic YAP activity [103]. Similar effects are observed for combined MST1/2 deficiency, leading to increased hepatocyte proliferation and eventually HCC development in a YAP-dependent manner [104]. Together the studies confirm the central role of Hippo/YAP deregulation in HCC formation.

Interestingly, the close connection between Hippo/YAP pathway activity and processes that sense cell-cell contact, cell polarity and cytoskeletal dynamics suggest that changes in cell contact could directly or indirectly control tumor formation via the Hippo pathway. In addition, it is unknown if changes in junctional structures contribute to oncogenic Hippo/pathway activity via distinct molecular mechanisms or if any kind of cell contact alteration changes Hippo/YAP activity. Thus, a systematic screen of dysregulated junction factors in human HCC tissues could be informative regarding the aberrant composition of junction structures with possible impact on YAP activity in hepatocarcinogenesis.

2 Aims

Cell-cell connections, mediated by cell junctions, play an important role in cell polarity and tissue homeostasis. Therefore, dysregulation of junctional structures is associated with the development of several diseases such as tumor formation. Since the function of liver-resident hepatocytes strictly depends on a high degree of spatial organization, disturbance of hepatocellular polarity is one key molecular and histomorphological feature in hepatocarcinogenesis. In this context, the activity of the cell-cell contact-sensing and organ size-controlling Hippo/YAP pathway is frequently dysregulated in HCC. Indeed, first data indicate a direct connection between junctional structures and Hippo/YAP activity. However, it is unknown if the oncogene YAP unspecifically responds to cell contact changes or if specific molecular mechanism exist that connect the dysregulation of junctional constituents with YAP activity. Thus, the goal of this project is to identify molecular connections linking aberrantly expressed junctional proteins with Hippo/YAP pathway activity.

The specific goals of this project are:

- Systematic screening for dysregulated cell junction and cell polarity factors in HCC patient cohorts.
- Shortlisting candidates for which the dysregulation statistically associates with poor clinical outcome and YAP activity.
- Confirming the link between junction protein candidates and YAP *in vitro.*
- Investigating the biological/functional relevance of the identified candidates in suitable liver cancer cell lines.
- Identifying the molecular/mechanistic connection between junction protein candidates with Hippo/YAP pathway activity.
- Analyzing the tumor-initiating and/or tumor-promoting properties *in vivo*.

3 Materials and Methods

3.1 General chemicals and consumables

All general chemicals and reagents used in this study are listed in table 1.

Table 1: General chemicals and reagents.

Chemical/reagent	Supplier
Acetic acid (AcOH)	Carl Roth, Karlsruhe, Germany
Acetone	Merck, Darmstadt, Germany
Acrylamide/Bis solution 29:1	SERVA, Heidelberg, Germany
Albumin fraction V, biotin-free (BSA)	Carl Roth
Ammonium persulfate (APS)	Bio-Rad, München, Germany
Boric acid	LabChem, Dinslaken, Germany
Bromphenol blue	Sigma-Aldrich, Taufkirchen, Germany
Cristal violet	Sigma-Aldrich
Dithiothreitol (DTT)	SERVA
Ethylenediamine tetra-acetic acid (EDTA)	SERVA
Ethanol (EtOH)	Merck
Formaldehyde solution 30%, methanol-free	Carl Roth
Glycerol	Thermo Fisher Scientific, Darmstadt, Germany
Glycine	Sigma-Aldrich
Hydrochloric acid (HCl)	Merck
Lithium chloride (LiCl)	Carl Roth
Methanol (MeOH)	Sigma-Aldrich
NP-40	Sigma-Aldrich
Paraformaldehyde (PFA)	Merck
Phosphate-buffered saline (PBS)	Sigma-Aldrich
Phenylmethanesulfonylfluoride (PMSF)	Sigma-Aldrich
Sodium chloride (NaCl)	LabChem
Sodium-deoxycholate (Na-desoxycholate)	Carl Roth
Sodium-dodecylsulfate (SDS)	SERVA
Tetramethylethylenediamine (TEMED)	Carl Roth
Tris-hydroxymethyl-aminomethane (Tris)	Carl Roth
Triton X-100	Merck
Tween 20	Carl Roth
UltraPure™ DNase/RNase-free distilled water	Thermo Fisher Scientific

General plastic ware and consumables used in this study are listed in table 2.

Table 2: General Consumables

Consumables	Supplier
Amersham™ Protran™ 0.45 µm Nitrocellulose Blotting Membrane	GE Healthcare, Solingen, Germany
Cell culture plates	NeoLab, Heidelberg, Germany
Cell scrapers	Corning, New York, USA
DISTRITIP	Gilson, Limburg, Germany
Falcon tubes	Greiner Bio-One, Frickenhausen, Germany
MicroAmp® fast 96-well reaction plate (0.1 ml)	Thermo Fisher Scientific
MicroAmp® optical adhesive film	Thermo Fisher Scientific
Microcentrifuge tubes	Eppendorf, Hamburg, Germany

Microscope slides and cover glasses	Engelbrecht, Edermünde, Germany
Millex-HA filter (0.45 µm)	Merck
Parafilm	Pechiney, Düsseldorf, Germany
Pasteur pipettes	Wilhelm Ulbrich, Bamberg, Germany
PCR reaction tubes	Brand, Wertheim, Germany
Pipette tips	Sarstedt Greiner Bio-One
Scalpels	Feather, Osaka, Japan
Sterile stripettes®	Corning, New York, USA
Whatman™ 3MM Chr	GE Healthcare

3.2 Antibodies

Used antibodies, applications and used dilutions are indicated in table 3.

Table 3: Antibodies

Primary Antibody (clone)	Species	Application	Dilution	Company
ACTB (A3E5)	mouse	WB	1:1,000	Cell Signaling, Frankfurt, Germany
Biotin	mouse	WB	1:1,000	DAKO, Hamburg, Germany
CTGF	rabbit	WB	1:500	Santa Cruz Biotechnology, Heidelberg, Germany
CYR61 (D4H5D)	rabbit	WB	1:1,000	Cell Signaling
DSG1 (P124)	mouse	IHC-Fr	1:10	Progen, Heidelberg, Germany
DSG1 (27B2)	mouse	WB	1:1,000	Thermo Fisher Scientific
DSG2 (AH12.2)	mouse	Co-IP IF IHC-Fr WB	2 µg 1:100 1:200 1:500	Santa Cruz Biotechnology
DSG2	rabbit	PLA	1:100	Boster Biological Technology, Pleasanton, USA
Flag (M2)	mouse	Co-IP WB	2 µg 1:1,000	Merck
GAPDH	chicken	WB	1:4,000	EMD Milipore, Darmstadt, Germany
GFP (D5.1)		IHC-P	1:100	Cell Signaling
Ki67	rabbit	IHC-P	1:500	Abcam, Cambridge, UK
LATS2 (C-2)	mouse	PLA	1:100	Santa Cruz Biotechnology
LATS2 (D83D6)	rabbit	WB	1:1,000	Cell Signaling
NF2 (B-12)	mouse	PLA	1:100	Santa Cruz Biotechnology
NF2 (D1D8)	rabbit	WB	1:1,000	Cell Signaling
PARP	rabbit	WB	1:1,000	Cell Signaling
β-tubulin (5H1)	mouse	WB	1:1,000	BD Bioscience, Heidelberg, Germany
VASP (A-11)	mouse	IF IHC-Fr IHC-P PLA WB	1:50 1:100 1:50 1:100 1:500	Santa Cruz Biotechnology
VASP (9A2)	rabbit	Co-IP WB	2 µg 1:1,000	Cell Signaling
Vinculin (hVIN-1)	mouse	WB	1:1,000	Sigma-Aldrich
YAP	rabbit	IF	1:60	Bethyl Laboratories, Montgomery, USA
YAP (H-9)	mouse	PLA	1:100	Santa Cruz Biotechnology

YAP XP (D8H1x)	rabbit	Co-IP IHC-P PLA WB	2 µg 1:200 1:100 1:1,000	Cell Signaling
p-YAP	rabbit	WB	1:1,000	Cell Signaling
Secondary Antibody	**Isotype**	**Application**	**Dilution**	**Company**
anti-mouse Cy3	donkey IgG	IF	1:300	Jackson Immuno Research, Newmarket, UK
anti-mouse 488	donkey IgG	IF	1:300	Jackson Immuno Research
anti-rabbit Cy3	donkey IgG	IF	1:300	Jackson Immuno Research
IRDye® 680LT anti-chicken	donkey IgG	WB	1:20,000	LI-COR Bioscience, Bad Homburg, Germany
IRDye® 680LT anti-mouse	donkey IgG	WB	1:20,000	LI-COR Bioscience
IRDye® 680LT anti-rabbit	donkey IgG	WB	1:20,000	LI-COR Bioscience
IRDye® 800CW anti-mouse	donkey IgG	WB	1:20,000	LI-COR Bioscience
IRDye® 800CW anti-rabbit	donkey IgG	WB	1:20,000	LI-COR Bioscience

Co-IP: co-immunoprecipitation, IF: immunofluorescence, IHC-Fr/P: immunohistochemistry- fresh frozen section/fixed and paraffin embedded, PLA: proximity ligation assay, WB: Western immunoblotting

3.3 Cell Culture

3.3.1 Cell lines

All used cell lines were obtained from the American Type Culture Collection (ATCC; LGC Standards GmbH, Wesel, Germany) or the Japanese Collection of Research Biosources (JCRB; via Tebu-Bio, Offenbach, Germany) and are listed in table 4.

Table 4: Cell lines and origin.

Cell line	Origin	Supplier
HepG2	Hepatoma	ATCC
Huh7	HCC	JCRB
HLF	HCC	JCRB
Hek293T	Human embryonic kidney (expressing mutant SV40 large T antigen)	ATCC

3.3.2 Cultivation and seeding of cells

Cells were cultured in 10 cm culture dishes containing RPMI (Roswell Park Memorial Institute 1640 medium, Sigma-Aldrich) or DMEM (Dulbecco's Modified Eagle Medium, Sigma Aldrich) medium, supplemented with 10% FCS (Fetal bovine serum, Thermo Fisher Scientific) and 1% P/S (Penicillin/Streptomycin, Thermo Fisher Scientific) in an CO_2 incubator (5%) at 37°C. When reaching 80% confluence, medium was removed, cells were washed with PBS (Dulbecco's Phosphate Buffered Saline, Sigma-Aldrich) and the cells were detached with trypsin-EDTA solution (Sigma-

Aldrich) at 37°C for 10 min. Cells were resuspended in an appropriate amount of cell culture medium and transferred into a new culture dish. Cells were routinely checked for mycoplasma contamination and authenticity by short tandem repeat (STR) analysis (DSMZ, Braunschweig, Germany).

For seeding a particular number of cells for transfection experiments, the cell number was determined. Therefore, cells were washed with PBS, trypsinized and centrifuged at 1,000 x g for 5 min. The cell pellet was resuspended in cell culture medium and counted using a Neubauer chamber. The cell numbers used for different culture dishes are summarized in table 5.

Table 5: Cell numbers for seeding of cells in different cavities.

Cell line	Cultivation medium	10 cm	6-well	12-well	48-well	96-well
HepG2	RPMI	-	100,000	50,000	25,000	10,000
Huh7	DMEM	-	80,000	-	-	
HLF	DMEM	2 x 10^6	60,000	30,000	15,000	5,000
Hek293T	DMEM	1.8 x 10^6	30,000	-	-	-

3.3.3 Transient transfection of siRNAs

For gene-specific inhibition of genes, small-interfering RNA (siRNA) was transfected for RNA interference. siRNAs were designed using E-RNA*i* (DKFZ, Heidelberg, Germany) and synthesized at Eurofins Genomics (Ebersberg, Germany). Sequences of siRNAs are listed in table 6.

Table 6: Small interfering RNA sequences.

Target gene and siRNA	RNA accession number	Sequence (5'-3')
NTC	NA	UGGUUUACAUGUCG CUAA
DSG2 si1	NM_001943	CACAUACUCUUGUGAUGAAAA-dTdT
DSG2 si2		CUGUAAAGAUUGUGGCCAUAU-dTdT
VASP si1	NM_003370	GCAGAAAGUGAAAGAGGAAAU-dTdT
VASP si2		GGGGAAGGAAGGAGGGAAUUU - dTdT

For siRNA transfection assays, cells were seeded one day prior to transfection (chapter 2.4.2). The transfection reagent Oligofectamine (Sigma-Aldrich) and siRNAs were diluted in Opti-MEM (Thermo Fisher Scientific) and incubated for 7 min (table 7). Afterwards, both solutions were mixed and incubated at room temperature for 20 min. During complex formation cells were washed with PBS and covered with Opti-MEM. Next, the transfection solution was spread onto the cells. Gene specific siRNAs were used at a final concentration of 20 nM. Untreated and control siRNA (non-targeting control; NTC)-treated cells served as negative controls. Four hours after transfection, cell line specific culture medium was added. The complete medium was replaced after 24 h of culture.

Cells were harvested 48 h after siRNA transfection for nucleic acid or protein isolation or reseeded for further incubation and functional analyses.

Table 7: SiRNA transfection protocol.

		10 cm	6-well	12-well	48-well
A	Opti-MEM	900 µl	180 µl	90 µl	22.5 µl
	siRNA [20 µM]	5 µl	1 µl	0.5 µl	0.13 µl
B	Opti-MEM	75 µl	15 µl	7.5 µl	1.88 µl
	Oligofectamine	15 µl	3 µl	1.5 µl	0.38 µl
Cell culture plate	Opti-MEM	4 ml	800 µl	400 µl	100 µl

3.3.4 Transient transfection of plasmids

Cells were seeded on 10 cm dishes at least one day prior transfection (chapter 3.4.2). When reaching 80% confluence, cells were transfected using the Fugene® HD Reagent Kit (Promega, Mannheim, Germany). For this, 10 µg of plasmid and 25 µl of Fugene® HD reagent were diluted in 1 ml Opti-MEM medium and incubated for 15 min at room temperature. The mixture was then distributed dropwise of the cells and incubated for further 48 h.

3.3.5 Lentiviral transduction of cells

For stable and inducible gene overexpression in cells, lentiviral transduction of the respective cDNA cloned in expression vectors was performed (chapter 3.5.3). Firstly, the respective lentiviral particles were generated. For this, 1,8 x 10^6 Hek293T cells were seeded in 10 ml DMEM on 10 cm cell culture dishes, one day prior transfection. The next day, cells were washed with PBS and 9 ml DMEM was added. For transfection, 10 µg of the respective plasmid, 8 µg of the packaging vector psPAX2, 2.5 µg of the envelope plasmid pMD2G and 60 µl of the transfection reagent PEI (Polyethylenimine, Polyscience, Warrington, USA) were diluted in 1 ml Opti-MEM, incubated for 30 min and then distributed dropwise on the cells. Medium was changed after 15 h. The next day, the virus particles-containing supernatant was collected and filtered using filters with 0.46 µm pore size. In parallel, HLF and HepG2 cells were seeded on 6-well plates. The next day, a mixture of 1 ml cell culture medium, 1 ml virus suspension and 16 µg polybrene (Hexadimethrine bromide, Sigma-Aldrich, final concentration of 8 µg/ml) was added to the cells and incubated overnight. Cells were washed twice with PBS and cultured containing 1 µg/ml puromycin (Sigma-Aldrich) for selection of transduced cells carrying the vector. Selection pressure was maintained during cultivation.

3.3.6 Induction of gene expression with doxycycline

For induction of target gene expression in stably transduced cells (chapter 3.4.5), cultivation medium was supplemented with 2 µg/ml doxycycline (Doxycycline hyclate, Sigma-Aldrich) and cells were incubated at least for 48 h. As negative controls served, untreated cells and the original cell lines without lentiviral manipulation.

3.3.7 Treatment with azacytidine

Huh7 cells were seeded on 6-well plates (chapter 3.4.2). After 24 h and 48 h, new medium supplemented with different concentrations of azacytidine (0, 5, 10, 30 µM, Accord Healthcare GmbH, München, Germany) was added. Cells were harvested and RNA was isolated and reverse transcribed into complementary DNA (cDNA) after 72 h of treatment (chapter 3.6.1). Abundance of target genes (DSG1, DSG2) and control genes (SHP1, DNTM1) was analyzed by qPCR (chapter 3.6.2).

3.4 Molecular Cloning

3.4.1 Enzymes and regents for cloning

All enzymes and reagents used for Gateway and restriction cloning are listed in table 8.

Table 8: Enzymes and reagents used for cloning.

Name	Company
Dimethyl sulfoxide (DMSO)	Thermo Fisher Scientific
dNTP-Mix	Thermo Fisher Scientific
EcoRI restriction enzyme	Thermo Fisher Scientific
Gateway® BP Clonase™ II Enzyme Mix	Thermo Fisher Scientific
Gateway® LR Clonase™ II Enzyme Mix	Thermo Fisher Scientific
MluI restriction enzyme	New England Biolabs, Frankfurt, Germany
Phusion® High-Fidelity DNA Polymerase	New England Biolabs
StuI restriction enzyme	Boehringer Mannheim, Germany
T4 DNA ligase	New England Biolabs
10x Tango buffer	Thermo Fisher Scientific

3.4.2 Polymerase chain reaction

For the amplification of cDNA without errors, gene-specific cDNA polymerase chain reaction (PCR) was performed. For this, the PCR reaction was prepared according to table 9. The thermocycling conditions are indicated in table 10. For further cloning, PCR products were purified using the Wizard® SV Gel and PCR Clean-Up System (Macherey-Nagel, Düren, Germany) according to the manufacturer's instructions.

Table 9: Gateway PCR master mix

Reagent	Volume
5x Phusion GC buffer	10 µl
10 mM dNTPs	1 µl
Forward primer (10 µM)	2.5 µl
Reverse primer (10 µM)	2.5 µl
cDNA template	2 µl
Phusion® High-Fidelity DNA polymerase (2 U/µl)	0.5 µl
DMSO	1.5 µl
dH_2O	ad 50 µl

Table 10: Gateway PCR thermocycling conditions

Description	Temperature	Duration	Cycles
Initial denaturation	98°C	30 s	1x
Denaturation	98°C	30 s	30x
Annealing	55°C	30 s	
Elongation	72°C	30 sec/kb	
Final elongation	72°C	10 min	1x

3.4.3 Gateway Cloning

For the overexpression of genes in human cell lines, respective vector constructs were generated using the Gateway cloning system. For cloning of DSG1, DSG2 and VASP into the Gateway system, the cDNAs were amplified using the Phusion DNA polymerase (chapter 3.5.2). As template, respective cDNA-containing plasmids were used (phDSG1, phDSG2, phVASP). Primers used for Gateway-PCR were designed according to the Gateway manual's instructions, containing either *att*B1 or *att*B2 sites for recombination with pDONR plasmids. Nucleic acids were ordered from Thermo Fisher Scientific and are listed in table 11.

For the first cloning step, BP recombination between the generated Gateway-PCR products and the pDONR plasmids was performed using the Gateway® BP Clonase™ II Enzyme Mix according to the manufacturer's instructions. In the second step, recombination between the cDNA containing pDONR plasmids and the destination vectors (pDest_Flag, pTRIPZ, pBirA-N, pBirA-C), the Gateway® LR Clonase™ II Enzyme Mix was used according to the manufacturer's instructions.

Table 11: Gateway PCR primer

Name	Sequence (5'-3')
GW hDSG1 for	GGGGACAAGTTTGTACAAAAAAGCAGGCTCCACCATGGACTGGAGTTTCTTC
GW hDSG1 rev	GGGGACCACTTTGTACAAGAAAGCTGGGTTCTACTTGCTATATTGCACGG
GW hDSG1 rev noStop*	GGGGACCACTTTGTACAAGAAAGCTGGGTTCTTGCTATATTGCACGG
GW hDsg2 fw	GGGGACAAGTTTGTACAAAAAAGCAGGCTCCACCATGGCGCGGAGCCCGGGA
GW hDsg2 rev	GGGGACCACTTTGTACAAGAAAGCTGGGTTTTAGGAGTAAGAATGCTGTA

GW hDsg2 rev noStop*	GGGGACCACTTTGTACAAGAAAGCTGGGTTGGAGTAAGAATGCTGTA
GW hVasp fw	GGGGACAAGTTTGTACAAAAAAGCAGGCTCCACCATGAGCGAGACGGTCATC
GW hVasp rev	GGGGACCACTTTGTACAAGAAAGCTGGGTTTCAGGGAGAACCCCGCTTCC

*noStop: primers for cloning of cDNA without stop codon, which allow tagging of proteins at the C-terminus.

3.4.4 Generation of pT3-plasmids for murine expression

For the preparation of pT3-vectors containing murine DSG2 and VASP cDNA, 'traditional' restriction cloning was applied. Murine cDNA was amplified using gene specific oligonucleotides (table 12), adding a restriction site at the beginning and the end of the sequence (chapter 3.5.2). After purification of the DNA fragments, a double digest was performed at 37°C for 2 h. The digested products were purified and ligation was performed at room temperature overnight (table 13).

Table 12: Cloning primers for murine cDNA

Name	Sequence (5'-3')
mDSG2 MluI fw neu	TATACGCGTATGGCGCGGAGCCCGGGTGAC
mDSG2 StuI rev neu	GAGGCCTCTTTAGGAGTAAGAATGTTGCATGGTGCTATGCTTGGTG
mVASP MluI fw neu	ACTACGCGTATGAGCGAGACGGTCATCTGTTCCAG
mVASP EcoRI rev	GATCGAATTCTCAAGGAGACCCCCGCTTCCTCAGC

Table 13: Standard protocol for double digest and ligation

PCR-product restriction		Plasmid restriction		Ligation	
Reagent	**Volume**	**Reagent**	**Volume**	**Reagent**	**Volume**
PCR-product	30 µl	pT3 plasmid	2 µg	Vector	1 µl
MluI (10 U/µl)	1 µl	MluI (10 U/µl)	1 µl	Insert	2 µl
StuI/EcoRI (10 U/µl)	1 µl	StuI/EcoRI (10 U/µl)	1 µl	T4 Ligase (400 U/µl)	1 µl
10x Tango buffer	10 µl	10x Tango buffer	6 µl	10x T4 Ligase buffer	1 µl
H_2O	Ad 50 µl	H_2O	Ad 30 µl	H_2O	Ad 10 µl

3.5 Equipment

Equipment and devices used in this study are listed in table 14.

Table 14: List of laboratory equipment

Equipment	Company
12 Tube magnet	Qiagen, Hilden, Germany
Aperio® AT2 scanner	Leica Mikrosysteme, Wetzlar, Germany
Axioplan 2 microscope	Zeiss, Oberkochen, Germany
Bacteria incubator	Memmert, Schwabach, Germany
BIOWIZARD Silver Line safety cabinet	Ewald, Bad Nenndorf, Germany
Centrifuge 5415R	Eppendorf

Cyclone Thermal Cycler	Biozym, Hessisch Oldendorf, Germany
DNA Engine® Thermal Cycler	Bio-Rad, München, Germany
Electrophoresis Power Supply EV231 and EV302	Consort, Turnhout, Birmingham
FLUOstar Omega microplate reader	BMG Labtech, Ortenberg, Germany
Heracell™ VIOS 250i CO_2 Incubator	Thermo Fisher Scientific
Megafuge 16R	Thermo Fisher Scientific
Mikro 200 centrifuge	Hettich, Tuttlingen, Germany
Mini Trans-Blot Cell	Bio-Rad
Mini-PROTEAN® Tetra Cell Casting Module	Bio-Rad
NanoDrop ND-1000 spectrophotometer	Thermo Fisher Scientific
Neubauer counting chamber	Brand, Frankfurt, Germany
Odyssey Sa Infrared imaging system	LI-COR Bioscience
Olympus BX53, CKX31, IX81	Olympus
QuantStudio™ 5 Real-Time PCR System, 96-well	Thermo Fisher Scientific
Roll shaker CAT RM5	Neolab, Heidelberg, Germany
Thermomixer compact	Eppendorf
Transsonic T460/H ultrasound water bath	Elma, Singen, Germany

3.5.1 Plasmids

All plasmids used in this study are listed in table 15.

Table 15: All plasmids used in this study.

Plasmid	Full name	Description	Origin
phDSG1	pm-Cherry-DSG1-N-18	amplification of human DSG1, Gateway cloning	AddGene
phDSG2	pm-Cherry-DSG2-N-18	amplification of human DSG2, Gateway cloning	AddGene
phVASP	pGEM-VASP	amplification of human VASP, Gateway cloning	Sino biological
pDONR	pDONR201	BP backbone, Gateway cloning	Gift from Stefan Pusch, DKFZ
pDest_Flag	pDEST26-N-FLAG_NeoR	LR backbone, Gateway cloning, Flag-tag	Gift from Stefan Pusch, DKFZ
pDest_DSG2-Flag	pDEST26-N-FLAG_NeoR_DSG2	human Flag-DSG2 expression vector, Gateway cloning	Generated in this study
pTRIPZ	pTRIPZ_GW	LR backbone, stable inducible expression, Gateway cloning	Gift from Stefan Pusch, DKFZ
pT_DSG1	pTRIPZ_DSG1	Stable inducible DSG1 expression, Gateway Cloning	Generated in this study
pBirA-C	pTRIPZ-BirA-Flag-C-terminal	LR backbone, BioID, Gateway Coning	Alessandro Ori, Fritz Lipmann Institute
pBirA-N	pTRIPZ-BirA-Flag-N-terminal	LR backbone, BioID, Gateway Cloning	Alessandro Ori, Fritz Lipmann Institute
pDSG1-C	pTRIPZ-BirA-Flag-C-terminal_DSG1_nsc	stable inducible DSG1-BirA expression, Gateway cloning	Generated in this study
pDSG2-C	pTRIPZ-BirA-Flag-C-terminal_DSG2_nsc	stable inducible DSG2-BirA expression, Gateway cloning	Generated in this study
pVASP-N	pTRIPZ-BirA-Flag-N-terminal_VASP	stable inducible BirA-VASP expression, Gateway cloning	Generated in this study
pVASP-C	pTRIPZ-BirA-Flag-C-terminal_VASP_nsc	stable inducible VASP-BirA expression, Gateway cloning	Generated in this study
psPAX2	psPAX2	Virus production	Addgene

pMD2G	pMD2G	Virus production	Addgene
pmDSG2	pGEM-mDSG2	amplification of murine DSG2	Sino biological
pmVASP	CpUC19-mVASP	amplification of murine VASP	Sino biological
pT3_empty	pT3-EFIGS_linker_GFP	Hydrodynamic tail vein injection	Gift from Darjus Tschaharaganeh, DKFZ, Heidelberg, Germany
pT3_c-MYC	pT3-EF1a-c-MYC-IRES-GFP	Hydrodynamic tail vein injection, c-MYC	Generated in this study
pT3_DSG2	pT3-EFIGS_linker_GFP_DSG2	Hydrodynamic tail vein injection, murine DSG2	Generated in this study
pT3_VASP	pT3-EFIGS_linker_GFP_VASP	Hydrodynamic tail vein injection, murine VASP	Generated in this study
pCMV-SB10	pCMV-SB10	Hydrodynamic tail vein injection, Sleeping Beauty transposase	Gift from Darjus Tschaharaganeh, DKFZ

3.5.2 Bacterial transformation and plasmid isolation

For the reproduction of plasmids, One Shot™ Mach1™ T1 Phage-Resistant Chemically Competent *E. coli* (Thermo Fisher Scientific) were used. Plasmids were transformed into bacteria using heat shock. For this, plasmids were mixed with 50 µl chemocompetent bacteria and incubated on ice for 30 min. Heat shock was performed at 42°C for 45 s, followed by incubation on ice for 5 min. Subsequently, bacteria were plated on LB- (LB broth Lennox, Carl Roth, Karlsruhe, Germany) agar (Bacto™ Agar, BD, Heidelberg, Germany) plates supplemented with 50 µg/ml carbenicillin (carbenicillin disodium salt, Carl Roth) and incubated at 37°C overnight. In case of pDONR plasmids, 150 µl SOC medium (New England Biolabs) was added after heat shock and bacteria were incubated at 37°C with shaking for 1 h and plated on LB-agar plates supplemented with 50 µg/ml kanamycin (kanamycin sulphate, Carl Roth). Single colonies were picked and cultured in 5 ml (Miniprep) or 250 ml (Maxiprep) LB medium containing the respective antibiotics at 37°C with shaking overnight. Plasmid DNA was isolated using either the NucleoSpin® Plasmid extraction kit (Macherey Nagel) for small-scale vector isolations (Miniprep) or the EndoFree® Plasmid Maxi Kit (Qiagen, Hilden, Germany) for large-scale isolations (Maxiprep) and mouse experiments, according to the manufacturer's instructions.

3.5.3 Sequence validation

All vector constructs and PCR products were validated by Sanger sequencing (Seqlab-Sequence Laboratories, Göttingen, Germany). All used sequencing primers were ordered from Thermo Fisher Scientific and are listed in table 16. Sequence results were analyzed using the plasmid editor ApE.

Table 16: Sequencing primer

Name	Sequence (5'-3')	Application
hDSG1 Seq for1	CAATACGGCCAGTATGCTCT	human DSG1 sequencing
hDSG1 Seq for2	ACCAATACTGGCAGACAAGA	human DSG1 sequencing
hDSG1 Seq rev1	GAGGATCGAGAATAGGCTTA	human DSG1 sequencing
hDSG1 Seq fw3	GTGCACGTTCACGATAACCG	human DSG1 sequencing
hDsg2 fw1	GAACACAGCAGCTACACTTTG	human DSG2 sequencing
hDsg2 fw3	CACTAGCTGAAGTTTGCCTG	human DSG2 sequencing
hDsg2 rev1	GCAGGTTTTTGTCTCTGCTC	human DSG2 sequencing
hVasp fw1	CATCAACTGTGCCATCGTCC	human VASP sequencing
hVasp rev1	GGTTGTGCTGTTCTTCTCCC	human VASP sequencing
hVASP seq rev2	CCGAAGAAGACGACTTCATC	human VASP sequencing
BirA-N seq fw	GCATCAACCTGGACCGGAAC	BioID vector sequencing
BirA-C Att region fw	CGTATGTCGAGGTAGGCGTG	BioID vector sequencing
mDSG2 seq fw1	GTATGAGGGGACAGTGGAAG	murine DSG2 sequencing
mDSG2 seq fw3	CTGATCGTGACAGAGAGGGTG	murine DSG2 sequencing
mDSG2 seq rev1	GGAGCAGGAGTGCTAGAATC	murine DSG2 sequencing
mDSG2 seq rev2	CTCAATGGACCCAACAAAGAC	murine DSG2 sequencing
mVASP seq fw1	CAGGTGGTTATCAACTGTGC	murine VASP sequencing
mVASP seq rev2	GTCTTCTCACAGGTTCACTC	murine VASP sequencing
pT3 IRES rev	CGTCAAGAAGACAGGGCCAG	pT3 sequencing

3.6 Methods of molecular biology

3.6.1 RNA isolation and cDNA synthesis

Total RNA was isolated using the ExtractMe Total RNA Kit (7BioSciences, Hartheim, Germany) following the manufacturer's instructions. RNA concentration and purity were determined using the Nanodrop spectrophotometer. cDNA was synthesized using 500 ng of total RNA with the PrimeScript RT Reagent Kit (TakaraBio, Saint-Germain-en-Laye, France), according to the manufacturer's instructions. For the reverse transcription, random hexamer primers were applied. cDNA samples were diluted 1:50 with UltraPure distilled Water and stored at -20°C.

3.6.2 Semi-quantitative real-time PCR (qPCR)

Gene expression was analyzed at nucleic acid level using qPCR. Reactions were setup using the primaQuant 2x qPCR-SYBR-Green-MasterMix (Steinbrenner Laborsysteme, Wiesenbach, Germany) as indicated (table 17). Thermocycling condition and subsequent melting curve analysis to assure product specificity are illustrated in table 18. Each sample was analyzed in technical triplicates. Relative gene expression was calculated using the comparative Ct method [105]. For the measurement of human samples, the housekeeping genes ACTB, GAPDH, B2M, TBP, SRSF4 or RPL41 were used for normalization. In case of murine samples, ACTB and GAPDH were used. For the

analysis of gene expression in tissue samples a panel of housekeeping genes (B2M, RPL41, SRFS4, TBP) was analyzed using the geNorm algorithm to find the most stable reference gene [106].

Table 17: qPCR master mix.

Reagent	Volume	Final concentration
2x SYBR Green Mix	5 µl	50 %
Forward primer [10 µm]	0.3 µl	0.3 µM
Reverse primer [10 µm]	0.3 µl	0.3 µM
cDNA (1:50)	2 µl	
dH_2O	2.4 µl	

Table 18: Thermocycler conditions for qPCR and melting curve.

Part	Description	Temperature	Time	Cycles
qPCR	Initial denaturation	95°C	15 min	1x
	Denaturation	95°C	15 s	40 x
	Annealing and elongation	60°C	60 s	
Melting curve	Denaturation	95°C	15 s	1x
	Annealing	60°C	30 s	
	Dissociation	60-95°C	0.5°C/s	
	Final denaturation	95°C	15 s	

Oligonucleotides for qPCR analysis used in this study were synthesized by Thermo Fisher Scientific and are listed in table 19.

Table 19: qPCR primer sequences.

Gene name	Accession number	Forward primer (5'-3')	Reverse primer (5'-3')
human			
ACTB	NM_001101	GACAGGATGCAGAAGGAGAT	GATCCACATCTGCTGGAAGG
ANKRD1	NM_014391	AGTAGAGGAACTGGTCACTGG	TGGGCTAGAAGTGTCTTCAGAT
B2M	NM_004048	CACGTCATCCAGCAGAGAAT	TGCTGCTTACATGTCTCGAT
CTGF	NM_001901	CCAAGGACCAAACCGTGG	CTGCAGGAGGCGTTGTCAT
CYR61	NM_001554	AGCCTCGCATCCTATACAACC	TTCTTTCACAAGGCGGCACTC
DNMT1	NM_001379	GAGTATGCGCCCATATTTGG	GTTCAAGTTGAGGCCAGAAG
DSG1	NM_001942	GGAGACTTTGTAGCTACTGA	CCTCCGAGCATATTGTACTG
DSG2	NM_001934	CACAGCAGCTACACTTTGAC	CATCGAACACTTTTATGCGC
GAPDH	NM_002046	CTGGTAAAGTGGATATTGTTGCCAT	TGGAATCATATTGGAACATGTAAACC
RPL41	NM_001035267	AAACCTCTGCGCCATGAGAG	AGCGTCTGGCATTCCATGTT
SHP1	NM_002831	GAACAAGAAGCAGGAGTCCG	CGCTGGTGCAAGTTCTTCAC
SRSF4	NM_005626	TGCAGCTGGCAAGACCTAAA	TTTTTGCGTCCCTTGTGAGC
TBP	NM_001172085	CCGGCTGTTTAACTTCGCTT	ACGCCAAGAAACAGTGATGC
VASP	NM_003370	GATGATGGCAACAAGCGATG	GGACGATGGCACAGTTGATG
YAP	NM_006106	CCTGCGTAGCCAGTTACCAA	CCATCTCATCCACACTGTTC
murine			
ACTB	NM_007393	GCTTCTTTGCAGCTCCTTCGT	ACCAGCGCAGCGATATCG
DSG2	NM_007883	GGAGAACTGAACATCACTAG	CTTTGATGCGTAGTTCCAAG
GAPDH	NM_001289726	TGTCCGTCGTGGATCTGAC	CCTGCTTCACCACCTTCTTG
VASP	NM_009499	GAGTTGTTGGCCGCAAGATG	GCCTGATTGTACTTGACACC

3.7 Methods of protein biochemistry

3.7.1 Protein isolation

For isolation of proteins from cultured cells, medium was removed and cells were washed with PBS. Cells were scraped with 1x Cell Lysis buffer (Cell signaling) supplemented with 1x Protease inhibitor Mix G (Serva, Heidelberg, Germany) and 1x PhosStop (Sigma-Aldrich). For complete disruption of cellular membranes, samples were sonicated 3-times for 30 s in an ultrasound water bath, with 1 min cooling steps on ice in between. Afterwards, cell debris was pelleted at 15,000 x g at 4°C for 10 min. Protein-containing supernatant was transferred into a new reaction tube and protein concentrations and purity were determined using a NanoDrop spectrophotometer measuring the absorption at 280 nm. Storage of the protein lysates was performed at -20°C.

3.7.2 SDS-polyacrylamide gel electrophoresis and Western immunoblotting

Proteins were separated according to their molecular weight via sodium dodecyl sulfate polyacrylamide gel electrophoresis (SDS-PAGE) using 8% Tris-glycine SDS-polyacrylamide gels (Stacking gel: 30% acrylamide mix, 1.0 M Tris pH 6.8, 10% SDS, 10% APS, 1% TEMED; Resolving gel: 30% acrylamide mix, 1.5 M Tris pH 8,8, 10% SDS, 10% APS, 0.8% TEMED) with SDS running buffer (25 mM Tris, 192 mM Glycine, 0.1% SDS). Before loading onto the gels, 200 µg of protein samples were prepared with 4x protein loading buffer (250 mM Tris-HCl pH 6.8, 8% SDS, 40% glycerol, 0.04% bromphenol blue, 100 mM DTT), adjusted with MilliQ H2O to 30 µl and boiled at 95°C for 5 min. Fisher's EZ Run™ Pre-Stained *Rec* Protein Ladder (Thermo Fisher Scientific) was used as protein size marker. The gel was first run for at 80 V for 15 min and then at 120 V for 90 min. In the next step, separated proteins were transferred onto nitrocellulose membranes. For this, a blotting "sandwich" was assembled consisting of three filter papers, the membrane, the gel and again three filter papers. The blot was run at 130 V and 700 mA/chamber in borate blotting buffer (20 mM Boric acid, 1.27 mM EDTA) for 80 min. After blotting, the membrane was blocked in blocking solution (5% BSA in TBST (20 mM Tris-HCl, 140 mM NaCl, 0.1% Tween20)) for 1 h. Next, the membrane was incubated with first antibody in blocking solution overnight. The next day, the membrane was washed three-times with TBST and then incubated with the respective secondary antibody in blocking solution for 2 h, again followed by three washing steps. Fluorescence signals were detected and quantified using the Odyssey-CLx Infrared Imaging system with the ImageStudio Lite software. The proteins ACTB, GAPDH or Vinculin served as loading controls.

3.7.3 Subcellular protein fractionation

Cells were seeded at low density (300,00 cells/10 cm dish) and transfected with siRNAs as described (chapter 3.4.2). Subcellular protein fractionation was performed using the NE-PER™ Nuclear and Cytoplasmic Extraction Reagents kit (Thermo Fisher Scientific) according to the manufacturer's protocol. For further investigation, 20 µl of the isolated cytoplasmic and nuclear fractions were separated by SDS-PAGE and analyzed by Western immunoblotting (chapter 3.7.2). β-tubulin and PARP served as cytoplasmic and nuclear loading control, respectively.

3.7.4 Identification of protein binding partners - BioID-Assay

First, HLF cell lines with stable integration of vector that allow the inducible expression of proteins tagged to the promiscuous biotin ligase BirA were generated (chapter 3.5.3). Next, 2 x 10^6 cells were seeded on 15 cm dishes and treated with 1 µg/ml dox for 48 h and 50 µM biotin (Sigma-Aldrich) for 24 h. Cells were washed twice with PBS and scraped in 1 ml BioID lysis buffer (50 mM Tris pH 7,5, 200 mM NaCl, 0.1% SDS, 1% Triton X-100, 1 mM EDTA, 0.25% Na-desoxycholate). Protein lysates were sonicated 3-times in an ultrasound water bath for 30 s, with cooling steps on ice in between for 1 min. After centrifugation at 15,000 x g at 4°C for 10 min, supernatant was added to 50 µl of streptavidin magnetic beads (Dynabeads MyOne Streptavidin C1, Thermo Fisher Scientific), which were equilibrated twice with 200 µl BioID lysis buffer by using a magnetic separator. The suspension was rotated at 4°C overnight to form bead/protein complexes, followed by 5 washing steps: two steps with 500 µl BioID washing buffer 1 (2% SDS), one step with 500 µl BioID washing buffer 2 (50 mM Tris pH 7.5, 500 mM NaCl, 1% Triton X-100, 1 mM EDTA, 6.1% Na-desoxycholate), one step with 500 µl BioID washing buffer 3 (10 mM Tris pH 7.5, 250 mM LiCl, 0.5% Triton X-100, 1 mM EDTA, 0.5% Na-desoxycholate) and finally one step with 500 µl PBS. Next, 20 µl 4x NuPAGE™ LDS sample buffer (Thermo Fisher Scientific) was added and proteins were eluted at 95°C for 10 min. Samples were loaded onto NuPAGE™ 4-12% Bis-Tris Mini-gels (Thermo Fisher Scientific) and electrophoresis was performed at 120 V for 10 min using NuPAGE™ MOPS SDS-Running buffer (Thermo Fisher Scientific) supplemented with DL-Dithiothreitol solution (Sigma-Aldrich). Samples were fixed using fixation solution (40% H_2O, 50% EtOH, 10% AcOH) for 20 min, stained with Quick Coomassie Stain (Protein Ark, Eching, Germany) for 10 min and de-stained in H_2O overnight.

All following steps were done in the Core Facility for Mass Spectrometry & Proteomics (CFMP) at the Center for Molecular Biology (ZMBH, Heidelberg University) headed by Dr. Thomas Ruppert. Sabine Merker was responsible for the sample preparation.

The reduction and alkylation of proteins were carried out by incubating gel pieces with 60 µl dithiothreitol (40 mM) in 50 mM tetraethylammonium tetrahydroborate buffer (TEAB, pH 8.5) at 57°C for 30 min followed by incubation with 60 µl iodoacetamide (59 mM) in 50 mM TEAB at 25°C in darkness for 20 min. After dehydration with 60 µl 100% acetonitrile (ACN), 30 µl trypsin solution (8 ng/µl in 50 mM TEAB) were added to the gel and incubated at 37°C overnight. After adding 20 µl of 0.1% trifluoroacetic acid (TFA), peptides were extracted by dehydration in 20 µl ACN twice and washed in 30 µl of 50 mM TEAB for 20 min. The collected supernatants were dried by vacuum.

For HPLC-MS analysis (Ultimate 3000 liquid chromatography system coupled to an Orbitrap QE HF, Thermo Fischer Scientific), samples were dissolved in 15 µl 0.1% TFA and loaded to an in-house packed analytical column (inner diameter 75 µm x 20 cm, CS-Chromatographie Service GmbH, Langerwhe, Germany) with a flow rate of 550 nl/min of HPLC solvent A (0.1% formic acid (FA) and 1% ACN) for 20 min. The peptide separation was done by using a linear gradient of HPLC solvent B (3-40% of solvent B (0.1% FA, 89.9% ACN) with a reduced flow rate of 300 nl/min for 60 min. The mass spectrometer was operated in data-dependent acquisition mode, automatically switching between MS and MS^2. MS spectra (m/z 400-1,600) were acquired in the Orbitrap at 60,000 (m/z 400) resolution. Fragmentation in HCD cell was performed for up to 15 precursors and MS^2 spectra were acquired at 15,000 (m/z 400) resolution.

The MS raw files were processed using the MaxQuant software version 1.6.12.0. MS^2 spectra were compared against the UniProt human proteome database (UP000005640_9606, fasta downloaded Nov 2019) and the contaminants database provided together with software. Cysteine carbamidomethylation was set as fixed modification. N-terminal acetylation, methionine oxidation and glutamine/asparagine deamidation were included as variable modifications. Trypsin/P was defined as the proteolytic enzyme and up to two missed cleavages were allowed. The maximum false discovery rate for proteins and peptides was set to 1% and the minimum peptide length was 7 amino acids. All other parameters were default ones from MaxQuant. The calculation of quantitative normalized ratios was done by MaxQuant. Data analysis was performed using Perseus software [107].

3.7.5 Co-immunoprecipitation (Co-IP)

For Co-IP experiments, 50 µl magnetic beads (Dynabeads® Protein G, Thermo Fisher Scientific) were equilibrated with 50 mM glycine (pH 2.8) for 5 min. Next, beads were resuspended in 200 µl PBST (PBS pH 7.4, 0.02% Tween-20), 2 µg of the respective antibody was added and the mixture was incubated for at 4°C with rotation for 4 h, followed by two washing steps with 500 µl PBST. Cells were seeded in 10 cm dishes. When reaching confluence, cells were harvested using 500 µl IP lysis

buffer (50 mM Tris-HCl pH7.4, 1% NP-40, 0.25% Na-desoxycholate, 150 mM NaCl, 1mM EDTA, 1x Protease inhibitor Mix G, 1 mM PMSF, 1 mM DTT) on ice for 10 min. Subsequently cells were scratched and cell lysates were incubated at 4°C with rotation for 15 min. After centrifugation at 14,000 x g at 4°C for 15 min, the supernatant (input) was added to the beads and incubated at 4°C with rotation overnight. The next day the beads were washed 3-times with 500 µl PBS using a magnetic separator. Finally, the bound proteins were eluted with 25 µl 4x sample buffer at 95°C for 10 min and analyzed by western immunoblotting (chapter 3.7.2). Beads with antibody but without protein were used as negative immunoglobulin G (IgG) controls.

3.7.6 Proximity ligation assay

The DuoLink *in situ* Proximity ligation assay (PLA) was performed according to the manufacturer's instructions (Duolink® In Situ PLA® Probe MINUS and PLUS + Duolink® In Situ Detection Reagent Orange, Sigma-Aldrich). In brief, cells were seeded on 18 mm glass coverslips in 12-well plates. When reaching 80% confluence, cells were washed 3-times with PBS und fixed with 4% PFA in PBS for 10 min. Next, cells were washed 4-times for 5 min with PBS and permeabilized with 0.1% Triton X-100 in PBS for 5 min, followed again by two 5 min-washing steps with PBS. Afterwards cells were blocked using the Blocking solution for 30 min and incubated with primary antibodies diluted in Antibody Diluent at 4°C overnight. The next day, cells were washed 2-times with Wash Buffer A for 5 min, followed by an incubation at 37°C with PLA-probes (MINUS and PLUS) diluted in Antibody Diluent for 1 h. Cells were washed twice with Wash Buffer A for 5 min and incubated at 37°C with the Ligation solution for 30 min, followed again by two 2 min-washing steps with Wash Buffer A. Next, the cells were incubated with the Amplification solution at 37°C for 100 min. Finally, cells were washed twice with Wash Buffer B for 10 min, once with 0.01x Wash Buffer B for 1 min and mounted on slides with DAPI Fluoromount-G (Southern Biotech, Birmingham, USA). Fluorescence images were acquired at 40x magnification with an Axioplan 2 microscope.

3.7.7 Immunofluorescence staining and analysis of cryosections

Cryosections of human livers and HCC tissues were provided by the Tissue Bank of the National Center for Tumor Diseases (NCT, Heidelberg, Germany) in accordance with the regulations of the tissue bank and the approval of the ethics committee of Medical Faculty of Heidelberg (approval number: S-376/2018).

In case of DSG1 and VASP staining, cryosections were fixed in 4% PFA in PBS for 20 min. In case of DSG2 staining, cryosections were fixed in cold methanol for 10 min, followed by 10 min in cold

acetone and air dried for 20 min. Next, cryosections were permeabilization with 0.2% Triton X-100 in PBS for 10 min, washed with PBS and incubated with the primary antibody diluted in antibody dilution buffer (Invitrogen) at room temperature for 1 hour. Afterward, slides were washed with PBS followed by an appropriate secondary antibody incubation at room temperature for 1 hour. Subsequently, slides were washed with PBS, dried and mounted with DAPI-containing Fluoromount-G. Fluorescence images were acquired at 40x magnification with an Axioplan 2 microscope.

The intensity of stains was analyzed in an automatic manner using Fiji macro functions [108]. The DSG1/DSG2/VASP tissue stains were segmented by applying Trainable Weka Segmentation algorithm [109]. The resulting probability maps were thresholded. These masks were overlaid with the original DSG1/DSG2/VASP intensity data obtaining stain intensity per image. Subsequently, the mean intensity of the DSG1/DSG2/VASP in HCC samples was compared with the stain intensity in the liver samples.

3.7.8 Immunofluorescence staining of cultures cells

For immunofluorescence, cells were seeded on 18 mm glass coverslips, pre-coated with PLL (Poly-l-lysine hydrobromide, Sigma-Aldrich) solution (25 µg/ml) for 20 min and air-dried for 10 min. Cells were seeded on coated coverslips (chapter 3.4.2), followed by siRNA transfection (chapter 3.4.3). Cells were fixed with 4% PFA in PBS for 15 min and permeabilized with 0.2% Triton X-100 in PBS for 7 min. After washing with PBS, cells were blocked with 0.1% BSA in PBS for 30 min, followed by three 5 min-washing steps with PBS. Next, cells were incubated with primary antibodies diluted in PBS for 1 h, washed 3-times for 5 min with PBS and incubated with secondary antibodies, diluted in PBS for 1 h. Finally, cells were again washed with PBS, incubated for 5 min with 100% EtOH and mounted on slides with DAPI-containing Fluoromount-G. Fluorescence images were acquired at 40x magnification with an Axioplan 2 microscope.

3.7.9 Immunohistochemistry (IHC)

IHC staining was performed by the IHC research facility at the Institute of Pathology, Heidelberg (CMCP, head: Dr. Tanja Poth).

In brief, formalin-fixed, paraffin-embedded (FFPE) tissue sections were cut into 2 µm thick sections and mounted on microscope slides. Samples were deparaffinized with xylene three times for 5 min, followed by rehydration in 100% ethanol twice for 2 minutes, 95% ethanol for 2 minutes twice and 70% ethanol for 2 minutes twice and finally rinsed with distilled water. Antigen retrieval was

performed by either steamer (epitope: GFP) or pressure cooker (epitopes: Ki67, VASP, YAP) with Citrate target retrieval buffer (pH 6). Tissue sections were cooled down, washed with TBS and subsequently incubated with the primary antibody diluted in antibody dilution buffer (Dako) overnight, followed by washing with TBS three times for 5 min. Next, the Enhancer Detection Line followed by washing with TBS and AP-Polymer Detection Line incubation was applied. Alternatively, biotinylated antibody was applied for 30 min, followed by washing with TBS and incubation with Streptavidin-HRP. Slides were washed twice with TBS. Subsequently, permanent AP Red Kit or AEC (3-amino-9-ethylcarbazole) were used for signal detection. Slides were digitalized using the digital slide scanners Aperio AT2 with a 40x magnification.

3.8 Functional assays

3.8.1 Cell viability assay

To analyze cell viability, equal numbers of cells were seeded at 48-well plates and transfected with gene-specific siRNAs or induced with dox as described (chapter 3.4.3 + 3.4.6). Resazurin reagent (Bio-Techne GmbH, Wiesbaden, Germany) was added 1:10 to the cell culture medium at the indicated time points, followed by incubation at 37°C for 1 h. Supernatant was transferred to a 96-well plate and light emission was measured using a FLUOstar Omega microplate reader (excitation wavelength: 544 nm, emission wavelength: 590 nm).

3.8.2 Cell proliferation assay

To analyze effects on cell proliferation after gene-specific knockdown or gene overexpression, identical numbers of cells were seeded in 96-well plates 24 h after treatment. BrdU-ELISA assay (Cell proliferation ELISA Biotrak System, GE Healthcare) was performed according to the manufacturer's instructions after 72 h. Absorbance was measured at 450 nm using a FLUOstar Omega microplate reader.

3.8.3 Cell migration assay

To analyze effects on migration, 24 h after gene-specific knockdown 5 x 10^4 cells were seeded in transwell inserts (Falcon® Permeable Support for 24-well Plate with 8.0 µm Transparent PET Membrane, Corning, Kaiserslautern, Germany) in FCS-free medium. Inserts were placed into

receiver wells (Falcon® 24-well Cell Polystyrene Permeable Support Companion Plate, Corning) containing standard growth medium. After incubation at 37°C for 18 h, medium was aspirated and the inner part of the inserts was cleaned from remaining cells. Cells on the outer side of the membrane were fixed by adding 100% ice-cold Methanol for 10 min and stained with crystal violet stain solution for 1 h. Pictures were taken using an Olympus BX53 microscope at 10x magnification. The area covered by cells was quantified using the software Fiji with the macro 'migration counting'.

3.8.4 Cell invasion assay

For the analysis of cell invasion, spheroids were generated 24 h after siRNA transfection. For this, $1x10^5$ cells were resuspended in 4 ml medium containing 20% v/v 12 mg/ml methocel solution (Methylcellulose, Sigma Aldrich) and seeded as 'hanging drops' on the lid of a 15 cm cell culture dish. In total, 144 20 µl-drops were generated, each consisting of approximately 500 cells, and incubated at 37°C for 48 h to allow spheroid formation. In the next step, cavities of 24-well plates were pre-coated with 250 µl of a 1:1 mix of 1 mg/ml collagen/methocel. The collagen solution was prepared using PureCol (PureCol® Bovine Collagen I Solution, Advanced Biomatrix, Carlsbad, USA) and 1x DMEM (10x DMEM – low glucose, Sigma-Aldrich), diluted in deionized water. Spheroids were carefully harvested, resuspended in 250 µl collagen/methocel, transferred on the pre-coated wells and incubated at 37°C.

Image acquisition was done after matrix-polymerization (time point: 0 h) and 24 h after embedding the spheroids into the matrix with an Olympus IX81 microscope at 10x magnification, using the Olympus CellSens Dimension software. To quantify cell invasion the perimeter of the spheroids was determined using the Fiji software with the macro 'Spheroids'. By subtracting the spheroid area at time point 0 h from the area at time point 24 h, followed by normalization to the siRNA-transfected control, the relative cell invasion was calculated.

3.9 Mouse work

Male FVB/N mice were kept in barrier-maintained colonies in standard Makrolon type II breeding cages with an automated night and day rhythm. Housing and breeding were carried out at the IBF (Interfakultäre Biomedizinische Forschungseinrichtung, University of Heidelberg). All experiments were performed with the permission of the German Regional Council of Baden-Wuerttemberg (Karlsruhe, Germany) and the institutional regulations of the IBF (animal application number: G-87/19). For plasmid delivery into murine hepatocytes, the hydrodynamic tail vein injection

(HDTVI) technique was applied [110]. For this, pT3 expression vector-combinations of the different oncogenes (table 20) and sleeping beauty transposase-coding vector (pCMV-SB10) were diluted in 2 ml PBS and injected into the tail vein of eleven to twelve weeks old mice in less than 10 s. Mice were maintained and monitored twice weekly. Mice were sacrificed 5 weeks after injection by CO_2 anaesthetization. Mouse liver tissues were immediately collected and washed with PBS once. Liver samples were taken for formalin fixation and for storage at -80°C for further analysis.

Table 20: Plasmid combinations and concentrations for HDTVI.

Mouse group	pT3_c-MYC	pT3_DSG2	pT3_VASP	pT3_empty	pCMV-SB10
c-MYC	10 µg	-	-	10 µg	2 µg
DSG2	-	10 µg	-	10 µg	2 µg
VASP	-	-	10 µg	10 µg	2 µg
DSG2 + c-MYC	10 µg	10 µg	-	-	2 µg
VASP + c-MYC	10 µg	-	10 µg	-	2 µg

3.10 Human patient data analysis

For screening, expression data from two independent HCC cohorts were used; the HBV-positive HCC cohort (LCI cohort) consisting of 239 liver tissues and in part corresponding 242 HCC tissues [111], and the TCGA cohort consisting of 50 liver tissues and 372 HCCs [112]. The online tool Cutoff Finder was used to determine the optimal cutoff to subdivide patient data in two groups [113]. Independent cDNA samples from 10 HCC patients with corresponding liver samples were obtained from the NCT Heidelberg. For the analysis of copy number alterations in HCC patients, genomic TCGA data deposited in cBioPortal was investigated [114] [115]. For the comparison of liver cancer cell lines, expression data provided by Cancer Cell Line Encyclopedia was analyzed [116]. Gene expression profiling data from HepG2 cells after combined YAP and TAZ inhibition was analyzed [117]. Respective, cDNA samples after YAP/TAZ inhibition were provided by Fabian Rose.

3.10.1 HCC tissue-microarray analysis

The tissue samples used for the HCC tissue micro-array (TMA) analysis were surgically resected at the University Hospital of Heidelberg and histologically classified according to established criteria by experienced pathologists (Prof. Dr. Stephan Singer, Prof. Dr. Beate Straub). The TMA contained 40 non-tumorous liver tissues, 476 HCCs (grading: G1 = 87, G2 = 311, G3/4 = 78) and 174 cirrhotic liver tissues. The study was approved by the institutional ethics committee of the Medical Faculty of Heidelberg University (S-376/2018). For semi-quantitative IHC stain quantification, a score was

created according to the following scoring system: quantity (0: no expression; 1: <1% positive; 2: 1-9% positive; 3: 10-50% positive; 4: >50% positive cells) and intensity (0: not detected; 1: low; 2: moderate; 3: high). The product of quantity and intensity was calculated to yield the final score, which was used for statistical analysis. In case of YAP, the cytoplasmic and nuclear staining scores were evaluated separately and summed up for correlation analysis. For Ki67 stains, quantity scores were determined ranging from 1 (negative) to 4 (strong positive).

3.11 Statistical analysis

Statistical analyses were performed using GraphPad Prism software (Prism 8, San Diego, USA). Data are shown as mean ± standard deviation (SD). Statistical comparison between two groups was performed using the non-parametric Mann-Whitney U test, the non-parametric Wilcoxon test for matched pairs and the parametric paired t-test. For multiple group comparison either the two-way ANOVA, the RM one-way ANOVA or the ordinary one-way ANOVA was applied. Survival analysis was performed using the Kaplan-Meier method with Log-rank test. For each experiment, the respective test is indicated in the figure legend. For correlation analysis the Spearman correlation coefficient was calculated. Significance levels are defined as: ns – not significant, * $P \leq 0.05$, ** $P \leq 0.01$, *** $P \leq 0.001$.

3.12 Software

Used software in this study is listed in table 21.

Table 21. Software and webpages used in this study.

Software	Provider
Adobe® Photoshop® CS5	Adobe Systems, San José, USA
ApE v2.0.61	https://jorgensen.biology.utah.edu/wayned/ape
Aperio ImageScope v12.4.3.7001	Leica Biosystems, Nussloch, Germany
BioRender	https://biorender.com
cBioPortal webpage	https://www.cbioportal.org/
Citavi 6	https://www.citavi.com/
CellSens Dimensions	Olympus
FIJI/Image J v1.53	www.fiji.sc
GraphPad Prism 9	GraphPad Software, San Diego, USA
Image Studio Lite v5.2	LI-COR Bioscience
Leica application Suite software	Leica Microsystems
Omega v 3.00 R2 and MARS	BMG Labtech, Ortenberg, Germany
Perseus v1.6.15	https://maxquant.net/perseus/
QuantStudio™ Design & Analysis Software v1.4.3	Thermo Fisher Scientific
R-4.1.0	www.R-project.org
RStudio v.1.4.1717	www.rstudio.com

4 Results

4.1 Screening strategy for the identification of dysregulated genes coding for junctional proteins in human HCC tissues

To answer which junctional structures may contribute to Hippo/YAP-dependent hepato-carcinogenesis, I performed a screening approach for the identification of potential candidates that are dysregulated on the transcript level in HCC patients (figure 4A). Therefor I investigated expression data derived from two independent HCC patient cohorts; the TCGA cohort, consisting of data from 372 HCC tissues and 50 non-HCC tissues and the LCI cohort, consisting of data from 242 HCC tissues with the respective surrounding non-HCC tissue [112] [111].

In the first step I defined a list of junctional and junction associated structures, in total 47 candidates. Here I focused especially on components of adherens junctions (e.g. cadherins, nectins) and desmosomes (e.g. desmocollins, desmogleins), but also adaptor proteins linking cell junctions with actin filaments (e.g. catenins, afadin) since it is known that actin polymerization affects Hippo/YAP pathway activity [118]. All genes included in this study are listed in supplement table 1. To identify dysregulated junctional messenger RNAs (mRNAs) in HCC, I analyzed the expression of this gene panel in HCC tissues compared to non-tumorous tissues (non-HCC) for both cohorts. To statistically compare these two groups I used the nonparametric Mann-Whitney U test, which ranks the values in each group and calculates a *P*-value depending on the discrepancy between the mean ranks [119]. The results illustrated that in the TCGA cohort 33/47 (70%) investigated mRNAs showed a significant up- or down-regulation in HCCs ($P \leq 0.05$), while for the LCI cohort 44/47 (94%) showed an aberrant expression. In total 31/47 (66%) of the analyzed transcripts revealed a significant dysregulation in both cohorts and were therefore selected for further analysis (figure 4A, upper intersection analysis).

Since I wanted to select clinically relevant candidates which potentially play a role in carcinogenesis, in the next selection step I associates the data with clinical outcome. Therefor I divided the HCC-patients into two groups according to low or high mRNA abundance and tested if candidate gene expression statistically associated with patient survival (Kaplan-Meier method with Log-rank test). To determine the optimal cutoff to subdivide patient data in the two groups, I used the Cutoff Finder [113]. In case of the TCGA cohort, 17/31 (55%) of the selected genes showed significant differences in patient survival between both patient groups, while for the LCI cohort 19/31 (61%) genes showed statistically relevant differences. Importantly, 12/31 (39%) genes were consistently regulated in both patient cohorts and used for further analysis (figure 4A, middle analysis).

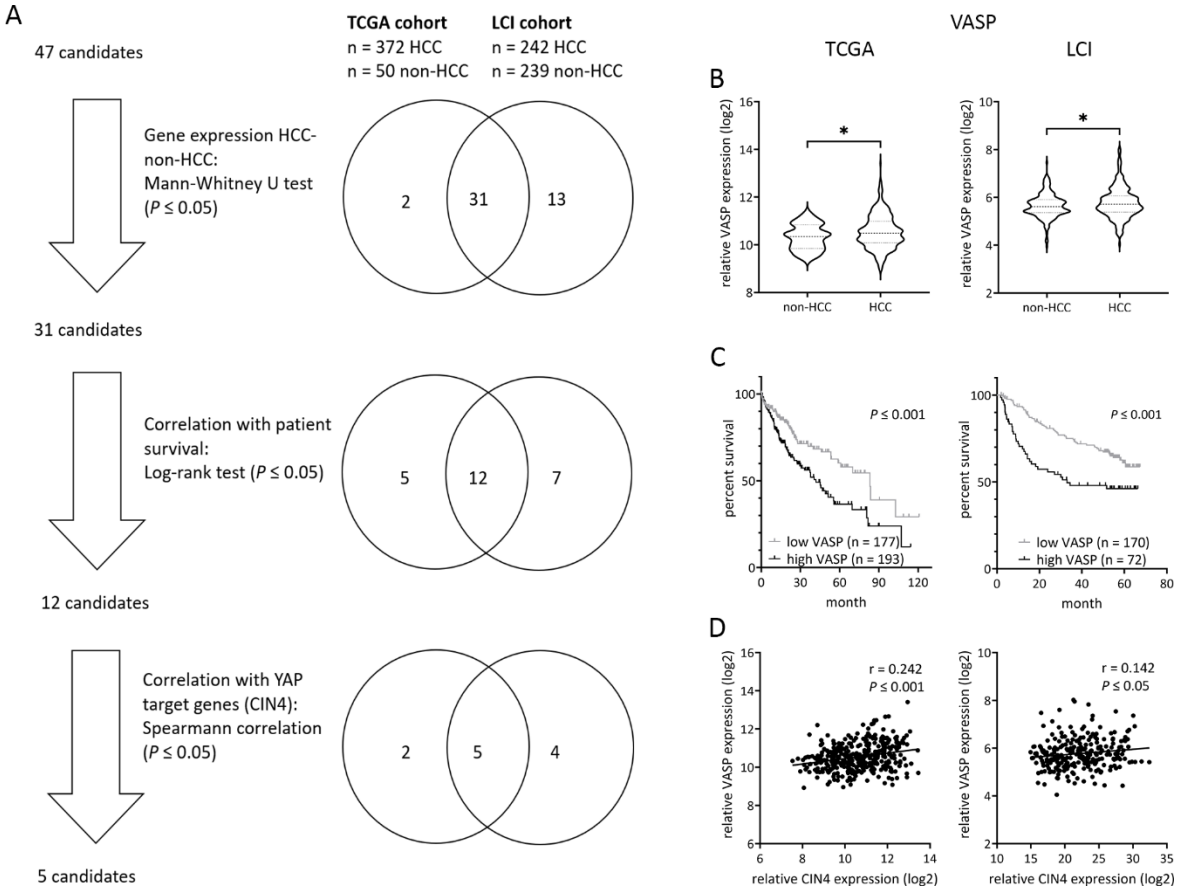

Figure 4: Screening strategy for dysregulated junctional mRNAs in human HCC tissues. (A) Schematic screening approach to identify junctional factors for further analysis. Expression data from two independent HCC patient cohorts (TCGA, LCI) are used to analyze the expression of a pre-selected panel of junctional genes in HCC. **(B)** Expression of VASP in HCCs compared to non-tumorous liver tissues in TCGA and LCI cohorts. The Mann-Whitney U test is used for group comparison. * $P \leq 0.05$. **(C)** The Log-rank test is utilized to analyze patient survival, comparing survival of patients with high and low expression of VASP. **(D)** HCC expression data for VASP are correlated with YAP-dependent CIN4 gene signature expression, which serves as a marker for YAP activity. Spearman correlation coefficient r and *P*-values are calculated.

In the next step I wanted to select those candidates, for which a possible link with Hippo/YAP signaling pathway activity was indicated. Therefore, as a last selection criterion, I correlated the expression of the remaining 12 candidates with the expression of YAP induced target genes, the so-called CIN4 gene signature. This signature consists of the four genes minichromosome maintenance protein 2 homolog (MCM2), mitotic arrest deficient 2-like protein 1 (MAD2L1), phosphotyrosine picked threonine-protein kinase (TTK) and targeting protein for Xklp2 (TPX2), which are transcriptionally regulated by YAP and here served as a marker for YAP activity [61] [60]. For calculation of the signature score, the expression values of the CIN4 genes were summarized und the sum was correlated with candidate gene expression. The Spearman correlation coefficient (r) indicated that 11/12 candidate genes showed a statistically significant association with CIN4; two exclusively in TCGA (17%), four in LCI (33%) and five in both cohorts (42%) (figure 4A, lower

intersection analysis). The group of consistently regulated candidate genes included DSG1 and DSG2, actin associated vasodilator-stimulated phosphoprotein (VASP) and CTNNA2 and CTNNA3. Since α-catenins were already described to regulate Hippo/YAP signaling [120] [121] and also characterized in HCC [122] [123], I decided to focus on VASP, DSG1 and DSG2 for further analysis.

The factor VASP is an actin-binding protein, which is a member of the Ena-VASP protein family and promotes actin filament elongation [124]. The analysis of both HCC cohorts illustrated that VASP expression was significantly upregulated in HCC tissues compared to non-HCC tissues (figure 4B). Second, Kaplan Meier survival analysis revealed a worse clinical outcome for patients with high VASP expression compared to patients with low VASP levels (figure 4C). Lastly, VASP expression positively correlated with YAP induced CIN4 gene signature (figure 4D), as indicated by Spearman correlation coefficient. Thus, high level expression of VASP could serve as a molecular event that contributes to YAP activation in the process of liver carcinogenesis.

The two selected candidates DSG1 and DSG2 are calcium-binding transmembrane glycoproteins and represent major components of desmosomes. Together with DSG3 and DSG4 they belong to the same family of desmosomal cadherins and cluster in close proximity on the same locus on chromosome 18 [125] (figure 5A). Interestingly, despite the low distance of about 180 kbp between the DSG1 and DSG2 genes, the transcripts of both factors were inversely regulated in HCC tissues (figure 5B). While DSG1 mRNA levels were strongly decreased in cancer tissues compared to non-tumorous livers, DSG2 levels were increased (LCI cohort) or showed elevated expression in subgroup of tumors (TCGA cohort). Equally, reduced DSG1 and elevated DSG2 mRNA concentrations statistically associated with worse clinical outcome. Lastly, a statistically significant negative (for DSG1, $r = -0.441$, $r = -0.369$) and positive (for DSG2, $r = 0.485$, $r = 0.436$) correlation with the YAP target gene signature CIN4 suggested a possible mechanistic link between both factors and Hippo pathway activity. Since DSG1 and DSG2 inversely correlated with CIN4, I analyzed whether the candidates also correlate with each other (figure 5C). Indeed, there was a moderate negative correlation between the DSG1 and DSG2 family members in TCGA ($r = -0.202$) and LCI ($r = -0.261$) cohort observable. The differential expression of DSG family members in HCC tissues caused by special interest as there might be the possibility that also other DSG family members such as DSG3 were dysregulated in liver cancer. The analysis of DSG3 expression data revealed significantly decreased expression of DSG3 in HCC only in the LCI cohort but not the TCGA cohort (figure 5B). Equally, survival analysis and correlation with CIN4 did not lead to any significant results. DSG4 was not even identified in the investigated cohorts. These results suggested that there might be specific mechanism leading to inverse DSG1 and DSG2 expression with direct impact on YAP activity.

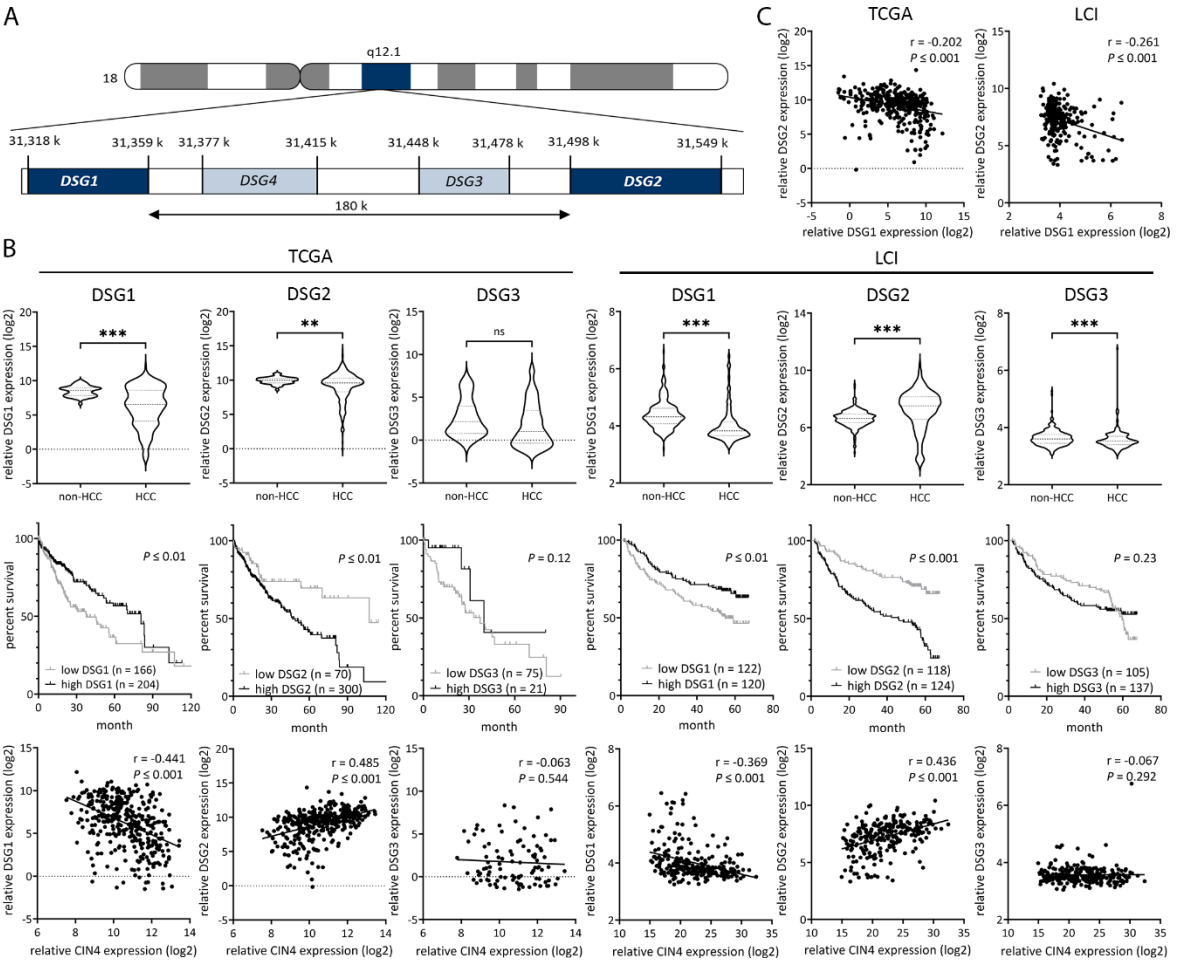

Figure 5: Expression of DSG1 and DSG2 in HCC cohorts. (A) The genomic locus of the desmosomal gene family indicates a close proximity of DSG gene family members on chromosome 18. **(B)** The expression of three desmosomal cadherins in HCC is compared with liver (non-HCC), using the Mann-Whitney U test. ** $P \leq 0.01$, *** $P \leq 0.001$, ns – not significant. The Log-rank test is utilized to analyze patient survival, comparing survival of patients with high and low expression. Correlation between the CIN4 gene signature and selected junctional genes **(B)** or correlation between DSG1 and DSG2 **(C)** in HCC samples is analyzed performing Spearman correlation analysis (r and *P*-values are indicated). All analyses are performed for DSG1, DSG2 and DSG3 in TCGA and LCI cohort.

In summary, by using expression data from primary human HCCs, I selected cell junction-associated factors (VASP, DSG1, DSG2), which are dysregulated in HCCs compared to non-malignant livers. Overexpression (VASP, DSG2) or repression (DSG1) of these factors associates with poor clinical outcome and the expression of typical YAP target genes. This led me conclude that these factors might represent upstream regulators of Hippo pathway activity in hepatocarcinogenesis.

4.2 Copy number alteration or promotor methylation cannot explain the expression of DSG1 and DSG2 in HCC cells

Analysis of TCGA and LCI HCC patient expression data cohorts revealed an inverse expression of DSG1 and DSG2 in HCC cells (figure 5B-C). While DSG1 mRNA was consistently downregulated, DSG2 transcripts were induced (at least in one cohort). Based on this data, I planned to investigate if known molecular mechanisms such as genomic alterations or epigenetic changes can explain the observed differences. To analyze copy number alterations of human DSG family members in HCC patients, I utilized the genomic TCGA data deposited in cBioPortal [114] [115]. Next to DSG1 and DSG2 I additionally investigated the data for the tumor suppressor gene TP53 as a positive control, because it is known that this gene is carrying several genetic alterations such as point mutations or chromosomal alterations in HCC cells [126]. As expected, this analysis revealed different types of alterations for the tumor suppressor gene TP53 in 32% of cases (e.g., missense mutations or genomic deletions; figure 6A). In contrast, for the DSG1 and DSG2 genes one detectable amplification was documented (which translated to 0.6% and 0.8% of all cases), respectively. No genomic deletions for DSG1 or higher numbers of DNA amplifications for DSG2 were determined (figure 6B). With this observation I was able to exclude that genomic copy number alteration could explain the inverse regulation of DSG1 and DSG2 in human HCCs.

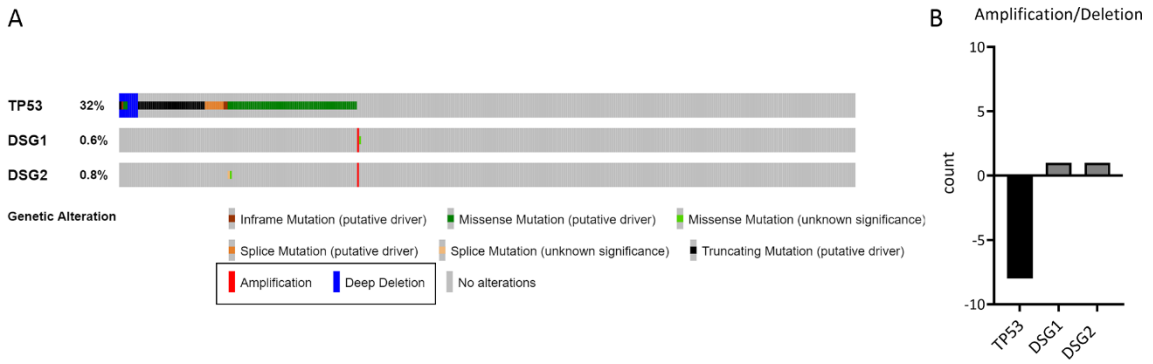

Figure 6: Overview of genomic alterations in DSG1 and DSG2 genes. Data from cBioPortal are utilized to analyze the portion of HCC patients with genetic alterations of the DSG1 or DSG2 genes. In total 372 patients are included in this analysis. **(A)** Detailed depiction of different types of genetic alterations in the investigated HCC patient cohort. The TP53 genes serve as a positive example, showing known deletions and genetic alteration, which are leading to the inactivation of this tumor suppressor gene. **(B)** Main focus is set on the number of patients showing chromosomal amplifications or deletions of the target genes.

Next, I investigated if promotor methylation might represent the cause for the inverse regulation. For this reason, I treated HCC cells with different concentrations of the methyltransferase inhibitor azacytidine, which reduces DNA methylation, and subsequently measured the expression of

candidate genes to check whether they were transcriptionally controlled by DNA methylation [127] [128] (figure 7). qPCR analysis of DNTM1 (DNA methyltransferase) levels showed an expected decrease, indicating that the treatment was successful. As additional control, I analyzed the expression of SHP1 (Src homology region 2 domain-containing phosphatase) which is characterized by an hypermethylated gene promoter [129] [130]. Indeed, qPCR results revealed an increase of SHP1 transcripts in a concentration-dependent manner. In contrast, for DSG1 and DSG2 I could not observe any changes in mRNA abundance, illustrating that promotor methylation is not a major cause for the differential expression of DSG family members in HCC cells.

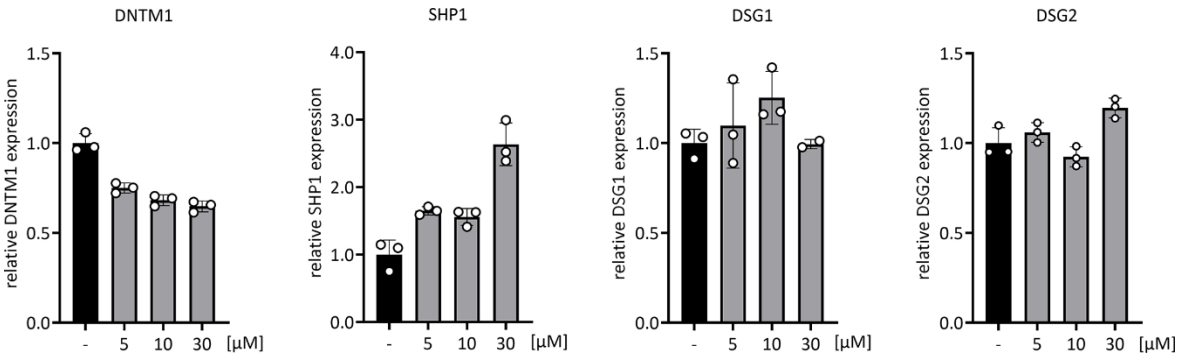

Figure 7: qPCR analysis of DSG1 and DSG2 mRNA after treatment of HCC cells with azacytidine. Huh7 cells are treated with different amount of methyltransferase inhibitor azacytidine (0 – 30 µM) for 48 h. RNA is isolated, reverse transcribed into cDNA and relative amount of DSG1 and DSG2 are measured using qPCR analysis. As indicated by the literature DNTM1 must be reduced while SHP1 should increase in the course of azacytidine treatment. One representative of three independent experiments is shown.

Lastly, I tested weather the activity of cellular signaling pathways may affect on DSG1 and DSG2 expression in HCC. Therefore, I treated HCC cells with siRNAs targeting main components of several pathways, such as AKT1/2, ERK1/2, STAT3 and NOTCH1. However, subsequent qPCR analysis did not reveal any changes of DSG1 or DSG2 expression after efficient silencing of these pathways (data not shown). Hence AKT/PI3K-, MAPK/ERK-, JAK/STAT- and Notch-signaling did not affect DSG1 and DSG2 expression and therefore could not explain the observed inverse expression of both factors.
To conclude, genomic alterations, gene promoter methylation, as well as the aberrant activation of different cellular signaling pathways can be excluded as causes for the inverse DSG1 and DSG2 expression in HCC cells. Other molecular reasons such as additional epigenetic regulation (e.g., histone modifications), the activation of other signaling pathways (e.g., the TGF-β receptor pathway) or the regulation by non-coding RNAs (e.g., micro-RNAs or long non-coding RNAs) might be involved. However, these aspects were not further investigated in this study.

4.3 Confirmation of altered DSG1, DSG2 and VASP expression in independent human HCC tissue cohorts

Investigation of two different HCC patient expression data cohorts revealed a dysregulation of DSG1, DSG2 and VASP at the mRNA levels. To reinforce these finding, I analyzed cryosections of human liver and HCC tissues, which were provided by the NCT (Nationales Centrum für Tumorerkrankungen, Heidelberg). I stained the frozen tissue slides for DSG1 (red), DSG2 (green) and VASP (green) using fluorophore-conjugated secondary antibody (figure 8A-C). A first semi-quantitative analysis of DSG1 staining intensities revealed a reduction of DSG1 in about 40% of HCC cases compared to liver tissues, while 8% showed an increase and about 52% of the tested cases did not show obvious alterations. In case of DSG2, about 32% of HCC tissue sections revealed in increase of the protein, 25% a reduction and 42% no alterations. Lastly, for VASP the majority (42%) of HCC sections showed increased VASP levels and 29% showed a reduction or no alterations, respectively. For a more objective comparison of the small patient cohort, the intensity of stains in HCC and liver tissues was automatically measured using the software Fiji [109] [108]. Subsequently, I statistically compared the stain intensities for HCC tissues with the stain intensities for liver tissues (figure 8A-C, graphs). Neither DSG1 nor DSG2 or VASP showed a statistically significant alteration of protein abundance in HCC compared to liver tissues. However, comparing the means of both groups revealed a good tendency of DSG1 reduction and DSG2 and VASP induction in HCCs. Due to the relatively low number of cases in this cohort (n = 9 – 25) and the high data variance, the results did not reach the level of significance; however, it confirms the tendency derived from LCI data set. To further confirm the altered expression for all three selected candidate genes on transcript level, I performed qPCR analysis of an independent HCC cohort consisting of cDNA samples from ten HCC patients with corresponding liver samples (figure 8D). As statistical test I used the nonparametric Wilcoxon test for matched pairs. qPCR analysis of DSG1 revealed a significant decrease of DSG1 in HCC samples compared to their corresponding liver samples (P = 0.0020). In case of DSG2, seven patients showed elevated DSG2 levels, while three showed a reduction; however, the results did not reach the level of significance (P = 0.2324). Investigation of VASP expression revealed a mixed picture with upregulation and downregulation in five cases each. For VASP the level of significance was also not reached (P = 0.4922).

In summary, I was able to confirm the inverse expression of DSG1 and DSG2 in HCC on protein as well as RNA levels. For VASP, only immunofluorescence analysis was able to confirm the results from the HCC expression cohort analysis. In part inconsistent results are likely due to the fact that the investigated cohorts are relatively small and that only a subgroup of patients is characterized by diminished DSG1 and elevated DSG2/VASP expression.

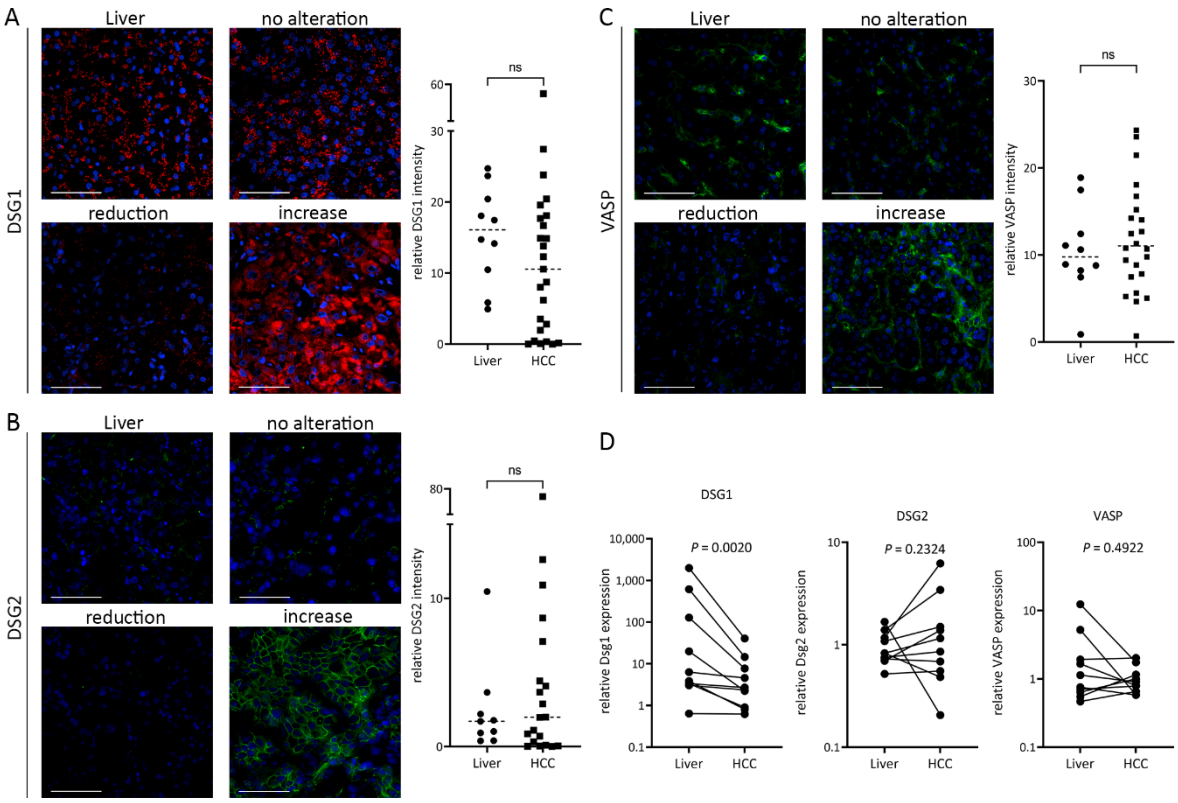

Figure 8: Confirmation of altered expression of DSG1, DSG2 and VASP in HCC. Frozen human HCC and liver tissue sections are stained for DSG1 **(A)**, DSG2 **(B)** or VASP **(C)** using immunofluorescence. Additional DAPI staining for the visualization of nuclei is performed. The intensity of stains is quantified using Fiji macro functions and compared between HCC and liver tissues. The Mann-Whitney U test is used for group comparison. For each candidate protein representative pictures of liver and HCC tissue are shown. Scale bar: 200 µm. ns – not significant. **(D)** qPCR analysis is used to compare DSG1, DSG2 and VASP mRNA expression in samples derived from ten HCCs and corresponding liver tissues. Statistical test: nonparametric Wilcoxon test for matched pairs.

4.4 Comparison of DSG1, DSG2 and VASP expression in various liver cancer cell lines

To further investigate the selected candidates from the screening approach I searched for appropriate cell lines for further analysis. For their selection I analyzed the expression of DSG1, DSG2 and VASP in various liver cancer cell lines, using data provided by Cancer Cell Line Encyclopedia (CCLE). The CCLE is a platform preprocesses and allows access to genetic data such gene expression data for more than 1,000 cell lines [116]. Data revealed that DSG1 was barely expressed in all analyzed liver cancer cell lines. In contrast, DSG2 and VASP transcripts were highly present in all tested cell lines (figure 9). Since expression of each candidate was very similar among the analyzed cell lines, I decided to continue with HepG2 and HLF cells. HepG2 is a well-differentiated human hepatocyte-derived human liver cancer/hepatoblastoma cell line, which

grows in highly polar cell aggregates. Therefore, it is an suitable *in vitro* model to study junctional proteins and how they modulate intracellular signaling [131]. HLF is a dedifferentiated and hepatocyte-derived human HCC cell line [132]. For both selected cell lines different transfection protocols for siRNAs and expression vectors existed, which qualified both lines for subsequent investigations.

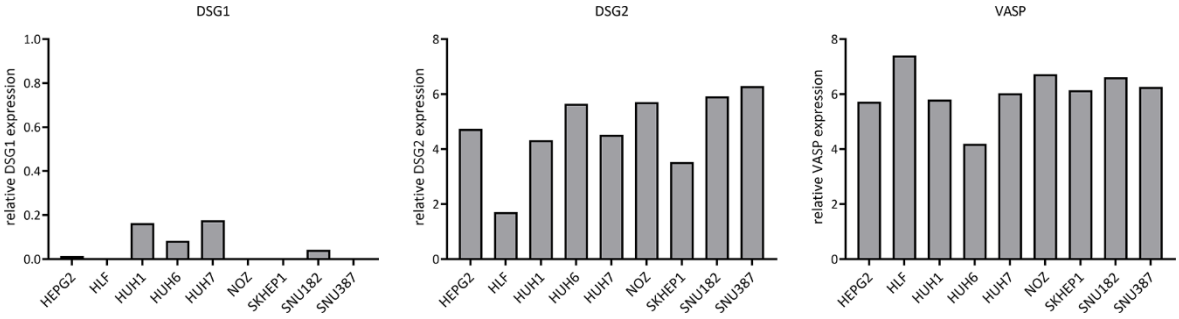

Figure 9: Relative DSG1, DSG2 and VASP expression in liver cancer cell lines. The expression of DSG1, DSG2 and VASP is investigated in various liver cancer cell lines using CCLE expression values for DepMap released cell line data.

4.5 DSG1 overexpression does not affect YAP activity, proliferation or viability

First, I investigated the influence of the candidate DSG1 on liver cancer cell functionality and its impact on YAP activity as the initial hypothesis for the selection process was that the candidates could control the Hippo pathway and/or YAP. My previous data showed that DSG1 mRNA and protein abundance was decreased in HCC tissues and that patients with low DSG1 levels were characterized by reduced survival and low YAP target gene expression (figure 5B). Therefore, I hypothesized that the absence of DSG1 negatively regulates Hippo signaling and thereby stimulates YAP activation, which subsequently could result in increased cell proliferation and viability. Accordingly, high abundance of DSG1 would lead to inactivation of YAP by increased phosphorylation and a reduction in vitality and proliferation. To test this hypothesis, I overexpressed DSG1 in HepG2 cells. For this, I generated a DSG1 doxycycline (dox)-inducible lentiviral expression vector (pT_DSG1), which allowed the efficient expression of human DSG1 48 h after dox administration (data not shown). Subsequently, I infected native HepG2 cells with viral particles and selected for cells with stable vector integration using puromycin. Western blot analysis revealed a robust induction of DSG1 expression compared to untreated control cells 48 h after dox administration (figure 10A). However, no significant changes for total YAP protein levels and YAP

phosphorylation (pYAP) were detectable. Equally, the analysis of RNA levels confirmed the overexpression of DSG1 after dox induction; however, expression of YAP and its known target genes CTGF, CYR61 and ANKRD1 were not affected (figure 10B). Together these results indicate that under the chosen experimental conditions overexpression of DSG1 did not affect YAP activity. Next, I wanted to investigate weather cell functionality was affected by DSG1 overexpression. For this I determined relative cell viability by using the resazurin assay after DSG1 induction. Again, dox treated cells didn't show any significant changes in comparison to untreated control cells for up to 72 h (figure 10C). These results were confirmed by a proliferation assay that revealed no significant effects on BrdU incorporation after DSG1 overexpression for 72 h (figure 10D).

In sum, *in vitro* overexpression of DSG1 in DSG1-negative liver cancer cells does not lead to changes in cell viability and proliferation and also YAP activity. Therefore, the initial hypothesis that DSG1 influences YAP activity and liver cancer cell functionality must be rejected. Thus, DSG1 was excluded as Hippo/YAP-regulating candidate in human hepatocarcinogenesis.

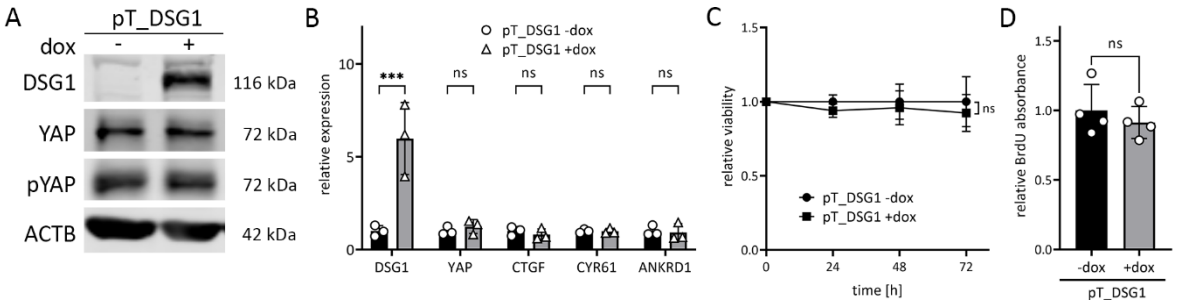

Figure 10: Analysis of cellular behavior after DSG1 overexpression. Dox inducible DSG1 overexpressing HepG2 cell lines (pT_DSG1) are treated with dox (+dox) to induce DSG1 overexpression. Untreated cells serve as a negative control (-dox). **(A)** Western immunoblot analysis of DSG1, YAP and pYAP level. ACTB serves as a loading control. **(B)** qPCR measurement of DSG1, YAP and YAP target (CTGF, CYR61, ANKRD1) RNA levels. **(C)** Viability of the cells is measured 24, 48 and 72 h post-dox induction. **(D)** Relative BrdU cell absorbance is measured 72 h after treatment. Biological triplicates **(B, C)** or quadruplicates **(D)** are shown as mean ± SD. Data are normalized on untreated control. For statistical analysis either the 2way ANOVA **(B, C)** or paired t-test **(D)** is used. *** $P \leq 0.01$, ns - not significant.

4.6 DSG2 and VASP siRNA inhibition affects cancer cell functionality

Since downregulation of DSG1 could be excluded as effector of the Hippo/YAP pathway and liver cancer cell behavior, I next focused on DSG2 and VASP, that were overexpressed in human HCCs and correlated with worse clinical outcome (figure 4B, 4C, 5B). I hypothesized that increased availability of DSG2 or VASP could support liver cancer cell properties such as proliferation, viability and active migration. To test my hypothesis, I designed DSG2- and VASP-specific siRNAs for transient silencing of the candidate genes (two independent siRNAs for each gene: si1 and si2). To

check weather inhibition was successful, I performed western blot analysis 48 h after siRNA transfection (figure 11A). Silencing of DSG2 leads to a strong reduction (up to 65-95%) of the protein levels in two tested liver cancer cell lines (HepG2 and HLF). Equally, for VASP a prominent protein reduction after transfection was observed after 48 h (up to 60-90%). As control, so-called scrambled siRNA that is not specific to any human gene was used (non-targeting control siRNA; NTC).

Next, I continued with functional analyses and performed viability assays using resazurin (figure 11B). Silencing of DSG2 leads to a significant 35%-decrease of viability for both siRNAs in HepG2 cells compared to treatment with control siRNA. In HLF cells, vitality reduction was less pronounced but still reached the level of significance (about 15%). In case of VASP siRNA inhibition, HepG2 cells showed the stronger effects compared to HLF cells with about 25% reduction of viability 72 h after transfection of siRNAs. Here the viability was reduced about 25%. In HLF cells viability decrease between 15-20% was observable. All together the results revealed that overall vitality of liver cancer cells was consistently decreased after efficient silencing of DSG2 or VASP.

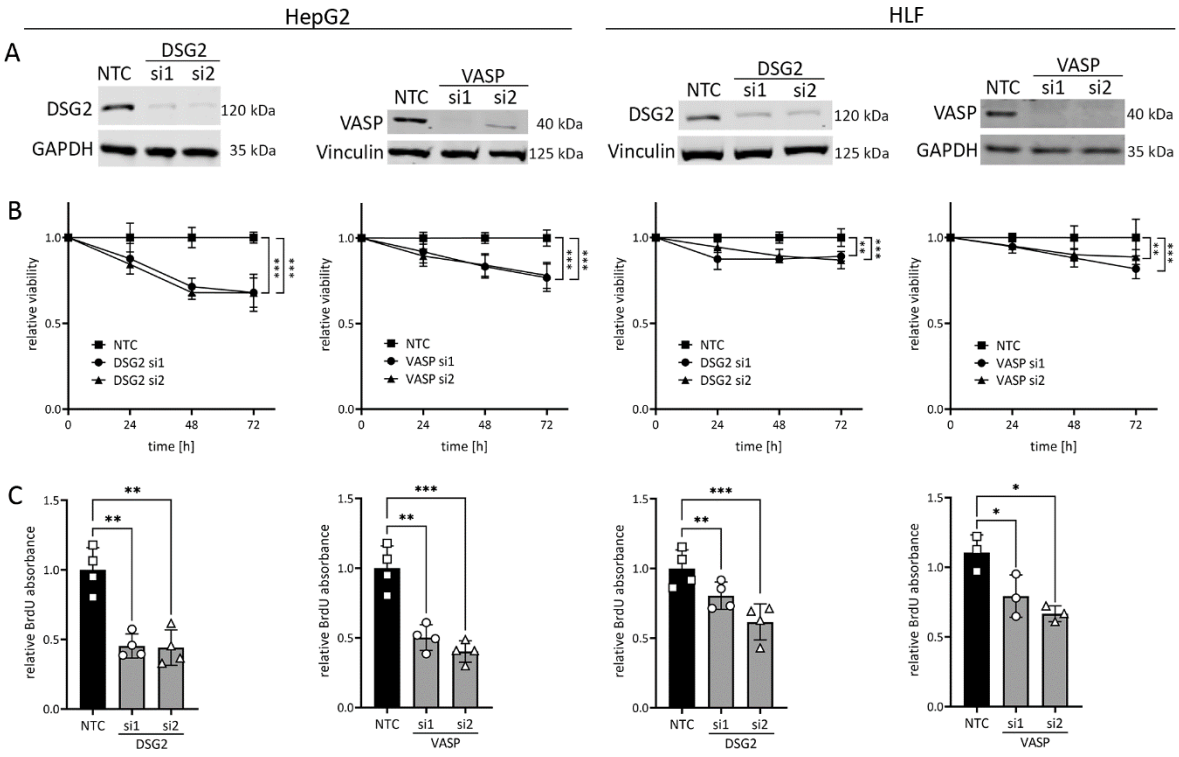

Figure 11: Analysis of cellular functionality after DSG2 and VASP silencing. HepG2 and HLF cells are treated with two different siRNAs specific for human DSG2 or VASP (si1, si2). Non-targeting control (NTC) siRNA is used as a negative control. **(A)** After 48 h western immunoblot analysis is performed to test for DSG2 and VASP knockdown efficiency. GAPDH and Vinculin serve as loading controls. **(B)** Viability of the cells is measured 24, 48 and 72 h post-treatment. **(D)** Relative BrdU absorbance is measured 72 h after siRNA treatment. Biological triplicates or quadruplicates are shown as mean ± SD **(B, C)**. Data are normalized on NTC. For statistical analysis either the 2way ANOVA **(B)** or RM one-way ANOVA **(C)** is performed. * $P \leq 0.05$, ** $P \leq 0.01$, *** $P \leq 0.01$.

Because the effects on cell viability were in some cases moderate, I performed additional experiments to confirm these findings. For this, I investigated the effects of DSG2 or VASP inhibition on cell proliferation and performed a BrdU ELISA 72 h after siRNA transfection (figure 11C). The results revealed that DSG2 inhibition led to a highly significant reduction of cell proliferation for HepG2 cells (about 60%) and a 20-40%-decrease for HLF cells. Analyzing relative cell proliferation after VASP silencing revealed a 50-60%-reduction for HepG2 and 30-40% for HLF cells. Taken together, inhibition of DSG2 or VASP leads to diminished proliferation of liver cancer cells. In general, the hepatoblastoma cell line HepG2 responded stronger than HLF. One possible explanation for this observation could be the high spatial polarity of the HepG2 cells [131], which could sensitize the cells for any kind of disturbance in three-dimensional structures or junctional complexes.

In the next step I wanted to investigate whether DSG2 and VASP can contribute to active cell mobility/migration. Since HepG2 cells grow in adherent aggregates this cell model was not suitable for any kind of mobility assay. First, I determined relative cell migration by performing the transwell assay (figure 12A - B). The pictures reveal a strong reduction of migration after DSG2 or VASP silencing, compared to the control treatment. For quantification of the total migration area, Fiji macros were used. Results reveal a 70-80% decrease after DSG2 and a 50-60% reduction after VASP silencing. For investigation if DSG2 or VASP also actively support cell invasion, I performed a spheroid assay and measured the perimeter of cell spheroids as proxy for the invasion in the surrounding matrix. Quantification of invasive capacity was performed using Fiji macros (figure 12C - D). Although identical cell numbers were used for the preparation of spheroids, analysis of the spheroids perimeter immediately after seeding (time point 0 h) revealed a diminished cell cluster size after DSG2 or VASP silencing, compared to the NTC controls. One explanation for this could be spatial changes of cells or cell-cell contacts, which might affect cell size and connectivity to neighboring cells. After 24 h, all spheroids were characterized by a clear spreading into the surrounding gel matrix. However, cell clusters from DSG2 or VASP siRNA-treated cells showed reduced invasion perimeters. Since the seeded spheroids already had smaller sizes, I considered their initial size for data calculation (normalized to the control spheroids at time point '0 h'). Despite this 'normalization', the results still indicated a 40-70% reduction of invasion after DSG2 inhibition and a 50-60% reduction after VASP silencing.

All together the results of the functional analyses illustrate that DSG2 and VASP positively affect liver cancer cell behavior. Both proteins support viability and proliferation but also cell dissemination *in vitro*.

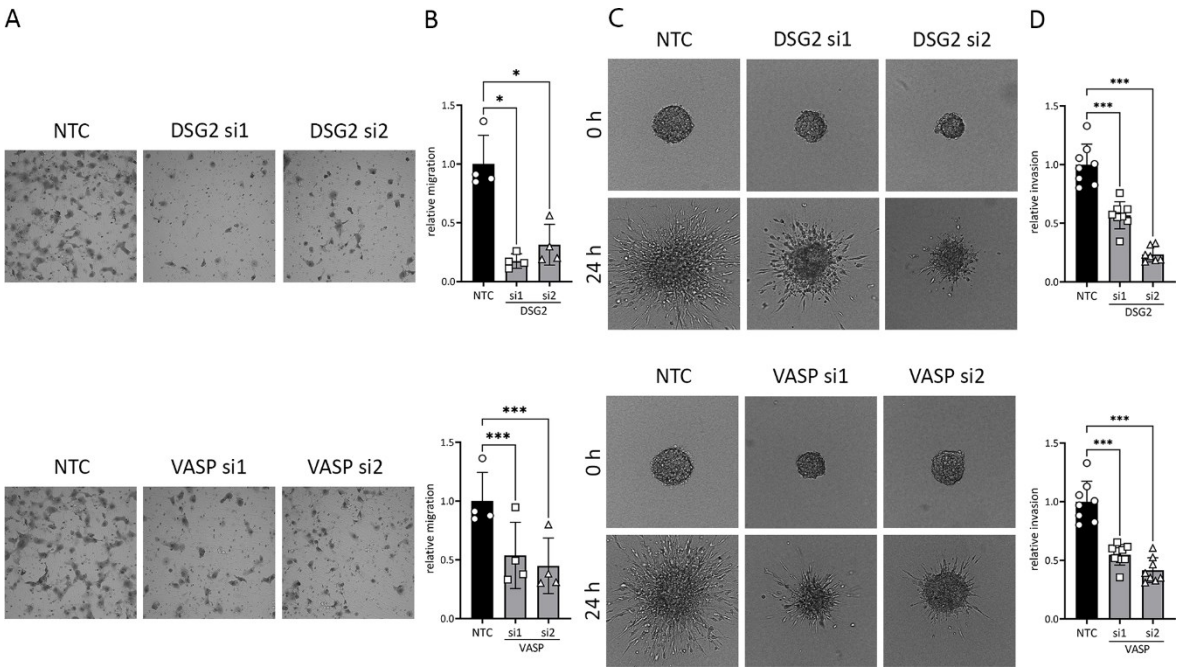

Figure 12: Investigation of cell migration (A) and invasion (B) after DSG2 and VASP knockdown. HLF cells are treated with two different DSG2- or VASP-specific siRNAs (si1, si2). NTC-siRNA is used as a negative control. **(A)** Exemplary pictures of transwell migration analysis are shown. **(B)** The total migration area of independent biological quadruplicates is quantified (mean ± SD). Data are normalized on NTC. For statistical analysis the RM one-way ANOVA is performed. **(C)** To measure invasion of cells, spheroids are generated and embedded in collagen gels. Pictures of single spheroids are taken immediately and 24 h after seeding. Exemplary pictures of spheroids are shown. **(D)** For quantification of invasion perimeter is measured as proxy. Time point 0 h is used as a blank and 24 h values are normalized on NTC. Each dot represents a single spheroid of a representative experiment. For statistical analysis the ordinary one-way ANOVA is performed. * $P \leq 0.05$, *** $P \leq 0.01$.

4.7 DSG2 and VASP control YAP activity

In the previous part of the project I was able to show that DSG2 and VASP support liver cancer cell functionality. However, another selection parameter for potential candidate genes was the association with the CIN4 gene signature, which is transcriptionally regulated by the oncogenic factor YAP. Indeed, the HCC expression data indicated a correlation between DSG2 or VASP expression and YAP target gene/CIN4 expression. Thus, DSG2 or VASP could affect the Hippo pathway via common or different molecular mechanism. To test this assumption, I transfected liver cancer cells with DSG2- and VASP-specific siRNAs and analyzed YAP, pYAP and target gene expression, as well as YAP localization.

DSG2 controls YAP activity

I started with the analysis of YAP after DSG2 inhibition. Indeed, Western immunoblot analysis confirmed clear inhibitory effects of DSG2 inhibition on YAP expression (figure 13A). The amount of

phosphorylated YAP was not affected. Calculation of the pYAP/YAP ratio suggested a threefold increase of pYAP in relation to total YAP (right panel). This was indicative for a YAP shift from the nucleus to the cytoplasm (phosphorylated YAP is accumulating in the cytoplasm). As protein levels of the YAP target genes CTGF and CYR61 were also diminished after DSG2 silencing, I concluded that DSG2 indeed positively controls YAP activity in HCC cells. This assumption was supported by qPCR analysis for different YAP target genes (figure 13B). CYR61, CTGF and ANKRD1 were significantly diminished after YAP inhibition. Depending on the DSG2-specific siRNA, the analyzed genes exhibited a transcript-reduction of 25-85% compared to controls.

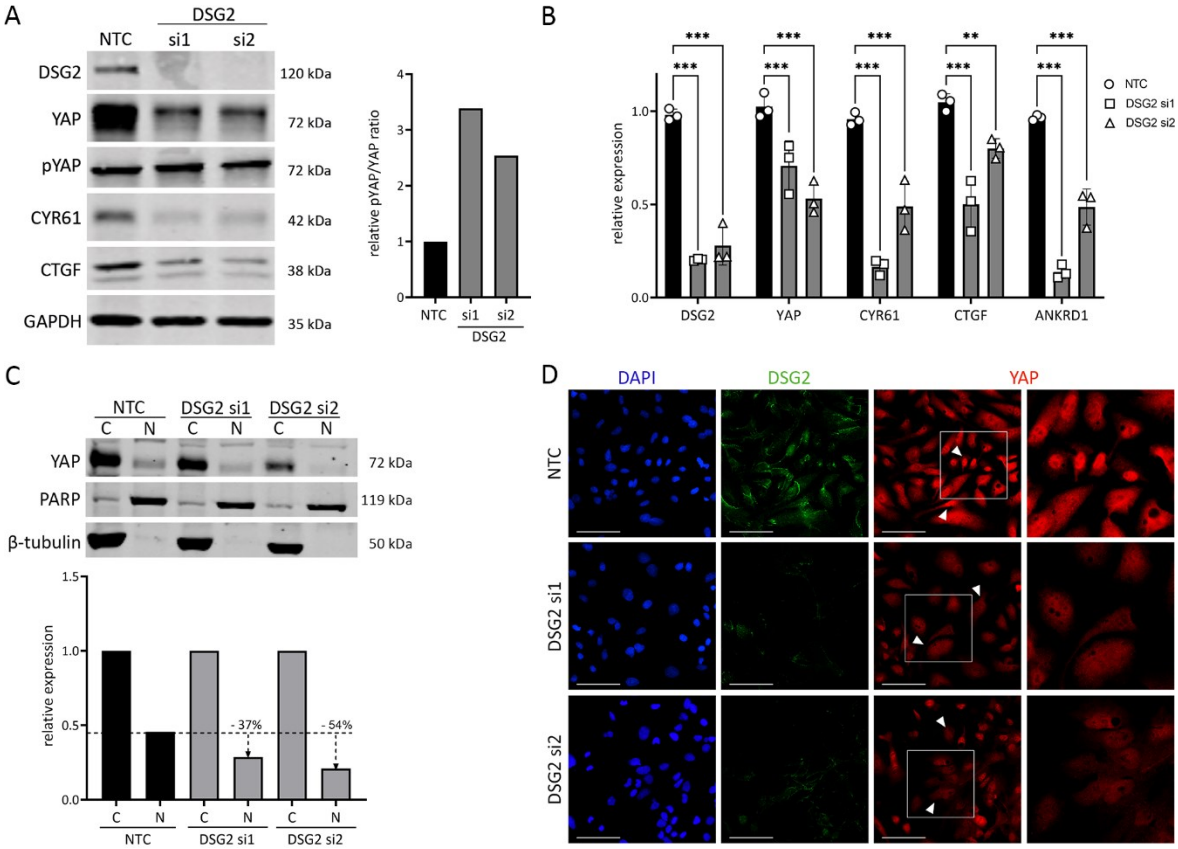

Figure 13: Analysis of YAP activity after DSG2 silencing. HepG2 cells are treated with two different DSG2 siRNAs (si1, si2) and NTC-siRNA as a negative control. **(A)** Western immunoblot analysis of DSG2, YAP, pYAP and YAP targets CYR61 and CTGF. GAPDH serves as loading control. YAP and pYAP level are quantified and a pYAP/YAP ratio is calculated and normalized to NTC. **(B)** qPCR measurement of DSG2, YAP and YAP target genes CTGF, CYR61 and ANKRD1 at the mRNA levels. Biological triplicates are shown (mean ± SD). Data are normalized on NTC. For statistical analysis the 2way ANOVA is performed. ** $P \leq 0.01$, *** $P \leq 0.01$. **(C)** Cells are harvested and cytoplasmic (C) and nuclear (N) protein fractions are isolated. YAP localization is determined by Western immunoblot. PARP serves as a nuclear and β-tubulin as cytoplasmic loading control. YAP levels are quantified and normalized on corresponding cytoplasmic fractions. Relative nuclear YAP reduction is calculated in comparison to NTC. **(D)** DSG2 and YAP expression and localization are analyzed by immunofluorescence. DAPI staining is performed for the visualization of cell nuclei. The white arrowheads indicate cells with high nuclear YAP level (upper panel) or with low nuclear YAP expression (lower panels). The framed squares are shown in higher magnification on the right panel. Scale bar: 200 µm.

Since YAP inactivation is linked to its cytoplasmic retention, I next investigated the subcellular YAP localization. Therefore, I isolated cytoplasmic and nuclear protein fractions after siRNA mediated DSG2 silencing (figure 13C). Indeed, analysis of YAP abundance indicated decreased nuclear YAP levels. To quantify the relative protein changes, nuclear and cytoplasmic YAP levels were quantified and nuclear YAP was normalized to the respective cytoplasmic fractions. The quantification confirmed that after DSG2 inhibition the relative amount of nuclear YAP decreases about 37-54%, which underlines the positive effect of DSG2 on the nuclear enrichment of YAP.

Lastly, I performed immunofluorescence stains for YAP after DSG2 silencing to further confirm the impact of DSG2 on the cellular YAP abundance (figure 13D). As indicated by my previous analyses, the visual analysis of YAP staining revealed a decrease of especially nuclear YAP after DSG2 inactivation (white arrowheads point to the individual cells). Together, these results confirm previous analyses that indicate a mechanistic link between DSG2 expression levels and YAP abundance and activity in HCC cells.

VASP controls YAP activity

Next, I analyzed the potential effects of VASP overexpression on YAP expression in HCC cells. After establishing an siRNA-mediated RNAi protocol, the concentration of YAP was measured by Western blot analysis (figure 14A). Although, the results illustrated prominent reduction of VASP after transfection of siRNAs, total YAP levels were not significantly affected. Instead, phospho-YAP levels were clearly elevated after VASP inhibition. Signal quantification a subsequent calculation of the pYAP/YAP ratio indicated a three- to fourfold increase after VASP inhibition compared to the NTC control (lower panel). However, the analysis of YAP target genes did reveal inconsistent results, for protein or mRNA levels (figure 14A+B). Also, immunofluorescence analysis did not show any detectable changes of YAP expression after VASP silencing (figure 14C). Thus, the in vitro data suggested that VASP did not control the total amount of YAP but affects its phosphorylation and therefore activity.

To substantiate these findings, I decided to investigate TMAs consisting of human HCC tissues (figure 14D). For this I established IHC stains for VASP and YAP and visually quantified the amount and intensity of VASP positivity as well as the nuclear enrichment of YAP in tumor cells. In addition, the TMAs were stained for the proliferation marker Ki67. Next, I correlated the VASP intensity with tumor dedifferentiation (grading), with semiquantitative scores for nuclear YAP, and the proliferation marker Ki67. The Spearman correlation coefficient revealed a moderate but significant statistical association of VASP with tumor dedifferentiation ($r = 0.136$; $P \leq 0.001$), Ki67 ($r = 0.150$; $P \leq 0.001$) and nuclear YAP ($r = 0.230$; $P \leq 0.001$).

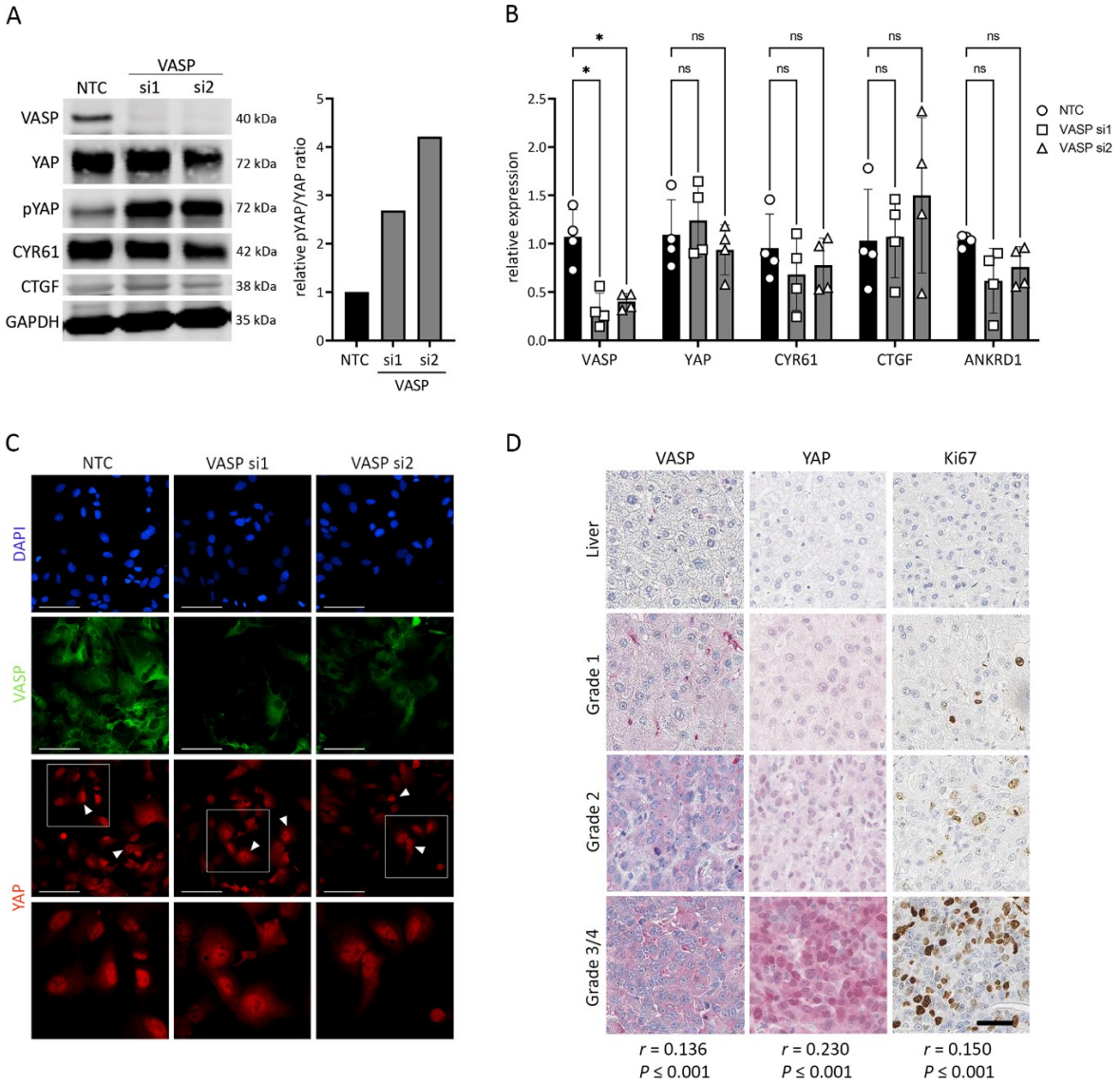

Figure 14: Impact of VASP on YAP activity. **(A)** HepG2 cells are treated with two different VASP siRNAs (si1, si2) and NTC-siRNA. VASP, YAP and pYAP levels are investigated using Western immunoblot analysis. GAPDH serves as a loading control. YAP and pYAP level are quantified and pYAP/YAP ratio is calculated and normalized to NTC. **(B)** qPCR measurement of VASP, YAP and YAP target genes CTGF, CYR61 and ANKRD1 at the mRNA levels. Biological quadruplicates are shown (mean ± SD). Data are normalized on NTC. For statistical analysis the 2way ANOVA is performed. * $P \leq 0.05$, ns - not significant. **(C)** VASP and YAP expression and localization are analyzed by immunofluorescence. DAPI staining is performed for the visualization of cell nuclei. The white arrowheads indicate cells with high nuclear YAP level (upper panel). The framed squares are shown in higher magnification on the bottom panel. Scale bar: 200 µm. (**D)** Analysis of VASP, YAP and Ki67 expression in human HCC tissue micro-array (TMA). In total, this TMA contained 40 non-malignant livers and 476 HCCs (grading: G1 = 87, G2 = 311, G3/4 = 78). Exemplary IHC stains of non-tumorous livers and HCC tissues of tumor grades 1, 2 and 3/4 are shown. Scale bars: 50 µm. Stains of VASP, nuclear YAP and Ki67 are visually quantified and the final scores are used for statistical analysis. Spearman correlation coefficient r and *P*-values are indicated.

In summary, DSG2 and VASP are effectors of YAP abundance or activity in HCC cells. Because the factors affect the total amount of YAP (DSG2) or its phosphorylation (VASP), distinct molecular mechanism might be involved in the regulatory process.

4.8 YAP does not affect DSG2 and VASP expression

The previous data confirmed that DSG2 and VASP are upstream regulators of YAP activity in HCC cells. I then asked if YAP itself controls DSG2 or VASP expression as this might be part of a feedback loop with different impact on gene expression of AJ constituents. To test this, I investigated gene expression profiling data from HepG2 cells after combined YAP and TAZ inhibition [117]. The results illustrated that neither DSG2 nor VASP transcript levels were significantly regulated after silencing YAP/TAZ with two different siRNA combinations (figure 15A). To further confirm these findings, I performed siRNA-mediated YAP/TAZ silencing experiments in HLF cells followed by qPCR analysis. Results verified the previous results showing no expression changes of DSG2 and VASP (figure 15B). In conclusion, DSG2 and VASP are not transcriptionally regulated by YAP, illustrating the absence of feedback regulation mechanisms.

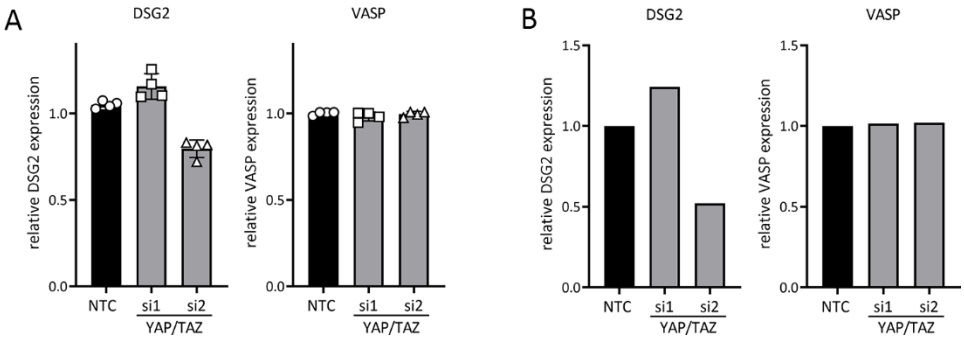

Figure 15: DSG2 and VASP expression analysis after YAP/TAZ inhibition. YAP/TAZ genes are silenced using two different siRNA combinations (si1, si2). NTC-siRNA serves as a negative control. **(A)** Gene expression profiling results for four samples with YAP/TAZ inhibition in HepG2 cells. DSG2 and VASP expression data are extracted from the data set and depicted. Biological quadruplicates are shown as mean ± SD. Data are normalized on NTC. For statistical analysis ordinary one-way ANOVA is performed. **(B)** Analysis of DSG2 and VASP expression after YAP/TAZ knockdown in HLF cells using qPCR. Expression data are normalized on NTC.

4.9 Dysregulation of DSG2 and DSG1 does not synergize in the regulation of liver cancer cell functionality

The previous result revealed a significant effect on cell behavior after DSG2 inhibition (figure 11 + 12). However, DSG1 overexpression didn't lead to obvious alterations in liver cancer cell functionality (figure 10C+D). Interestingly, I recognized an inverse expression of DSG1 and DSG2 in HCC expression data cohorts (figure 5C). This was substantiated by a statistical test that illustrated a moderate negative correlation (TCGA: r = -0.202, $P \leq 0.001$; LCI: r = -0.261, $P \leq 0.001$). This led to the question, weather combined and inverse DSG1 and DSG2 dysregulation could cooperate in the

regulation of pro-tumorigenic effects. For this reason, I investigated the viability of HepG2 cells with/without inducible DSG1 expression after transfection with/without DSG2 silencing. The successful genetic manipulation was tested by qPCR analysis (figure 16A). As already illustrated by my previous experiments, silencing with DSG2 specific siRNAs resulted in decreased cell viability (figure 16B). However, induction of DSG1 did not further increase or counteract these effects for up to 72 h. The inability of DSG1 overexpression to change cell proliferation with or without simultaneous DSG2 knockdown confirmed the cell viability results (figure 16C).

Together, the experiments show that simultaneous DSG2 inhibition and DSG1 overexpression do not cooperate or hamper each other in the regulation of liver cancer cell biology.

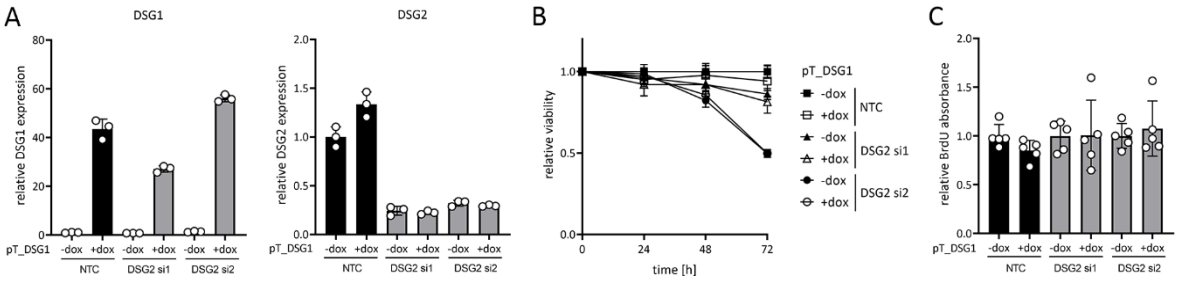

Figure 16: Analysis of cellular behavior after DSG2 inhibition with simultaneous DSG1 overexpression. HepG2 cells with dox-inducible DSG1 expression (pT_DSG1) are treated with dox (+dox) to induce DSG1 overexpression. Simultaneously cells are treated with two different DSG2 silencing siRNAs (si1, si2). Untreated cells (-dox) and NTC-siRNA serve as negative controls (-dox). **(A)** qPCR measurement of DSG1 and DSG2 RNA levels is done to test for the successful manipulation. Data are normalized on untreated NTC control. **(B)** Viability of the cells is measured 24, 48 and 72 h post treatment. Data are normalized to untreated NTC control. **(C)** Relative BrdU cell absorbance is measured 72 h after treatment. Data are normalized on -dox controls, each. One representative experiment out of three is shown as mean ± SD.

4.10 BioID-Assay – Identification of DSG2/VASP binding partners

Analysis of YAP localization, phosphorylation and YAP target gene expression after DSG2 and VASP silencing revealed that both candidates are effectors of YAP activity. Because first data indicated that the mode of action varies between DSG2 and VASP, the next step was to identify the existence of common or mutual exclusive molecular mechanisms. For this, I utilized an unbiased screening strategy to identify the interactome of DSG2 and VASP: the BioID assay. This technique allows proximity-dependent labeling and subsequent identification of proteins in living cells [133] (figure 17A). For this, human cDNA is cloned into an expression vector that contains a dox-inducible Flag-tagged biotin ligase (BirA). After transfection of this vector, cells with stable genomic integration of cDNA-BirA constructs are selected. Following dox and biotin administration lead to selective

biotinylation of proteins in close proximity to the candidate. These potential binding partners are then identified by mass spectrometry analysis (LC-MS/MS).

For DSG2, I generated plasmids with C-terminal tagging of BirA/Flag to the human DSG2 protein (DSG2-C). N-terminal tagged DSG2 was not investigated, since the N-terminal end is located outside the cell membrane and therefore not informative regarding intracellular binding partners [134]. To identify DSG2-specific binding partners and to exclude binding partners for DSG1 from further analysis, I additionally generated plasmids expressing C-terminal tagged DSG1 (DSG1-C). Expression of the empty, BirA/Flag expressing vectors was used as control (BirA-N - unspecific labeling of all proteins). To test whether the constructs work properly, I performed western blot analysis after their transient transfection and dox treatment of Hek293T cells (figure 17B). As expected, a Flag-antibody detected BirA without fusion partner at around 35 kDa. Detection of untagged or BirA-tagged DSG2 revealed a moderate but clear expression at 120 kDa (endogenous DSG2) and 155 kDa (BirA-tagged DSG2). Since endogenous DSG1 was not detectable in Hek293T cells, overexpression of untagged DSG1 served as positive control (pT_DSG1 vector). Like for DSG2, DSG1 was detected with a 35 kDa shift compared to the native DSG1 control.

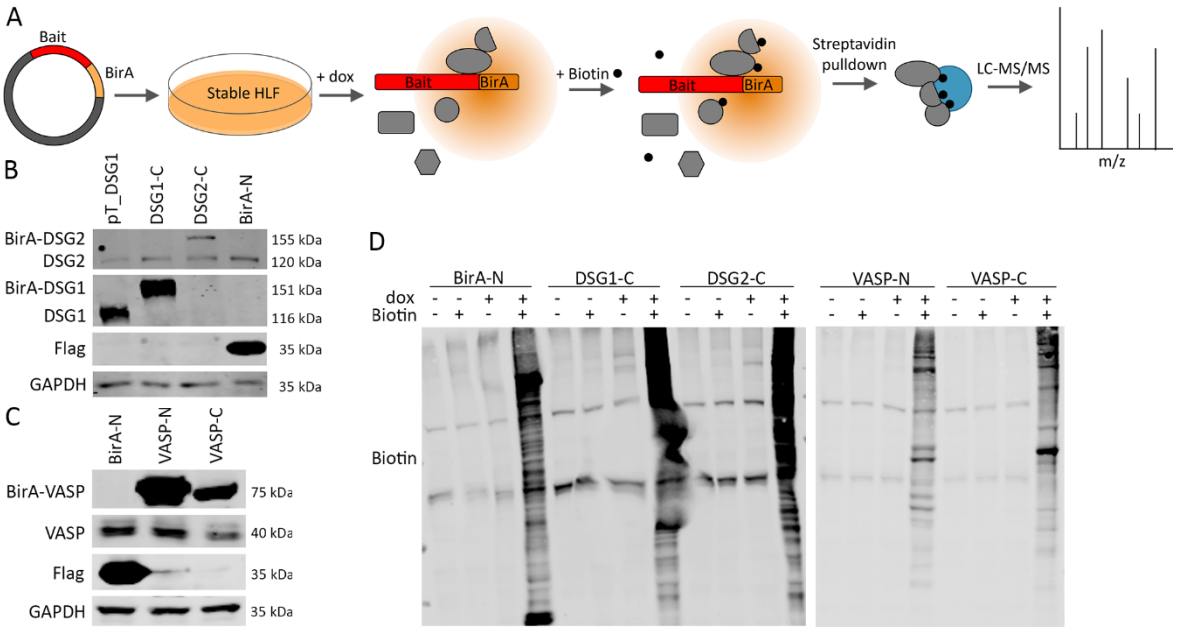

Figure 17: Bio-ID assay workflow and verification of experimental setup. (A) Schematic overview of the Bio-ID workflow for the identification of potential interacting targets of a bait protein by LC-MS/MS. Flag-tagged BirA is N- or C-terminally fused to bait proteins in a dox inducible vector system. **(B, C, D)** Functionality of the constructs is verified by western immunoblot after transient transfection of Hek293T cells and dox administration. **(B)** Expression of C-terminally tagged DSG1 (DSG1-C) and DSG2 (DSG2-C) is analyzed by western blot and compared to empty control vector (BirA-N) or untagged DSG1 overexpression by the pT_DSG1 vector. **(C)** Expression of N- and C-terminally tagged VASP is analyzed by western blot and compared to the empty BirA-N control vector. **(D)** HLF cells are stably infected with the different dox-inducible BirA expression vectors. Functionality of the cell lines is investigated by analysis of the biotin pattern after dox induction and biotin treatment.

For VASP, I generated VASP constructs with N- (VASP-N) and C- (VASP-C) terminal fusion of BirA, as VASP fully localizes in the cytoplasm (figure 17C). Again, cells expressing the empty BirA/Flag vector served as control and tagged VASP (75 kDa) could be demonstrated next to endogenous VASP (40 kDa). Next, I generated stable inducible Bait-BirA expressing HLF cell lines after transfection of the different constructs. The validity of the vectors was again tested by western blot (figure 17D). Therefor I analyzed the overall biotinylation pattern after administration of dox and biotin. Only in case of dox/biotin co-treatment 'laddering' of proteins was observed, which illustrated the biotinylation of many proteins (unspecific in case of BirA alone and specific in case of the DSG2/DSG1- and VASP-BirA isoforms).
After establishing the HCC cell lines with stable genomic integration of the constructs and inducible overexpression of the BirA fusion proteins, the relevant experiments were initiated (figure 18/20).

DSG1/DSG2

For the preparation of MS samples that would allow the identification of DSG binding partners, I seeded the BirA-DSG2-C, BirA-DSG1-C and empty vector BirA-N cell lines in quadruplicates, treated the cells with dox and biotin, and performed streptavidin pulldown assay for the enrichment of biotinylated proteins. Subsequently, samples were separated on PAA gels, gel pieces were cut out and subjected to LC-MS/MS analysis (figure 18A). Raw data were processed by the software Max Quant and led to the identification of 1,907 protein groups (one protein group contains all the proteins and protein isoforms, which can be explained by a given set of identified peptides). For further candidate selection, I continued with data analysis using the software Perseus (figure 18B). In a first step I excluded all potential contaminants, 'reverse' hits and hits which were 'only identified by site' and therefore not fulfill the quality criteria. Next, potential candidates must be detectable in three or four samples in at least one biological group (BirA-N, DSG2-C or DSG1-C). As proteins, which were not detected in every sample were considered to be a zero, I utilized a Perseus tool, which replaces missing values by random numbers based on normal distribution (imputation). Subsequently, a two-sample t-test comparing either DSG2-C or DSG1-C with the control was applied. Results for DSG1-C/BirA-N and DSG2-C/BirA-N are visualized in figure 18C+D. Next, I selected all potential candidates which were significantly ($P \leq 0.05$) upregulated ($\log_2$ fc > 1) in samples with BirA-DSG1 or BirA-DSG2 expressing cells compared to controls. This resulted in 171 hits for DSG1 and 179 for DSG2. After excluding all hits which were equally detected in DSG1 and DSG2, I narrowed down the number of potential DSG2 binding partners to 44 or to 36 in case of DSG1 (figure 18B+E, supplement table 2+3).

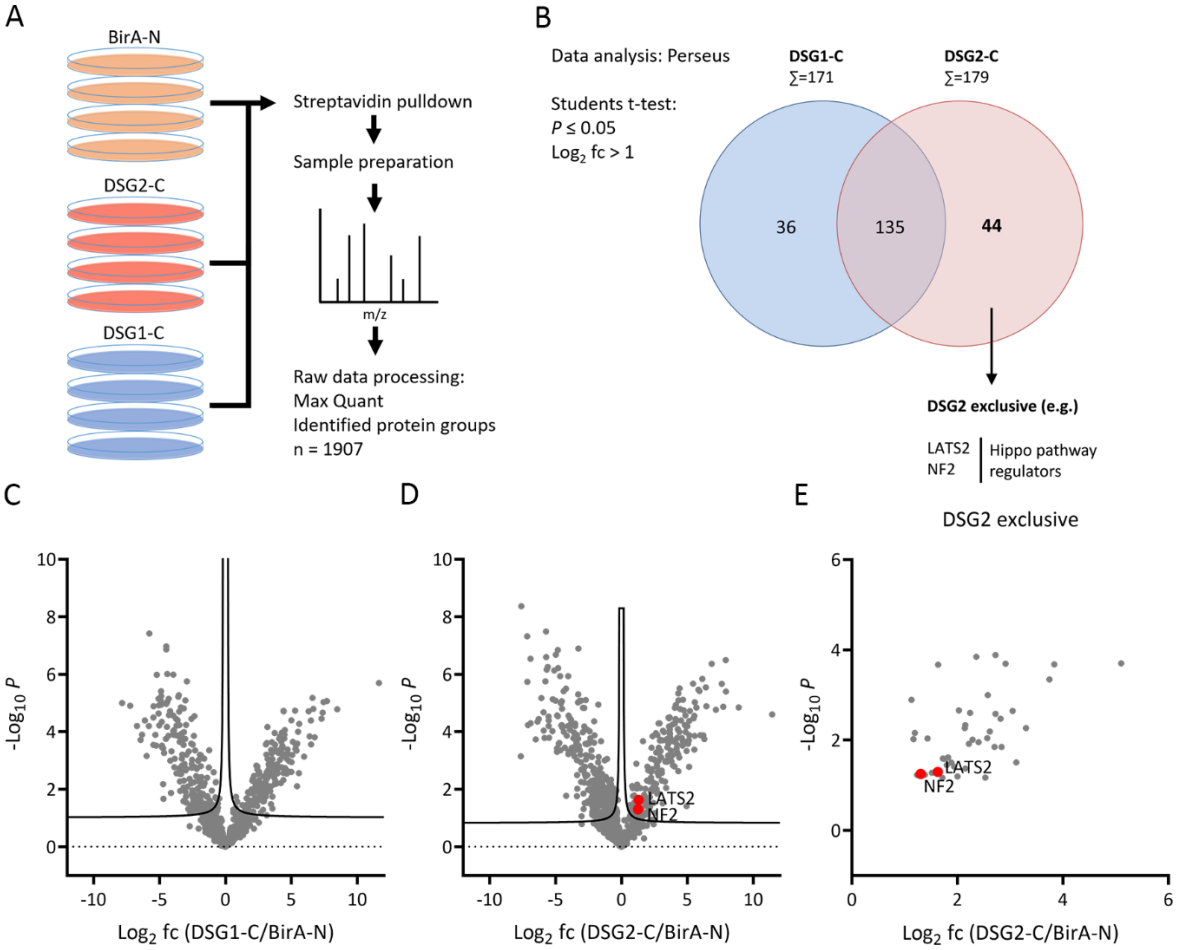

Figure 18: Proteomic analysis for the identification of DSG1 and DSG2 interaction partners. (A) Proteomics workflow for mass spectrometry measurement of C-terminally BirA-tagged DSG1 (DSG1-C) and DSG2 (DSG2-C) compared to controls (BirA-N). All cell lines are measured in biological independent quadruplicates. **(B)** Identified proteins (protein groups) are filtered for valid hits. Students t-test is performed for DSG1-C and DSG2-C respectively compared to the control. Significantly ($P \leq 0.05$) upregulated (Log_2 fc > 1) hits are overlapped and DSG2 exclusive hits (n = 44) are screened for potential candidates. Volcano plots illustrating all proteins detected by mass spectrometry for DSG1-C **(C)** and DSG2-C **(D)**. All hits above the curve are indicated as significant. **(E)** Volcano plot of all significantly upregulated DSG2 candidates. **(C, D, E)** The log_2 transformed fold-change (fc) of bait/BirA-N are plotted against the -log_{10} transformed *P*-values. Selected candidates used for subsequent analyses are labeled and marked with a red dot.

Importantly many of the factors identified for DSG1 and DSG2 have already been described as interaction partners in the literature. These include, among others, the desmosomal protein DSC2 [135], and the desmosomal adapter proteins plakoglobin (JUP) [136] and plakophilin-2/3 (PKP-2/3) [137][138]. This illustrated that the chosen approach worked and could be used for the identification of novel DSG interaction partners. However, there were also other so far not described binding partners for DSG1 and DSG2 on the list. For example for DSG1 the epidermal growth factor receptor kinase substrate 8 (EPS8) could be identified, which is a signaling adapter that regulates actin cytoskeleton architecture and dynamics [139] and promotes migration and invasion in breast cancer [140] and glioblastoma [141]. Another novel target was sorting nexin-6

(SNX6), which is involved in intracellular trafficking of membrane receptors and promotes breast cancer repression, but is also described to contribute to EMT and metastasis in pancreatic cancer [142] [143]. In case of DSG2, one interesting potential interaction partner was the neuroblast differentiation-associated protein AHNAK, which is a scaffolding protein that interacts with junctional associated structures like ZO-1 or F-actin and mediates cell architecture and calcium homeostasis. Among other it can be regulated by cell-cell contact [144]. Further AHNAK is described to have tumor suppressive functions in breast or ovarian cancer by affecting multiple signaling pathways like the Wnt/β-catenin pathway [145] [146]. Despite AHNAK, also roundabout homolog 1 (ROBO1) was detected as interesting potential binding partner since it is described to promote liver fibrosis and angiogenesis in HCC [147] [148].
However, as the initial goal of this experiment was the identification of DSG2 binding partners that could control the Hippo/YAP signaling axis, I systematically screened the list of potential DSG2 interaction partners for Hippo pathway effectors. Doing so, I identified the known Hippo pathway regulators NF2 and LATS2. Abundance and significance of the discovered Hippo constituents are illustrated among all detected (figure 18D) and the DSG2 exclusive (figure 18E) hits. Interestingly, the transcriptional effector YAP was not detectable in any data set. This suggests that DSG2 indirectly controls YAP activity via the physical binding of NF2 and LATS2. Indeed, for both factors a direct impact on YAP activity has been described in different cell models [149] [150].

To confirm the predicted DSG2-NF2/LAST2 interactions, Co-IP and PLA experiments were initiated. For the Co-IP analysis, I transiently overexpressed Flag-tagged DSG2 in HLF cells and used Flag-antibody to pull-down DSG2 and its interaction partners. The protein fraction was analyzed by Western blot and illustrated that LATS2 and NF2 indeed physically interacted with DSG2 (figure 19A). As YAP was not identified as a potential DSG2 binding partner, I also confirmed the absence of any interaction between both proteins by independent and 'inverse' Co-IP experiments (figure 19B). To further confirm the results, I additionally performed PLA experiments, which illustrate the close spatial localization of two proteins via specific antibodies *in vitro* (figure 19C). As negative controls, I applied DSG2, YAP, LATS2 and NF2 antibodies alone, illustrating no or weak positivity. As already indicated by the Co-IP results, co-incubation of DSG2 and YAP didn't result in any obvious signal. In contrast, application of DSG2- and LATS2-specific antibodies led to a moderate and predominantly nuclear signal for this interaction. For NF2, a clear cytoplasmic but also nuclear interaction with DSG2 was observed. Interestingly, a nuclear localization of DSG2 was not described so far. No obvious membranous positivity for the DSG2/LATS2 and DSG2/NF2 interaction was detectable.

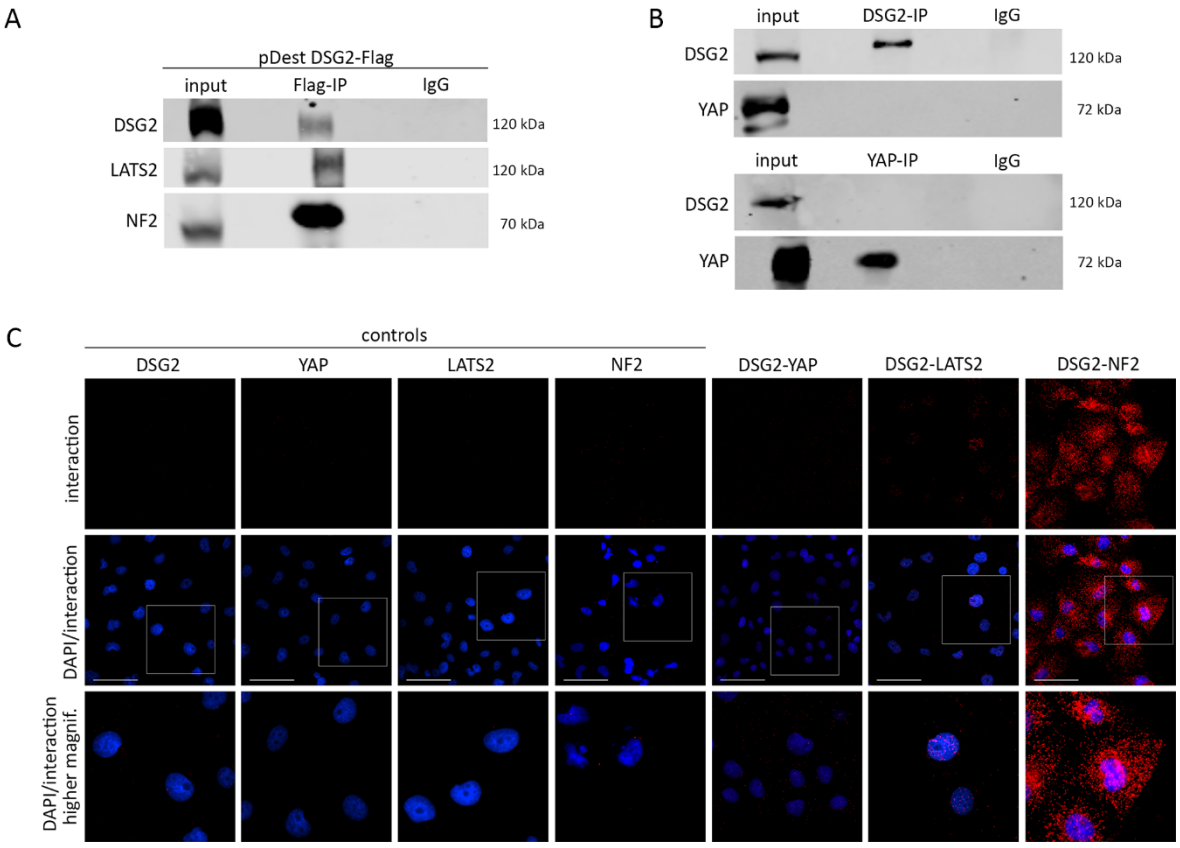

Figure 19: Interaction analysis using co-immunoprecipitation and proximity ligation assay. (A) Flag-tagged DSG2 is transiently overexpressed in HLF cells (pDest_DSG2-Flag) and immunoprecipitated using Flag antibody. Potential interaction partners are investigated by Western immunoblot analysis. **(B)** Western blot analysis of immunoprecipitated DSG2 and YAP from HLF cell lysates. **(A, B)** Total protein lysate (input) and unbound antibody (IgG) serve as controls. **(C)** Proximity ligation assay. The upper panel indicates interaction intensity of the targets. Single antibody treatment is used as control. Scale bar: 200 µm.

VASP

For studying VASP interactome I seeded quadruplicates of VASP-C, VASP-N and the control and performed the approach as described for DSG2 (figure 20A). Processing of the raw data disclosed that in total 2110 protein groups were identified. I filtered and analyzed the data as described before. Next, I applied the two-sample t-test, comparing either VASP-N or VASP-C with the control and selected all significant upregulated hits. Overlapping of the interactome revealed that 256 proteins were detected in both groups, while VASP-N had 307 and VASP-C had 50 exclusive hits. In total 613 interaction partners could be detected (figure 20B). The 150 most abundant hits are listed in supplement table 4. Importantly many of the factors identified for VASP have already been described as interaction partners in the literature, for example the actin filament binding vinculin or the tight junction proteins ZO-1/2 [151] [152]. This illustrated that the approach worked and could be used for the identification of novel VASP interaction partners. For example, signal transducer and activator of transcript 2 (STAT2) could be identified, which plays an important role in the modulation of immune responses and cancer [153].

However, as the initial goal of this experiment was the identification of VASP binding partners that could control the Hippo/YAP signaling axis, I systematically screened the list for YAP effectors. Surprisingly YAP was among them, it could be detected as significantly upregulated in VASP-N (figure 20C) as well as VASP-C (figure 20D) samples, suggesting that VASP and YAP are direct interaction partners.

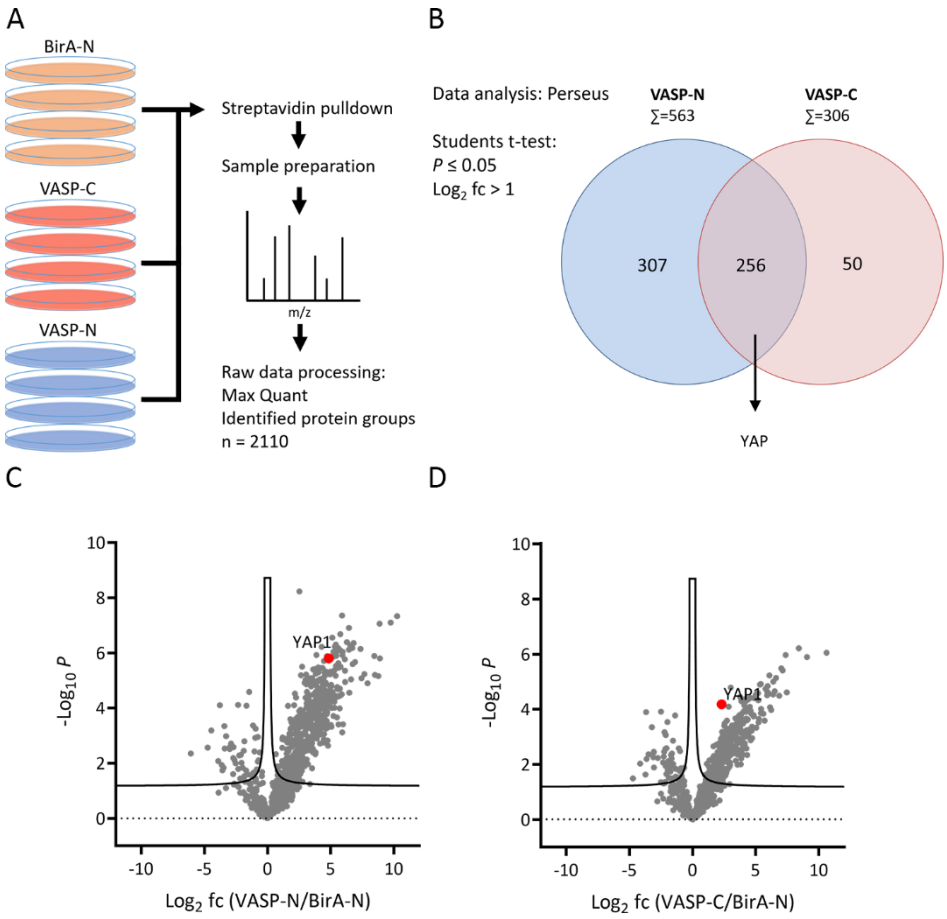

Figure 20: Proteomic analysis for the identification of VASP interaction partners. (A) Proteomics workflow for mass spectrometry measurement of C-terminally BirA-tagged VASP (VASP-C) and N-terminally BirA-tagged VASP (VASP-N) compared to controls (BirA-N). All cell lines were measured in biological independent quadruplicates. **(B)** Identified proteins (protein groups) are filtered for valid hits. Students t-test is performed for VASP-C and VASP-N respectively compared to the control. Significantly ($P \leq 0.05$) upregulated (Log_2 fc > 1) hits are overlapped and screened for potential candidates. Volcano plots illustrating all proteins detected by mass spectrometry for VASP-N **(C)** and VASP-C **(D)**. The log_2 transformed fold-changes (fc) are plotted against the $-log_{10}$ transformed *P*-values. Selected candidates used for subsequent analyses are labeled and marked with a red dot. All hits above the curve are indicated as significant.

The MS results did not indicate that VASP controls the Hippo pathway via the interaction with Hippo pathway constituents. Instead, a direct interaction with YAP was predicted. I confirmed this finding by Co-IP experiments with endogenous VASP and YAP (figure 21A). Detection of VASP revealed a signal not only in the VASP-IP but also the YAP-IP. However, YAP was only detectable in the YAP-IP

and not in the VASP-IP. Thus, the interaction between both proteins were only confirmed for one Co-IP condition. Since the findings were inconsistent, I used PLA to further validate the Bio-ID and Co-IP results (figure 21B). No background signals were detectable for the VASP and YAP antibodies alone (negative control). However, co-incubation with both antibodies resulted in a very strong, mainly cytoplasmic signal within spitting distance to the nucleus, proving a close spatial proximity and probably VASP-YAP interaction.

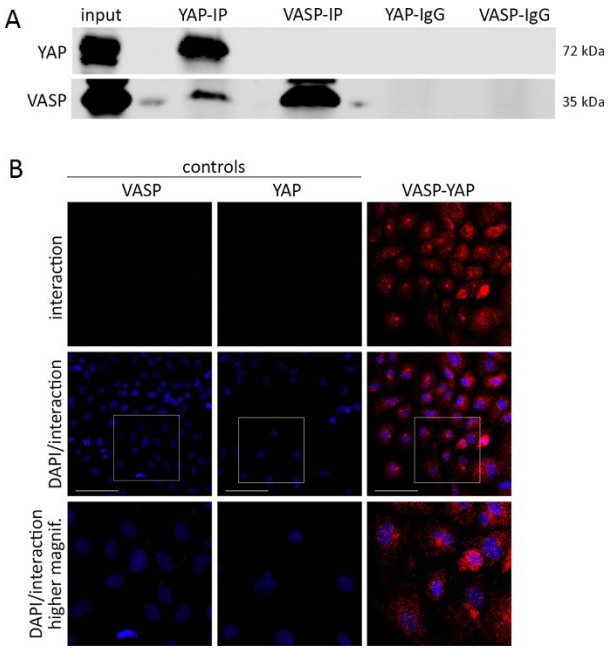

Figure 21: Interaction analysis using co-immunoprecipitation and proximity ligation assay. (A) Co-immunoprecipitated VASP and YAP from HLF cell lysates are investigated by western blot. Total protein lysate (input) and unbound antibody (IgG) serve as controls. **(B)** Proximity ligation assay. The upper panel indicates interaction intensity of the targets. Single antibody treatment is used as control. Scale bar: 200 µm.

All together the results of the Co-IP and PLA analyses verified the predicted interactions from the BioID-assay. DSG2 directly interacts with the Hippo regulators NF2 and LATS2 but not with YAP. VASP directly binds YAP. This confirms the hypothesize that DSG2 and VASP affect YAP activity via distinct mechanism.

4.11 DSG2 and VASP show no oncogenic potential *in vivo*

Exploration of the TCGA and LCI HCC expression data cohorts indicated a worse clinical outcome for patients with high DSG2 or VASP expression (figure 4+5). In addition, functional analyses in liver cancer cells revealed a moderate to strong impact on cell viability, proliferation, migration and invasion, suggesting that high levels of DSG2 and VASP support pro-tumorigenic properties of cells

(figure 11+12). However, it is so far unknown if DSG2 or VASP overexpression also facilitates tumor initiating properties, which would qualify these factors as oncogenes. This hypothesis is supported by the fact that DSG2 and VASP affect the tumor suppressive Hippo pathway and its downstream effector YAP (figure 13+14).

To test if DSG2 or VASP may act as oncogene in case of their dysregulation, I used an *in vivo* approach which allows the rapid and direct genetic manipulation of liver hepatocytes after injection of expression vectors in the lateral tail vein of mice (hydrodynamic gene delivery) [110]. For this, murine DSG2 and VASP orthologues were cloned in a pT3 vector (pT3_DSG2, pT3_VASP). The efficiency of the generated vectors was tested by qPCR after transient transfection of murine Hepa1-6 cells (figure 22A). qPCR results revealed a strong expression of murine DSG2 and murine VASP in pT3_DSG2/VASP transfected cells compared to cells transfected with the empty pT3 plasmid. Since the plasmids were functional, they were injected in the tail vein of mice, together with another vector coding for sleeping beauty transposase. To check if the injection technically worked *in vivo*, livers were isolated 1 week after injection and tissue sections were stained for GFP (the pT3 vector contains a GFP expression cassette) by immunohistochemistry. Results reveal that about 5-10% of the hepatocytes were successfully transfected (figure 22B).

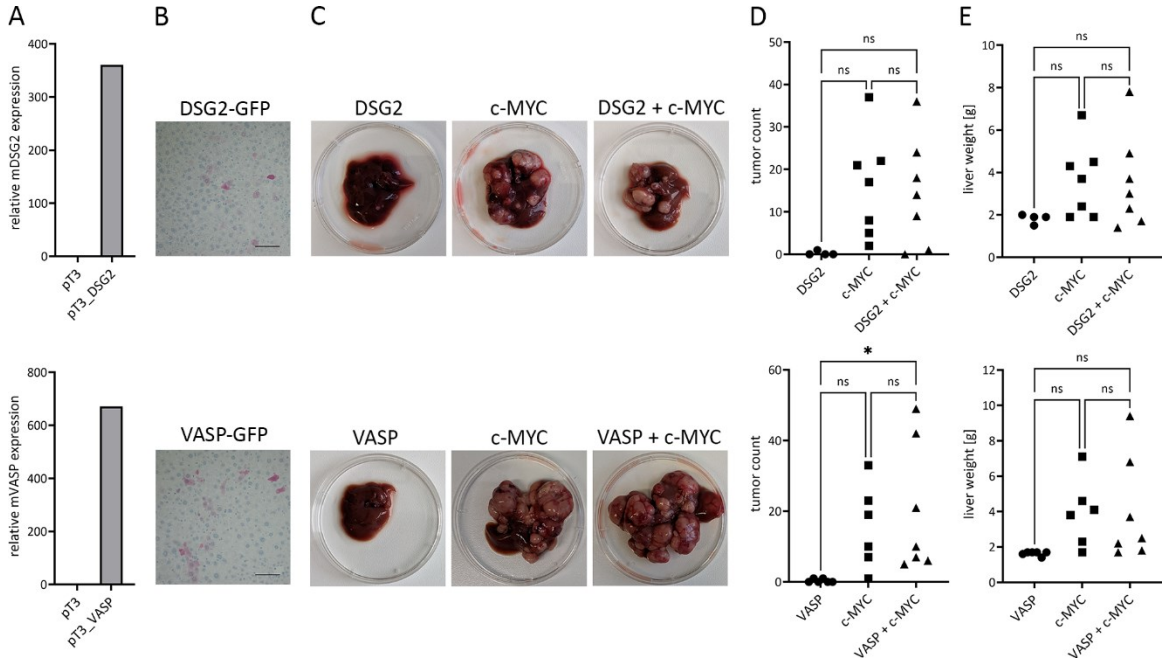

Figure 22: Analysis of oncogenic potential of DSG2 and VASP after hepatocyte-specific overexpression in mice. (A) DSG2 and VASP are cloned in pT3 vectors and their expression is checked using qPCR analysis. **(B, C, D, E)** DSG2, VASP and c-MYC expressing plasmids are delivered to FVB/N mice using hydrodynamic tail vein injection. **(B)** Livers are harvested one week post-injection and tissue sections are stained against GFP. **(C, D, E)** Livers are harvested five weeks post-injection and liver weight and tumor number is determined. Pictures of exemplary livers are shown. **(C, D)** Every dot represents one mouse. The ordinary one-way ANOVA is used for statistical analysis. ns - not significant. * $P \leq 0.05$.

To test the direct oncogenic impact of DSG2 and VASP, both vectors were separately injected, and mice were monitored. However, no macroscopic or microscopic tumor formation was detected after vector injection and subsequent isolation of liver tissues for up to five weeks. Thus, both proteins are not potent oncogenes; however, it was possible that DSG2 and VASP could support tumor formation in conjunction with other known liver oncogenes such as c-MYC [110]. Therefore, I co-injected DSG2 and VASP expressing vectors with a vector that allows the expression of c-MYC (c-MYC expression alone served as control). Five weeks after injection I isolated the livers, measured their organ weight and macroscopically quantified tumor number formation (figure 22C-E). As described in the literature, single expression of c-MYC induced tumor formation, co-injection of c-MYC and DSG2 or VASP did not significantly increased the number of tumor nodules or liver weight. These findings demonstrate that DSG2 and VASP do not act as liver oncogenes in the chosen experimental setup.

5 Discussion

Dysregulation of junctional structures is associated with the development of several diseases, including HCC, which is also associated with disturbed Hippo/YAP signaling. However, it was unknown if specific molecular mechanisms exist, which connect the aberrant expression of junctional constituents with altered YAP activity. In this study, three junctional and junction-associated proteins were identified to be dysregulated in human HCCs, with two of them affecting YAP activity. I systematically screened liver cancer patient expression data resulting in the identification of aberrantly expressed junctional proteins (DSG1, DSG2, VASP). Dysregulation at the transcript level of these factors was associated with poor clinical outcome and correlated with YAP activity. Investigation of additional patient tissues und patient expression samples confirmed the inverse regulation of DSG1 and DSG2 in HCC, with DSG2 being up- and DSG1 being down-regulated, while VASP was identified to be elevated in HCC tissues. *In vitro* analyses revealed that DSG2 and VASP supported HCC cell viability and affected YAP activity probably *via* distinct mechanisms: while VASP directly bound YAP, DSG2 interacted with the Hippo pathway constituents NF2 and LATS2 and thereby could affect YAP activity. Additional *in vivo* experiments disclosed that DSG2 and VASP were not potent oncogenes, illustrating that their dysregulation was not causative for tumor initiation. Interestingly, DSG1 did not show any effects on cell functionality or YAP activity and was therefore excluded as potential HCC driver and Hippo/YAP effector. Thus, the study provided novel insight into the distinct roles of junctional and junction-associated proteins on HCC cell functionality dependent on Hippo/YAP signaling.

5.1 A transcript-based screening approach is an effective method to identify structures with impact on specific pathways

Since the goal of this project was to disclose molecular connections linking aberrantly expressed junctional proteins in HCC with Hippo/YAP pathway activity, I initially identified potential candidates that were dysregulated in HCC patient cohorts and that correlated with patient survival and YAP activity. For this I established a straightforward screening approach, which systematically considered these selection criteria. To narrow down the number of potential candidates and to provide stronger evidence that they might be of relevance in human hepatocarcinogenesis, I analyzed two different HCC patient cohorts and selected those candidates that were identified in both cohorts [112][111]. The selection process resulted in the identification of five candidates

which were aberrantly expressed in HCC, associated with worse patient survival and correlated with YAP induced gene signature [61]. Three of them - downregulated DSG1, upregulated DSG2 and upregulated VASP - were selected for further investigations. Analysis of two additional patient cohorts by immunofluorescence and real-time PCR, consisting of tumor and non-tumorous samples, confirmed the general tendency of candidate expression, albeit not reaching the level of significance. These results could be explained by the low number of samples in both cohorts, as well as heterogenous expression of the candidate genes in cancer patients. Especially the latter aspect led to the assumption that only a subgroup of patients exhibited the expected phenotype regarding DSG1 reduction and DSG2/VASP induction. This was in accordance with the publication of Weiler et al., who demonstrated that the increased expression of YAP-dependent signature genes defined a subgroup of HCC patients (about 33%) with poor clinical outcome [61]. As VASP and DSG2 positively controlled YAP activity in HCC cells, it was tempting to speculate that the induction of YAP activity in 1/3 of cancer patients was in part due to transcriptional dysregulation of VASP and/or DSG2.

Additional functional analyses in my study illustrated the impact of DSG2 and VASP on YAP activity. For VASP, a study from Xiang et al. confirmed these observations, as they described that VASP promoted gastrointestinal cancer metastasis by activating YAP *via* the β1-integrin-FAK axis and by promoting YAP dephosphorylation to enhance its stability [154]. Liu et al. showed that VASP was overexpressed in HCC tissues and was associated with worse overall survival [155]**.** The elevated expression of DSG2 in HCC and its impact on prognosis of HCC patients was confirmed by Han et al. [156], however, a connection with Hippo/YAP activity has not been described yet. For DSG1 no association with HCC was described so far. Thus, the findings of this thesis were not only in accordance with published data from other groups but also added new information regarding the dysregulation of junctional factors in HCC and the mechanistic connection between cell junctions and YAP activity. Interestingly, unpublished data from my colleague Yingyue Tang revealed that CTNNA1 (synonym: α-catenin), which was also identified by the described screening workflow, was elevated in HCC tissues, and supported HCC cell functionality. Although a direct connection between α-catenin and YAP has been described in the literature for other tumor cell types [157], no direct regulatory mechanism was detectable for HCC. Instead, YAP controlled the expression of the centrosomal protein 55 (CEP55), which physically bound α-catenin (unpublished data). Together with my findings, these results illustrated that – although the underlying mechanisms might vary – the tissue-based screening approach was valid and could identify meaningful connections between factors.

Considering these findings, I could show that majority of the identified candidates indeed were dysregulated in HCC and associated with YAP activity, what affirmed the relevance of the applied

screening strategy. Since I started the analysis by defining a list of junctional and junction associated structures, an advantage of this procedure was the possibility to apply the same workflow on different aims by adapting the "input information" (e.g., by including a list of kinases to find out which affect YAP activity). However, this approach also comprised a disadvantage, namely only known and described structures or gene lists could be used. Further, structures which were regulated not *via* expression changes but intracellular localization (e.g., CTNNB1) or phosphorylation (e.g., YAP) should not be integrated [31][71]. Lastly, the analysis of tissue sample cohorts was difficult due to the presence of non-tumorous cell type (e.g., immune cells), which may conceal transcript information coming from tumor cells. This disadvantage was considered in my study as IF and partly IHC analyses confirmed that DSG1/2 and VASP were expressed by tumor cells in HCC tissues.

5.2 The unbiased BioID assay as method to identify interaction partners of DSG2 and VASP

Analysis of protein-protein interactions is essential for understanding the function as well as underling mechanism of a protein and is therefore one of the major objectives in cell biology. Various methods have been developed so far, each with advantages and limitations. One commonly used method is Co-IP analysis, where the interactome of the target protein is enriched by using an appropriate antibody. During the following Western immunoblot analysis, specific antibodies are applied to detect the binding partner of the precipitated factor. A disadvantage of this approach is that next to direct interaction partners also protein associations in a complex (indirect binding) can be isolated [158]. In addition, the scientist must already have candidates in his/her mind as protein-specific antibodies must be used for Western immunoblotting. Another method is the highly sensitive *in situ* PLA, which depends on the recognition of target molecules in proximity (<40 nm) by applying specific antibodies that are linked to pairs of affinity probes. Therefore, also proteins localized in short distance can be detected as interaction partners. This on the one hand enables the immediate visualization of direct interactions partners but on the other also of structures which don't interact. This method can be used to detect protein interactions directly in cells or tissues and thus gives additional information about the localization of the interaction [159]. As described for Co-IP experiments, a disadvantage of this method is, that only known proteins can be targeted by the usage of specific antibodies.

In contrast, the unbiased BioID assay is a high throughput screening strategy, which allows the proximity-dependent labeling of proteins in living cells and their subsequent identification by

LC-MS/MS in an antibody independent manner. Thus, a huge amount of data can be generated with just one experiment, which helps to create several new hypotheses regarding potential interaction partners of the 'bait'. Since the labeling takes place in living cells, adjacent proteins are tagged in a physiological cellular setting over a period of time, which leads to the identification of binding partners in a 'normal' cellular environment [160]. A disadvantage is that the expression of an exogenous fusion protein is required, what needs an intricately cloning procedure. Since the BirA tag is relatively big (35 kDa), it could lead to conformation changes and mislocalization of the bait and may interfere with protein-protein interactions and impair normal targeting or function [160]. Therefore, thoroughly validation is necessary. In case of my generated DSG1-, DSG2- and VASP-BirA fusion constructs I reviewed the expression and functionality of the constructs by Western immunoblot and the subcellular localization by IF staining before I started the actual experiments. However, with a labeling radius of approximately 10 - 15 nm this method is even more specific than PLA but still allows the labeling of indirect interaction partners [161]. In addition, since all proteins are denatured and solubilized, and thus protein complexes are disaggregated, the number of false positive 'hits' is drastically reduced. Especially in case of membrane or cytoskeletal proteins, which tend to aggregation and filament formation, this is of advantage, making it to an optimal method to study the interactome of my candidates DSG2 and VASP [160][162]. In accordance, this method had already been used to study the interactome of diverse junction-associated proteins such as N-cadherin, E-cadherin, or the serine/threonine protein kinase PAK4 [163][164][165]. Interestingly, one specific study revealed that fusion of the biotin ligase to either the N- or C-terminal end of the bait resulted in the identification of common but also exclusive proteins [166]. On one hand this result highlighted the specificity of this method, but also supported my results for VASP, where differences between N-terminal and C-terminal tagged VASP were detected. This variability after N- and C-terminal tagging, regarding the identified binding partners, could be due to conformational changes of the bait caused by the BirA ligase. Another explanation was that the ends of VASP could be involved in different functional complexes. However, after performing the LC-MS/MS measurement and subsequent data analysis, I screened the data for known interaction partners of DSGs and VASP as I expected to identify some known binding partners (positive control). Indeed, I identified several proteins like DSC2, PKP2/3, ZO1/2 or Vinculin, which supported the validity of the chosen approach and its usefulness for identifying novel DSG1/2 and VASP binding partners [135][138][152][151]. As the shortlisted binding partners could also be caused by spatial proximity and did not necessarily imply a direct physical interaction with the bait, I decided to confirm my results by Co-IP assays. In addition, PLA assays provided further information about the subcellular localization of the potential interaction.

Since I was especially interested to identify mechanistic links to YAP, I screened the detected proteins for known constituents of the Hippo pathway. Interestingly, I detected YAP itself among the hits for VASP in the candidate list for N-terminal tagged VASP and the C-terminal tagged VASP. *Vice versa*, VASP could be detected after performing interactome studies for YAP using the BioID approach (unpublished data). In accordance with the results of my study, DSG2 was not detected as YAP interacting protein (unpublished data). Instead, my data showed that DSG2 controlled YAP activity *via* the interaction with upstream regulators of YAP (illustrated for LATS2 and NF2). This strongly suggested that the mode of action of YAP regulation varies between DSG2 and VASP. Results of subsequent Co-IP and PLA analyses verified the predicted DSG2-LATS2, DSG2-NF2 and VASP-YAP interactions from the BioID approach, thereby proving the specificity and sensitivity of the method.

In summary, published and unpublished results as well as my thesis demonstrated that not all changes in junctional structures control YAP activity in HCC cells (e.g., α-catenin, DSG1). In contrast, the dysregulation of some junctional factors affected YAP activity probably *via* distinct molecular mechanisms (e.g., DSG2 and VASP).

5.3 Expression of DSG family members under physiological and pathological conditions

Desmogleins represent a family of non-classical cadherins, also referred to as desmosomal cadherins, consisting of the proteins DSG1, DSG2, DSG3 and DSG4, which span the plasma membrane of epithelial cells. Accordingly, all family members consist of extracellular-, transmembrane- and cytoplasmic domains [125]. Next to desmocollins, desmogleins are core components of cell-connecting desmosomes. Outside of the cell membrane, desmogleins/desmocollins form homophilic or heterophilic interactions with neighboring cells and contribute to cellular adhesion and communication. Inside the cell membrane, desmogleins/desmocollins connect cytoskeletal elements to the plasma membrane [11]. Although their function is mainly of mechanical nature, they also affect and modulate distinct cellular signaling cascades involved in differentiation, homeostasis, and carcinogenesis [13].

A disorder related to desmoglein dysregulation is *pemphigus vulgaris*, a blistering autoimmune disease of the skin. Here, antibodies are formed against DSG1 and DSG3, which leads to pathological loss of cell-cell adhesion in the epidermis. As consequence, keratinocytes bind each other less efficient, become separated, and the epidermis detaches from the underlying dermis [167]. In addition, desmogleins have also been found to be ‘imbalanced’ in many types of cancer, where

their aberrant expression contributes to metastasis and invasion [11]. However, different studies revealed an ambivalent role of desmogleins, either as oncogene or tumor suppressor. For example, DSG2 was shown to be downregulated in colon and prostate cancer, but upregulated in cervical cancer [168][169][170]. DSG3 was overexpressed in head neck cancer where it associated with clinicopathological features of the tumor, while membranous negativity of DSG1 was shown to be favorable for anal carcinoma patients [171][172]. Therefore, it was of great interest to disclose the distinct roles of DSG1 and DSG2 in HCC, as their dysregulation – but not of DSG3 – was associated with poor clinical outcome in HCC patients.

In this work I was able to show in different patient cohorts that DSG1 expression was diminished in HCC, while DSG2 was upregulated compared to non-tumorous liver tissues. Interestingly, the expression of these two desmogleins was negatively correlated. Since the genes of DSG1 and DSG2 are localized in relative close proximity (161 kb apart) on the same chromosomal arm 18q12.1 together with the other members of the DSG family, it is likely that specific mechanisms regulate their expression [173]. As no certain molecular mechanism could be identified in this study that could explain DSG1 reduction and simultaneous DSG2 induction (promoter methylation and copy number alterations were excluded), the most likely explanation for the opposite regulation of DSG1/2 was the differential activation by transcriptional regulators. Unfortunately, respective studies that could clarify the underlying mechanisms were not performed in my thesis due to time limitations. Interestingly, the expression of DSG family members seems to be different in other tumor types. For example, a previous study demonstrated that DSG1, DSG2 and DSG3 expression was reduced in most lung cancer cell lines. Demethylation treatment led to partial reexpression of DSG2 and DSG3, indicating that promoter methylation was partly responsible for silencing of the genes in lung cancer cells [174]. In case of DSG1 demethylation of the genome did not cause a reexpression.

In the epidermis, the expression of DSGs varies through the different layers of keratinocytes. While DSG2 is predominantly expressed in the basal cell layer of the epidermis, DSG1 is mainly detectable in the upper layers, which is characterized by keratinocyte differentiation [175]. *Vice versa* many basal DSG2 positive keratinocytes undergo mitosis to replace differentiating cells in the suprabasal layers. In accordance with this observation it was shown that DSG2 is highly upregulated in epithelial-derived skin tumors, which were characterized by tumor cell proliferation [176]. Interestingly, the expression of the desmogleins in the epidermis correlates with the order in which the genes are arranged at the chromosomal locus, from centromeric to telomeric direction [177]. Together this data suggested that the common or mutual exclusive expression of desmogleins, which might exhibit antagonistic functions, is temporally and spatially controlled, and reflects the state of cellular differentiation [178].

In this work, Kaplan-Meier analysis revealed that HCC patients with low DSG1 expression had poorer prognosis compared with high DSG1 expression. In case of DSG2 the opposite effect was observed; patients with high DSG2 were characterized by a poor clinical outcome. The latter finding was consistent with results from Han et al., who showed that DSG2 expression was higher in HCC tissues than in noncancerous tissues and correlated with tumor aggressiveness [156]. However, aberrant DSG1 expression in HCC was not described so far. Functional analyses revealed that DSG2 positively affected HCC cell proliferation and viability, but also migration and invasion. Importantly, *in vivo* analyses excluded DSG2 as hepatic oncogene. In case of DSG1 no influence on tumor cell function could be observed.

In conclusion, the results of my study illustrated an inverse DSG1/2 dysregulation in HCC. Only DSG2 accumulation promoted tumor cell viability and migration, but DSG2 did not act as oncogene *in vivo*. As the contrary expression of DSG1 and DSG2 was also observed in healthy tissues (e.g., skin), it was likely that existing molecular mechanisms control their expression under physiological and pathological conditions. Additionally, the inverse expression of DSG1 and DSG2 may serve as biomarker that predicts clinical outcome of (liver) cancer patients.

5.4 Dysregulation of VASP in carcinogenesis and its impact on YAP activity

VASP is a member the Ena/VASP family, which is a class of actin binding proteins. Besides VASP the family consists of two more members in vertebrates, namely Mena and Ena/VASP-like protein. All members share a conserved structure consisting of three functional domains: The N-terminal Ena-VASP-homology-1 (EVH1) domain, the polyproline-rich (PRD) core region, and the Ena-VASP-homology-2 (EVH2) domain at the C-terminus. With the EVH1 domain the Ena/VASP family members can bind to several cytoskeletal proteins and mediate subcellular targeting. The central PRD allows binding to actin-monomer-binding profilin, thereby promoting actin assembly and further mediates interaction with SH3- or WW-domain containing signaling proteins. Lastly, the EVH2 domain mediates interaction with monomeric and filamentous actin and is responsible for its tetramerization [179].

VASP proteins are localized close to actin fibers, the leading edge of lamellipodia and filopodia of mobile cells. Further, VASP is involved in cytoskeletal rearrangement and links the cytoskeleton dynamics with the activity of signaling pathways (see below). Additionally, this protein plays an important role in cell migration, cell adhesion and cell cycle progression. Under disease condition VASP has been described as an oncogene and to promote cancer metastasis as well as invasion

[179]. For example, VASP was related to the development of breast cancer, since it was upregulated in breast cancer tissues and its overexpression correlated with tumor stage, metastasis, and early recurrence [180]. In lung adenocarcinoma the expression of VASP was equally increased, especially in tumors with advanced stages [181]. In addition, VASP was described to promote cell migration and invasion in other malignant tumors like gastric or colon cancer [182][154]. Mechanistically, VASP promoted in most cases actin-dependent processes. However, other studies indicated that also VASP-deficiency could promote actin fiber formation, suggesting that balanced levels of VASP are necessary for correct functionality [183].

In this work I was able to show in different patient cohorts that VASP was upregulated in HCC compared to noncancerous tissues. Kaplan-Meier analysis revealed that patients with high amounts of VASP had a poorer prognosis. Increased VASP expression statistically associated with advanced tumor stages and positively affected HCC cell viability, proliferation, migration, and invasion. Although, VASP clearly facilitated tumor-supporting properties, my *in vivo* experiments (overexpression alone and in combination with an oncogene) excluded this factor as cancer driving oncogene in HCC. Data from Liu et al. confirmed the observed upregulation of VASP in HCC and that this condition promoted HCC cell migration and invasion by affecting actin dynamics. As underlying mechanism, they suggested that hypoxia inducible factor 1α (HIF-1α) contributed to the upregulation of VASP, which interacted with CRKL. This VASP-CRKL complex led to the activation of different signaling pathways as illustrated for AKT and ERK. AKT/ERK phosphorylation promoted the formation of an EMT phenotype and expression of MMPs, what was associated with increased HCC migration and invasion [155]. Another study from Dang et al., equally suggested that VASP was involved in the regulation of HCC metastasis, as they detected elevated migration and invasion of tumor cells after VASP overexpression or diminished mobility after VASP inhibition. Their data indicated that overexpression of VASP and of PDK1 was promoted by the transcription factor HOXC10, which was induced by interleukin-1β signaling [184]. Thus, both studies confirmed that VASP was overexpressed in HCC and that this upregulation correlated with tumor progression and reduced prognosis, though they identified different mechanism behind the regulation.

My screening approach already indicated that VASP correlated with YAP activity in HCC tissues as VASP transcript levels correlated with the abundance of YAP target genes (called CIN4). One possible explanation for this connection could be that YAP was regulated by Rho-GTPases and F-actin dynamics as VASP modulates F-actin assembly [82]. However, at this stage I could not exclude the possibility of further molecular mechanisms of VASP-dependent YAP activity. Therefore, it was of great interest to further investigate how VASP contributes to hepatocarcinogenesis and weather this mechanism is YAP related. By using the BioID approach and subsequent confirmatory experiments, I was able to identify YAP as a direct binding partner of

VASP. PLA analysis further revealed that they strongly interacted in the cytoplasm in close spatial proximity to the nucleus (figure 23). A direct impact of VASP on YAP activity in HCC was not described so far. However, a previous study from Xiang et al. revealed that VASP promoted liver metastasis of gastrointestinal cancer by activating YAP signaling via the β1-integrin-FAK axis. Here, two mechanisms were identified. First, VASP promoted ECM-induced β1-integrin activation. Second, VASP enhanced YAP stability by promoting its RhoA-dependent dephosphorylation. Indeed, no direct interaction of VASP with YAP was described. However, this demonstrated that inhibition of VASP led to a reduction of total amount of YAP and hence a downregulation of the YAP target gene CTGF [154]. In contrast, my results revealed that total YAP was not affected after VASP inhibition. Instead, pYAP levels were elevated after VASP silencing, thereby pointing towards an inactivation and cytoplasmic translocation of YAP. Thus, the observed VASP overexpression represented a tumor supporting step, that decreased YAP phosphorylation and allowed its nuclear enrichment in HCC cells (figure 23). However, how VASP protected YAP from phosphorylation was not investigated in my thesis.

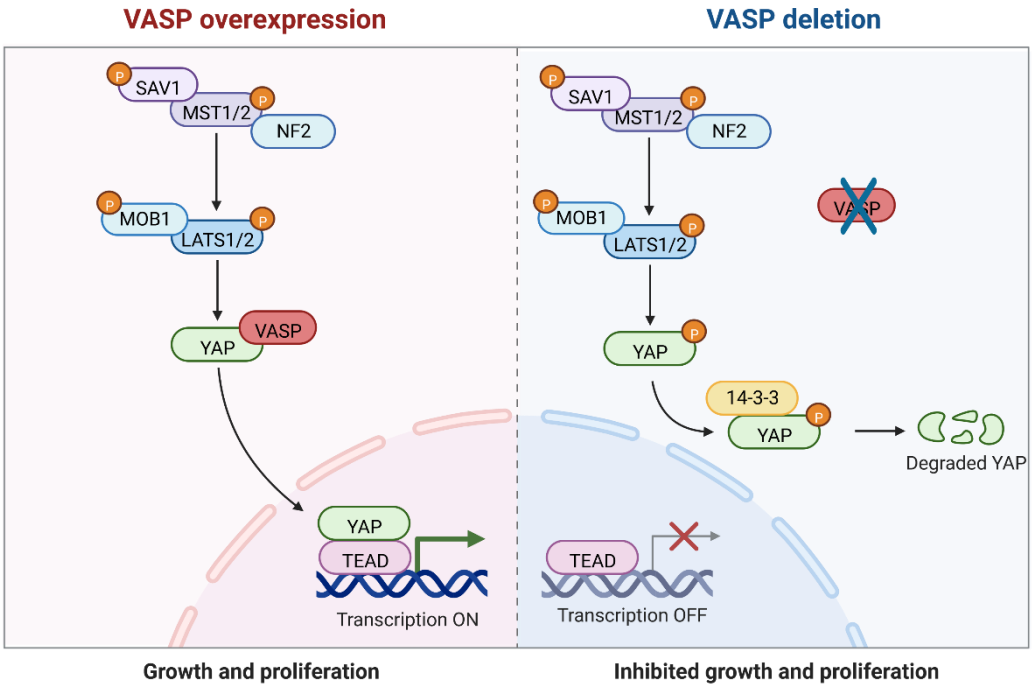

Figure 23: Working hypothesis how VASP potentially affects the Hippo/YAP signaling pathway. Adapted from "The Hippo Tumor-suppressor Pathway", by BioRender.com (2023). Retrieved from https://app.biorender.com/biorender-templates.

My findings and data from other groups indicated that VASP blocked the phosphorylation of YAP through direct interaction and thereby protected YAP from phosphorylation and degradation [154]. According to that, the VASP-YAP complex shuttled to the nucleus were VASP released YAP. After

shuttling from the cytoplasm to the nucleus, YAP and TEAD family members activated the transcription of its typical target genes. Interestingly, Li et al. described for the first time a nuclear localization of VASP in breast cancer cells. Here VASP interacted with components of the nuclear pore complex, like KPNA4. This protein is a transcriptional carrier, which enabled the shuttling of VASP in the nucleus by interaction with its EVH1 and EVH2 domains. In addition, the authors demonstrated that VASP directly binds β-catenin as well as DVL3 and promoted their translocation to the nucleus [180]. However, as my PLA analyses on VASP and YAP showed a predominant cytoplasmic interaction (very few VASP/YAP dots in the nucleus could be a result of cytoplasm covering the cell nuclei), I conclude that VASP under these experimental conditions was not shuttling into the nucleus with YAP.

To conclude, many studies pointed towards a tumor-supporting role of VASP in several cancer entities. In this study, I was able to disclose an influence of VASP abundance on YAP activity for the first time in HCC. Since VASP further associated with advanced tumor stages and reduced overall survival, VASP could serve as an independent prognostic factor predicting the survival of HCC patients.

5.5 DSG2 controls YAP activity via distinct mechanism

Desmogleins are dysregulated in various types of human cancers like colon, prostate, or cervical cancer [168][169][170]. Indeed, contradicting functions for this protein family either showing oncogenic or tumor suppressive functions have been described. For example, DSG2 was shown to be downregulated in lung and colon cancer, but highly expressed in cervical and ovarian cancer [185][168][170][186]. Therefore, DSGs may contribute to human cancer formation or progression *via* different mechanisms depending on their state of dysregulation. For example, it was shown that DSG2 upregulation activated Wnt/β-catenin signaling and promoted the conversion of normal cells into cancer stem cells [187]. In gastric cancer diminished DSG2 levels increased cell invasion and migration through EGFR/AKT and PG/β-catenin pathways [188]. Lastly, in lung adenocarcinoma DSG2 interacted with EGFR and thereby stimulated the EGFR/Src/PAK1 signaling pathway to promote tumorigenesis [185]. This data suggested that DSG2 dysregulation could support tumor cell biology *via* a plethora of mechanisms, probably in a (tumor) cell type-dependent manner.

In this study I was able to reveal an upregulation of DSG2 in HCC cells, which was associated with reduced patient survival and increased tumor cell proliferation and migration. Therefore, it was of interest to further investigate how DSG2 contributed to HCC malignancy and if these effects were mediated *via* YAP. Indeed, DSG2 overexpression statistically correlated with the expression of YAP

target genes, which supported this hypothesis. A possible influence of YAP on DSG2 (which could lead to a similar association between DSG2 and YAP activity) could be excluded at the mRNA level after YAP/TAZ silencing by siRNAs. Western blot and qPCR analysis after DSG2 inhibition revealed a reduction of total YAP levels, as well as YAP targets (CTGF, CYR61 and ANKRD1), indicating a reduction of YAP activity. Fractionation experiments and IF staining of liver cancer cells confirmed the decrease of total YAP and further disclosed its nuclear exclusion. Since pYAP levels were not affected, I hypothesized that this points towards an increase of YAP degradation in the cytoplasm (figure 24). Interestingly, these observations differed from the results after VASP silencing, where an increase of pYAP was detected. This indicated that VASP and DSG2 regulated YAP activity *via* distinct mechanisms. Indeed, the BioID analysis und subsequent confirmatory experiments identified YAP as direct interaction partner of VASP, whereas for DSG2 YAP was not detected.

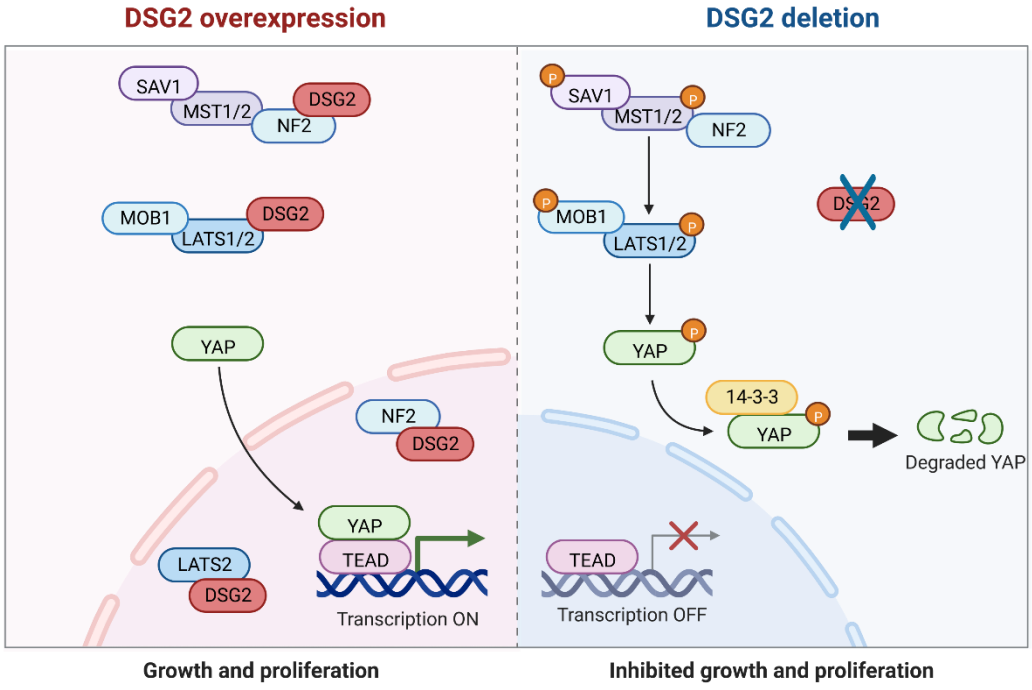

Figure 24: Working hypothesis how DSG2 potentially affects the Hippo/YAP signaling pathway. Adapted from "The Hippo Tumor-suppressor Pathway", by BioRender.com (2023). Retrieved from https://app.biorender.com/biorender-templates.

However, by using the BioID approach and Co-IP experiments, I was able to identify the YAP regulators NF2 and LATS2 as direct binding partners of DSG2 (figure 24). NF2 is a tumor suppressor which, together with MST1/2 and SAV1, promotes phosphorylation of LATS1/2, which in turn leads to phosphorylation and therefore inactivation of YAP [71]. PLA analysis further revealed that DSG2 and NF2 strongly interacted in the cytoplasm and the nucleus, while for DSG2 and LATS2 a weak, predominantly nuclear interaction was detected. Thus, DSG2 interacted with NF2 and LATS2 in

different cellular compartments. Previous studies have shown that DSG2 was localized at the cell membrane and in the cytoplasm, though no studies have mentioned its localization and potential role in cell nuclei [189]. Also, a direct interaction of DSG2 and NF2 and LAST2 was not described so far. However, NF2 and LATS2 were previously described to localize in the nucleus, where they contributed to increased YAP phosphorylation and thereby suppressed tumorigenesis [190][191]. According to these findings an interaction of DSG2 with NF2 and LATS2 could inhibit their tumor suppressive behavior as they cannot efficiently phosphorylate YAP in the cytoplasm and nucleus of HCC cells.

To conclude, I was able to show for the first time that DSG2 directly interacted with the tumor suppressors NF2 and LATS2 and thereby regulated YAP activity. Surprisingly, this interaction was predominantly detected in the nucleus (for LATS2) and nucleus/cytoplasm (for NF2), suggesting that DSG2 overexpression blocked YAP *via* mechanisms in different subcellular compartments. Interfering with these interactions e.g., by small molecule inhibitors could be a promising novel target for YAP-related therapy in HCC patients. As DSG2 contributed to tumorigenesis by different mechanisms in other tumor types, further work is required to test if DSG2/NF2 and DSG2/LATS2 interaction are important for YAP activity in other tumor entities.

5.6 Targeting junctional structures as novel therapy option in HCC with YAP activation

Primary liver cancer is the sixth most common cancer and the third most common cause of cancer-related death worldwide with a 5-year survival rate less than 20% [46][51]. Treatment of HCC is extremely difficult because of the high genetic heterogeneity of the tumor and the underlying cirrhosis, which itself impairs functionality of the remaining liver tissue and complicates conventional surgical approaches [52][53]. Therefore, the only treatment options are usually systemic therapies, including the administration of cytotoxic drugs (e.g. 5-fluoruracil, gemcitabine), treatment with the multi-kinase inhibitors (e.g. sorafenib, regorafenib) or novel immunotherapy (e.g. the combination of the PD-L1 targeting antibody atezolizumab with VEGF-targeting bevacizumab) [54]. However, these therapies only moderately prolong patient survival and even with therapy the survival time for most late-stage patients is around one year [55]. This sobering situation illustrates the necessity to investigate the therapeutic potential of novel target structures. YAP activity is often altered in HCC and represents a central oncogenic ‘driver’ in 30-50% of human HCCs [61][100]. Thus, targeting the Hippo pathway and its transcriptional effector YAP could be one promising treatment strategy for HCC patients. First experimental approaches are focusing on small

molecule inhibitors, that block the physical interaction of YAP and TEADs, which is usually associated with the degradation of YAP. For example, perturbation of the YAP/TEAD interaction by the small molecule inhibitor verteporfin leads to an inhibition of tumor growth in mice [192]. Indeed, due to various off-target effects, the compound did not reach the therapeutic application in clinics [193]. Another strategy is the alteration of YAP localization and stability, for example by pharmacological inhibition of the SCD1 protein, which inhibits nuclear translocation of YAP in lung cancer cells [194].

However, it is possible that direct targeting of YAP is not possible due to problems in the design of inhibitors or severe side effects. In this case the upregulation of upstream factors that modulate tumor-supporting YAP could serve as interesting alternative. My results revealed that DSG2 and VASP were upregulated in HCC and further statistically correlated with worse clinical outcome. Therefore, both could potentially be used as independent biomarkers for prognosis in HCC. In addition, I was able to demonstrate that VASP and DSG2 promoted HCC cell proliferation and migration via independent mechanisms. Therefore, targeting these mechanisms could be a promising novel treatment strategy in HCC, as the downregulation or inactivation of VASP and/or DSG2 could restore YAP phosphorylation and subsequent degradation, though to my knowledge, no approaches targeting junctional proteins have been successfully developed, yet.

To conclude, targeting protein-interactions is a commonly used strategy for anti-cancer therapies. Therefore, the newly detected DSG2 and VASP interactions with Hippo pathway constituents represents an interesting novel point of interference for the inactivation of YAP. Since the future of tumor therapies lies in the emerging field of personalized medicine, especially for heterogenous tumors like HCC, these data highlight the importance to gain more detailed knowledge about mechanism contributing to carcinogenesis.

6 References

1. Franke WW (2009) Discovering the molecular components of intercellular junctions--a historical view. Cold Spring Harb Perspect Biol 1:a003061
2. Adil MS, Narayanan SP, Somanath PR (2021) Cell-cell junctions: structure and regulation in physiology and pathology. Tissue Barriers 9:1848212
3. Garcia MA, Nelson WJ, Chavez N (2018) Cell-Cell Junctions Organize Structural and Signaling Networks. Cold Spring Harb Perspect Biol 10:a029181
4. Hartsock A, Nelson WJ (2008) Adherens and tight junctions: structure, function and connections to the actin cytoskeleton. Biochim Biophys Acta 1778:660–669
5. Rajasekaran AK, Hojo M, Huima T et al. (1996) Catenins and zonula occludens-1 form a complex during early stages in the assembly of tight junctions. J Cell Biol 132:451–463
6. Capaldo CT, Macara IG (2007) Depletion of E-cadherin disrupts establishment but not maintenance of cell junctions in Madin-Darby canine kidney epithelial cells. Mol Biol Cell 18:189–200
7. Lien W-H, Klezovitch O, Vasioukhin V (2006) Cadherin-catenin proteins in vertebrate development. Curr Opin Cell Biol 18:499–506
8. Zaidel-Bar R (2013) Cadherin adhesome at a glance. J Cell Sci 126:373–378
9. Gumbiner B, Stevenson B, Grimaldi A (1988) The role of the cell adhesion molecule uvomorulin in the formation and maintenance of the epithelial junctional complex. J Cell Biol 107:1575–1587
10. Coopman P, Djiane A (2016) Adherens Junction and E-Cadherin complex regulation by epithelial polarity. Cell Mol Life Sci 73:3535–3553
11. Green KJ, Jaiganesh A, Broussard JA (2019) Desmosomes: Essential contributors to an integrated intercellular junction network. F1000Research 8:2150
12. Hatzfeld M, Keil R, Magin TM (2017) Desmosomes and Intermediate Filaments: Their Consequences for Tissue Mechanics. Cold Spring Harb Perspect Biol 9
13. Müller L, Hatzfeld M, Keil R (2021) Desmosomes as Signaling Hubs in the Regulation of Cell Behavior. Front Cell Dev Biol 9:745670
14. Müller L, Hatzfeld M, Keil R (2021) Desmosomes as Signaling Hubs in the Regulation of Cell Behavior. Front Cell Dev Biol 9:745670
15. Getsios S, Simpson CL, Kojima S et al. (2009) Desmoglein 1-dependent suppression of EGFR signaling promotes epidermal differentiation and morphogenesis. J Cell Biol 185:1243–1258
16. Aktary Z, Kulak S, Mackey J et al. (2013) Plakoglobin interacts with the transcription factor p53 and regulates the expression of 14-3-3σ. J Cell Sci 126:3031–3042
17. Williamson L, Raess NA, Caldelari R et al. (2006) Pemphigus vulgaris identifies plakoglobin as key suppressor of c-Myc in the skin. EMBO J 25:3298–3309
18. Goodenough DA, Paul DL (2009) Gap junctions. Cold Spring Harb Perspect Biol 1:a002576
19. Morten Schak Nielsen, Lene Nygaard Axelsen, Paul L. Sorgen et al. (2012) Gap Junctions. In: Comprehensive Physiology, vol 2. John Wiley & Sons, Ltd, pp 1981–2035
20. Rodriguez-Boulan E, Macara IG (2014) Organization and execution of the epithelial polarity programme. Nat Rev Mol Cell Biol 15:225–242

21. Wodarz A, Näthke I (2007) Cell polarity in development and cancer. Nat Cell Biol 9:1016–1024

22. Buckley CE, St Johnston D (2022) Apical-basal polarity and the control of epithelial form and function. Nat Rev Mol Cell Biol 23:559–577

23. Halaoui R, McCaffrey L (2015) Rewiring cell polarity signaling in cancer. Oncogene 34:939–950

24. Gowrikumar S, Ahmad R, Uppada SB et al. (2019) Upregulated claudin-1 expression promotes colitis-associated cancer by promoting β-catenin phosphorylation and activation in Notch/p-AKT-dependent manner. Oncogene 38:5321–5337

25. Dhawan P, Ahmad R, Chaturvedi R et al. (2011) Claudin-2 expression increases tumorigenicity of colon cancer cells: role of epidermal growth factor receptor activation. Oncogene 30:3234–3247

26. Brennan D, Hu Y, Joubeh S et al. (2007) Suprabasal Dsg2 expression in transgenic mouse skin confers a hyperproliferative and apoptosis-resistant phenotype to keratinocytes. J Cell Sci 120:758–771

27. He B, Guo L, Hu Y et al. (2022) Desmocollin-2 inhibits cell proliferation and promotes apoptosis in hepatocellular carcinoma via the ERK/c-MYC signaling pathway. Aging (Albany NY) 14:8805–8817

28. Wheelock MJ, Shintani Y, Maeda M et al. (2008) Cadherin switching. J Cell Sci 121:727–735

29. Li S, Cong X, Gao H et al. (2019) Tumor-associated neutrophils induce EMT by IL-17a to promote migration and invasion in gastric cancer cells. J Exp Clin Cancer Res 38:6

30. Herzig M, Savarese F, Novatchkova M et al. (2007) Tumor progression induced by the loss of E-cadherin independent of beta-catenin/Tcf-mediated Wnt signaling. Oncogene 26:2290–2298

31. Valenta T, Hausmann G, Basler K (2012) The many faces and functions of β-catenin. EMBO J 31:2714–2736

32. Gordon MD, Nusse R (2006) Wnt signaling: multiple pathways, multiple receptors, and multiple transcription factors. J Biol Chem 281:22429–22433

33. Conacci-Sorrell M, Zhurinsky J, Ben-Ze'ev A (2002) The cadherin-catenin adhesion system in signaling and cancer. J Clin Invest 109:987–991

34. Treyer A, Müsch A (2013) Hepatocyte polarity. Compr Physiol 3:243–287

35. Gissen P, Arias IM (2015) Structural and functional hepatocyte polarity and liver disease. J Hepatol 63:1023–1037

36. Battle MA, Konopka G, Parviz F et al. (2006) Hepatocyte nuclear factor 4alpha orchestrates expression of cell adhesion proteins during the epithelial transformation of the developing liver. Proc Natl Acad Sci U S A 103:8419–8424

37. Zhu H, Lu J, Wang X et al. (2013) Upregulated ZO-1 correlates with favorable survival of gastrointestinal stromal tumor. Med Oncol 30:631

38. Willott E, Balda MS, Fanning AS et al. (1993) The tight junction protein ZO-1 is homologous to the Drosophila discs-large tumor suppressor protein of septate junctions. Proc Natl Acad Sci U S A 90:7834–7838

39. Cao Y, Chang H, Li L et al. (2007) Alteration of adhesion molecule expression and cellular polarity in hepatocellular carcinoma. Histopathology 51:528–538

40. Wan S, Meyer A-S, Weiler SME et al. (2018) Cytoplasmic localization of the cell polarity factor scribble supports liver tumor formation and tumor cell invasiveness. Hepatology 67:1842–1856

41. Vekemans K, Braet F (2005) Structural and functional aspects of the liver and liver sinusoidal cells in relation to colon carcinoma metastasis. World J Gastroenterol 11:5095–5102

42. Poisson J, Lemoinne S, Boulanger C et al. (2017) Liver sinusoidal endothelial cells: Physiology and role in liver diseases. J Hepatol 66:212–227

43. Dixon LJ, Barnes M, Tang H et al. (2013) Kupffer cells in the liver. Compr Physiol 3:785–797

44. Puche JE, Saiman Y, Friedman SL (2013) Hepatic stellate cells and liver fibrosis. Compr Physiol 3:1473–1492

45. Arjun Kalra, Ekrem Yetiskul, Chase J. Wehrle et al. (2022) Physiology, Liver. In: Kalra A, Yetiskul E, Wehrle CJ et al. (eds) StatPearls [Internet]. StatPearls Publishing

46. Sung H, Ferlay J, Siegel RL et al. (2021) Global Cancer Statistics 2020: GLOBOCAN Estimates of Incidence and Mortality Worldwide for 36 Cancers in 185 Countries. CA: A Cancer Journal for Clinicians 71:209–249

47. Yang JD, Hainaut P, Gores GJ et al. (2019) A global view of hepatocellular carcinoma: trends, risk, prevention and management. Nat Rev Gastroenterol Hepatol 16:589–604

48. McGlynn KA, Petrick JL, El-Serag HB (2021) Epidemiology of Hepatocellular Carcinoma. Hepatology 73 Suppl 1:4–13

49. Villanueva A, Newell P, Hoshida Y (2010) Inherited hepatocellular carcinoma. Best Pract Res Clin Gastroenterol 24:725–734

50. Dhanasekaran R, Bandoh S, Roberts LR (2016) Molecular pathogenesis of hepatocellular carcinoma and impact of therapeutic advances. F1000Research 5

51. Siegel RL, Miller KD, Jemal A (2018) Cancer statistics, 2018. CA: A Cancer Journal for Clinicians 68:7–30

52. Vogel A, Meyer T, Sapisochin G et al. (2022) Hepatocellular carcinoma. Lancet 400:1345–1362

53. Villanueva A (2019) Hepatocellular Carcinoma. N Engl J Med 380:1450–1462

54. Llovet JM, Castet F, Heikenwalder M et al. (2022) Immunotherapies for hepatocellular carcinoma. Nat Rev Clin Oncol 19:151–172

55. Chan SL, Wong AM, Lee K et al. (2016) Personalized therapy for hepatocellular carcinoma: Where are we now? Cancer Treatment Reviews 45:77–86

56. Zucman-Rossi J, Villanueva A, Nault J-C et al. (2015) Genetic Landscape and Biomarkers of Hepatocellular Carcinoma. Gastroenterology 149:1226-1239.e4

57. Schulze K, Nault J-C, Villanueva A (2016) Genetic profiling of hepatocellular carcinoma using next-generation sequencing. J Hepatol 65:1031–1042

58. Garcia-Lezana T, Lopez-Canovas JL, Villanueva A (2021) Signaling pathways in hepatocellular carcinoma. Adv Cancer Res 149:63–101

59. Plentz RR, Caselitz M, Bleck JS et al. (2004) Hepatocellular telomere shortening correlates with chromosomal instability and the development of human hepatoma. Hepatology 40:80–86

60. Carter SL, Eklund AC, Kohane IS et al. (2006) A signature of chromosomal instability inferred from gene expression profiles predicts clinical outcome in multiple human cancers. Nat Genet 38:1043–1048

61. Weiler SME, Pinna F, Wolf T et al. (2017) Induction of Chromosome Instability by Activation of Yes-Associated Protein and Forkhead Box M1 in Liver Cancer. Gastroenterology 152:2037-2051.e22

62. Dratwa M, Wysoczańska B, Łacina P et al. (2020) TERT-Regulation and Roles in Cancer Formation. Front Immunol 11:589929

63. Fan X, Jin S, Li Y et al. (2019) Genetic And Epigenetic Regulation Of E-Cadherin Signaling In Human Hepatocellular Carcinoma. Cancer Manag Res 11:8947–8963

64. Kim N-G, Koh E, Chen X et al. (2011) E-cadherin mediates contact inhibition of proliferation through Hippo signaling-pathway components. Proc Natl Acad Sci U S A 108:11930–11935

65. Boyault S, Rickman DS, Reyniès A de et al. (2007) Transcriptome classification of HCC is related to gene alterations and to new therapeutic targets. Hepatology 45:42–52

66. Nakagawa H, Hikiba Y, Hirata Y et al. (2014) Loss of liver E-cadherin induces sclerosing cholangitis and promotes carcinogenesis. Proc Natl Acad Sci U S A 111:1090–1095

67. Valletta D, Czech B, Spruss T et al. (2014) Regulation and function of the atypical cadherin FAT1 in hepatocellular carcinoma. Carcinogenesis 35:1407–1415

68. Xu C, Xu Z, Zhang Y et al. (2022) β-Catenin signaling in hepatocellular carcinoma. J Clin Invest 132

69. Grammont M (2007) Adherens junction remodeling by the Notch pathway in Drosophila melanogaster oogenesis. J Cell Biol 177:139–150

70. Zhao B, Lei Q-Y, Guan K-L (2008) The Hippo-YAP pathway: new connections between regulation of organ size and cancer. Curr Opin Cell Biol 20:638–646

71. Ma S, Meng Z, Chen R et al. (2019) The Hippo Pathway: Biology and Pathophysiology. Annu Rev Biochem 88:577–604

72. Yu F-X, Zhao B, Guan K-L (2015) Hippo Pathway in Organ Size Control, Tissue Homeostasis, and Cancer. Cell 163:811–828

73. Zhao B, Ye X, Yu J et al. (2008) TEAD mediates YAP-dependent gene induction and growth control. Genes Dev 22:1962–1971

74. Chuang LSH, Ito Y (2021) The Multiple Interactions of RUNX with the Hippo-YAP Pathway. Cells 10:2925

75. Varelas X, Samavarchi-Tehrani P, Narimatsu M et al. (2010) The Crumbs complex couples cell density sensing to Hippo-dependent control of the TGF-β-SMAD pathway. Dev Cell 19:831–844

76. Wang Y, Xu X, Maglic D et al. (2018) Comprehensive Molecular Characterization of the Hippo Signaling Pathway in Cancer. Cell Rep 25:1304-1317.e5

77. Zhang Y, Shen H, Withers HG et al. (2017) VGLL4 Selectively Represses YAP-Dependent Gene Induction and Tumorigenic Phenotypes in Breast Cancer. Sci Rep 7:6190

78. Meng Z, Moroishi T, Guan K-L (2016) Mechanisms of Hippo pathway regulation. Genes Dev 30:1–17

79. Chan EHY, Nousiainen M, Chalamalasetty RB et al. (2005) The Ste20-like kinase Mst2 activates the human large tumor suppressor kinase Lats1. Oncogene 24:2076–2086

80. Zhao B, Wei X, Li W et al. (2007) Inactivation of YAP oncoprotein by the Hippo pathway is involved in cell contact inhibition and tissue growth control. Genes Dev 21:2747–2761

81. Zhao B, Li L, Tumaneng K et al. (2010) A coordinated phosphorylation by Lats and CK1 regulates YAP stability through SCF(beta-TRCP). Genes Dev 24:72–85

82. Piccolo S, Dupont S, Cordenonsi M (2014) The biology of YAP/TAZ: hippo signaling and beyond. Physiol Rev 94:1287–1312

83. Yin F, Yu J, Zheng Y et al. (2013) Spatial organization of Hippo signaling at the plasma membrane mediated by the tumor suppressor Merlin/NF2. Cell 154:1342–1355

84. Yu F-X, Zhao B, Panupinthu N et al. (2012) Regulation of the Hippo-YAP pathway by G-protein-coupled receptor signaling. Cell 150:780–791

85. Hanahan D (2022) Hallmarks of Cancer: New Dimensions. Cancer Discov 12:31–46

86. Cao J, Huang W (2017) Two faces of Hippo: activate or suppress the Hippo pathway in cancer. Anticancer Drugs 28:1079–1085

87. Zanconato F, Cordenonsi M, Piccolo S (2016) YAP/TAZ at the Roots of Cancer. Cancer Cell 29:783–803

88. Zhang W, Gao Y, Li F et al. (2015) YAP promotes malignant progression of Lkb1-deficient lung adenocarcinoma through downstream regulation of survivin. Cancer Res 75:4450–4457

89. Kang W, Tong JHM, Chan AWH et al. (2011) Yes-associated protein 1 exhibits oncogenic property in gastric cancer and its nuclear accumulation associates with poor prognosis. Clin Cancer Res 17:2130–2139

90. Steinhardt AA, Gayyed MF, Klein AP et al. (2008) Expression of Yes-associated protein in common solid tumors. Human Pathology 39:1582–1589

91. Avruch J, Zhou D, Bardeesy N (2012) YAP oncogene overexpression supercharges colon cancer proliferation. Cell Cycle 11:1090–1096

92. St John MA, Tao W, Fei X et al. (1999) Mice deficient of Lats1 develop soft-tissue sarcomas, ovarian tumours and pituitary dysfunction. Nat Genet 21:182–186

93. Nishio M, Hamada K, Kawahara K et al. (2012) Cancer susceptibility and embryonic lethality in Mob1a/1b double-mutant mice. J Clin Invest 122:4505–4518

94. Evans DGR (2009) Neurofibromatosis 2 Bilateral acoustic neurofibromatosis, central neurofibromatosis, NF2, neurofibromatosis type II. Genet Med 11:599–610

95. Johnson R, Halder G (2014) The two faces of Hippo: targeting the Hippo pathway for regenerative medicine and cancer treatment. Nat Rev Drug Discov 13:63–79

96. Overholtzer M, Zhang J, Smolen GA et al. (2006) Transforming properties of YAP, a candidate oncogene on the chromosome 11q22 amplicon. Proc Natl Acad Sci U S A 103:12405–12410

97. Xu MZ, Yao T-J, Lee NPY et al. (2009) Yes-associated protein is an independent prognostic marker in hepatocellular carcinoma. Cancer 115:4576–4585

98. Tschaharganeh DF, Chen X, Latzko P et al. (2013) Yes-associated protein up-regulates Jagged-1 and activates the Notch pathway in human hepatocellular carcinoma. Gastroenterology 144:1530-1542.e12

99. Lin C, Hu Z, Lei B et al. (2017) Overexpression of Yes-associated protein and its association with clinicopathological features of hepatocellular carcinoma: A meta-analysis. Liver Int 37:1675–1681

100. Zender L, Spector MS, Xue W et al. (2006) Identification and validation of oncogenes in liver cancer using an integrative oncogenomic approach. Cell 125:1253–1267

101. Camargo FD, Gokhale S, Johnnidis JB et al. (2007) YAP1 increases organ size and expands undifferentiated progenitor cells. Curr Biol 17:2054–2060

102. Dong J, Feldmann G, Huang J et al. (2007) Elucidation of a universal size-control mechanism in Drosophila and mammals. Cell 130:1120–1133

103. Zhang N, Bai H, David KK et al. (2010) The Merlin/NF2 tumor suppressor functions through the YAP oncoprotein to regulate tissue homeostasis in mammals. Dev Cell 19:27–38

104. Zhou D, Conrad C, Xia F et al. (2009) Mst1 and Mst2 maintain hepatocyte quiescence and suppress hepatocellular carcinoma development through inactivation of the Yap1 oncogene. Cancer Cell 16:425–438

105. Schmittgen TD, Livak KJ (2008) Analyzing real-time PCR data by the comparative C(T) method. Nat Protoc 3:1101–1108

106. Vandesompele J, Preter K de, Pattyn F et al. (2002) Accurate normalization of real-time quantitative RT-PCR data by geometric averaging of multiple internal control genes. Genome Biol 3:RESEARCH0034

107. Tyanova S, Temu T, Sinitcyn P et al. (2016) The Perseus computational platform for comprehensive analysis of (prote)omics data. Nat Methods 13:731–740

108. Schindelin J, Arganda-Carreras I, Frise E et al. (2012) Fiji: an open-source platform for biological-image analysis. Nat Methods 9:676–682

109. Arganda-Carreras I, Kaynig V, Rueden C et al. (2017) Trainable Weka Segmentation: a machine learning tool for microscopy pixel classification. Bioinformatics 33:2424–2426

110. Chen X, Calvisi DF (2014) Hydrodynamic transfection for generation of novel mouse models for liver cancer research. Am J Pathol 184:912–923

111. Roessler S, Jia H-L, Budhu A et al. (2010) A unique metastasis gene signature enables prediction of tumor relapse in early-stage hepatocellular carcinoma patients. Cancer Res 70:10202–10212

112. Ally A, Balasundaram M, Carlsen R et al. (2017) Comprehensive and Integrative Genomic Characterization of Hepatocellular Carcinoma. Cell 169:1327-1341.e23

113. Budczies J, Klauschen F, Sinn BV et al. (2012) Cutoff Finder: a comprehensive and straightforward Web application enabling rapid biomarker cutoff optimization. PLoS One 7:e51862

114. Gao J, Aksoy BA, Dogrusoz U et al. (2013) Integrative analysis of complex cancer genomics and clinical profiles using the cBioPortal. Sci Signal 6:pl1

115. Cerami E, Gao J, Dogrusoz U et al. (2012) The cBio cancer genomics portal: an open platform for exploring multidimensional cancer genomics data. Cancer Discov 2:401–404

116. Broad DepMap (2022) DepMap 22Q2 Public. figshare

117. Weiler SME, Lutz T, Bissinger M et al. (2020) TAZ target gene ITGAV regulates invasion and feeds back positively on YAP and TAZ in liver cancer cells. Cancer Lett 473:164–175

118. Fernández BG, Gaspar P, Brás-Pereira C et al. (2011) Actin-Capping Protein and the Hippo pathway regulate F-actin and tissue growth in Drosophila. Development 138:2337–2346

119. Cheung YK, Klotz JH (1997) The Mann-Whitney Wilcoxon distribution using linked lists. Statistica Sinica 7:805–813

120. Sarpal R, Yan V, Kazakova L et al. (2019) Role of α-Catenin and its mechanosensing properties in regulating Hippo/YAP-dependent tissue growth. PLoS Genet 15:e1008454

121. Silvis MR, Kreger BT, Lien W-H et al. (2011) α-catenin is a tumor suppressor that controls cell accumulation by regulating the localization and activity of the transcriptional coactivator Yap1. Sci Signal 4:ra33

122. He B, Li T, Guan L et al. (2016) CTNNA3 is a tumor suppressor in hepatocellular carcinomas and is inhibited by miR-425. Oncotarget 7:8078–8089

123. Zhang S, Xu Y, Xie C et al. (2021) RNF219/α-Catenin/LGALS3 Axis Promotes Hepatocellular Carcinoma Bone Metastasis and Associated Skeletal Complications. Adv Sci (Weinh) 8:2001961

124. Zimmer M, Fink T, Fischer L et al. (1996) Cloning of the VASP (vasodilator-stimulated phosphoprotein) genes in human and mouse: structure, sequence, and chromosomal localization. Genomics 36:227–233

125. Whittock NV, Bower C (2003) Genetic evidence for a novel human desmosomal cadherin, desmoglein 4. J Invest Dermatol 120:523–530

126. Gao Q, Zhu H, Dong L et al. (2019) Integrated Proteogenomic Characterization of HBV-Related Hepatocellular Carcinoma. Cell 179:1240

127. Ilyas A, Hashim Z, Zarina S (2015) Effects of 5'-azacytidine and alendronate on a hepatocellular carcinoma cell line: a proteomics perspective. Mol Cell Biochem 405:53–61

128. Issa J-PJ, Kantarjian HM (2009) Targeting DNA methylation. Clin Cancer Res 15:3938–3946

129. Al-Jamal HAN, Mat Jusoh SA, Hassan R et al. (2015) Enhancing SHP-1 expression with 5-azacytidine may inhibit STAT3 activation and confer sensitivity in lestaurtinib (CEP-701)-resistant FLT3-ITD positive acute myeloid leukemia. BMC Cancer 15:869

130. Wen L-Z, Ding K, Wang Z-R et al. (2018) SHP-1 Acts as a Tumor Suppressor in Hepatocarcinogenesis and HCC Progression. Cancer Res 78:4680–4691

131. Donato MT, Tolosa L, Gómez-Lechón MJ (2015) Culture and Functional Characterization of Human Hepatoma HepG2 Cells. Methods Mol Biol 1250:77–93

132. Dor I, Namba M, Sato J (1975) Establishment and some biological characteristics of human hepatoma cell lines. Gan 66:385–392

133. Roux KJ, Kim D in, Raida M et al. (2012) A promiscuous biotin ligase fusion protein identifies proximal and interacting proteins in mammalian cells. J Cell Biol 196:801–810

134. Hulpiau P, van Roy F (2009) Molecular evolution of the cadherin superfamily. Int J Biochem Cell Biol 41:349–369

135. Harrison OJ, Brasch J, Lasso G et al. (2016) Structural basis of adhesive binding by desmocollins and desmogleins. Proc Natl Acad Sci U S A 113:7160–7165

136. Chitaev NA, Averbakh AZ, Troyanovsky RB et al. (1998) Molecular organization of the desmoglein-plakoglobin complex. J Cell Sci 111 (Pt 14):1941–1949

137. Chen X, Bonne S, Hatzfeld M et al. (2002) Protein binding and functional characterization of plakophilin 2. Evidence for its diverse roles in desmosomes and beta -catenin signaling. J Biol Chem 277:10512–10522

138. Bonné S, Gilbert B, Hatzfeld M et al. (2003) Defining desmosomal plakophilin-3 interactions. J Cell Biol 161:403–416

139. Disanza A, Carlier M-F, Stradal TEB et al. (2004) Eps8 controls actin-based motility by capping the barbed ends of actin filaments. Nat Cell Biol 6:1180–1188

140. Chen C, Liang Z, Huang W et al. (2015) Eps8 regulates cellular proliferation and migration of breast cancer. International Journal of Oncology 46:205–214

141. Yang G, Lu Y-B, Guan Q-L (2019) EPS8 is a Potential Oncogene in Glioblastoma. Onco Targets Ther 12:10523–10534

142. Rivera J, Megías D, Bravo J (2010) Sorting nexin 6 interacts with breast cancer metastasis suppressor-1 and promotes transcriptional repression. Journal of Cellular Biochemistry 111:1464–1472

143. Hu P, Liang Y, Hu Q et al. (2018) SNX6 predicts poor prognosis and contributes to the metastasis of pancreatic cancer cells via activating epithelial-mesenchymal transition. Acta Biochim Biophys Sin (Shanghai) 50:1075–1084

144. Sundararaj S, Ravindran A, Casarotto MG (2021) AHNAK: The quiet giant in calcium homeostasis. Cell Calcium 96:102403

145. Cai Y, Hu Y, Yu F et al. (2021) AHNAK suppresses ovarian cancer progression through the Wnt/β-catenin signaling pathway. Aging (Albany NY) 13:23579–23587

146. Chen B, Wang J, Dai D et al. (2017) AHNAK suppresses tumour proliferation and invasion by targeting multiple pathways in triple-negative breast cancer. J Exp Clin Cancer Res 36:65

147. Ao J-Y, Chai Z-T, Zhang Y-Y et al. (2015) Robo1 promotes angiogenesis in hepatocellular carcinoma through the Rho family of guanosine triphosphatases' signaling pathway. Tumour Biol 36:8413–8424

148. Chang J, Lan T, Li C et al. (2015) Activation of Slit2-Robo1 signaling promotes liver fibrosis. J Hepatol 63:1413–1420

149. Guo C, Wang X, Liang L (2015) LATS2-mediated YAP1 phosphorylation is involved in HCC tumorigenesis. Int J Clin Exp Pathol 8:1690–1697

150. Lavado A, He Y, Paré J et al. (2013) Tumor suppressor Nf2 limits expansion of the neural progenitor pool by inhibiting Yap/Taz transcriptional coactivators. Development 140:3323–3334

151. Reinhard M, Rüdiger M, Jockusch BM et al. (1996) VASP interaction with vinculin: a recurring theme of interactions with proline-rich motifs. FEBS Lett 399:103–107

152. Lawrence DW, Comerford KM, Colgan SP (2002) Role of VASP in reestablishment of epithelial tight junction assembly after Ca2+ switch. Am J Physiol Cell Physiol 282:C1235-45

153. Lee C-J, An H-J, Cho ES et al. (2020) Stat2 stability regulation: an intersection between immunity and carcinogenesis. Exp Mol Med 52:1526–1536

154. Xiang X, Wang Y, Zhang H et al. (2018) Vasodilator-stimulated phosphoprotein promotes liver metastasis of gastrointestinal cancer by activating a β1-integrin-FAK-YAP1/TAZ signaling pathway. NPJ Precis Oncol 2:2

155. Liu Z, Wang Y, Dou C et al. (2018) Hypoxia-induced up-regulation of VASP promotes invasiveness and metastasis of hepatocellular carcinoma. Theranostics 8:4649–4663

156. Han C-P, Yu Y-H, Wang A-G et al. (2018) Desmoglein-2 overexpression predicts poor prognosis in hepatocellular carcinoma patients. Eur Rev Med Pharmacol Sci 22:5481–5489

157. Schlegelmilch K, Mohseni M, Kirak O et al. (2011) Yap1 acts downstream of α-catenin to control epidermal proliferation. Cell 144:782–795

158. Ghosh R, Gilda JE, Gomes AV (2014) The necessity of and strategies for improving confidence in the accuracy of western blots. Expert Rev Proteomics 11:549–560

159. Alam MS (2018) Proximity Ligation Assay (PLA). Curr Protoc Immunol 123:e58

160. Roux KJ, Kim D in, Burke B et al. (2018) BioID: A Screen for Protein-Protein Interactions. Curr Protoc Protein Sci 91:19.23.1-19.23.15

161. Kim D in, Birendra KC, Zhu W et al. (2014) Probing nuclear pore complex architecture with proximity-dependent biotinylation. Proc Natl Acad Sci U S A 111:E2453-61

162. Zafra F, Piniella D (2022) Proximity labeling methods for proteomic analysis of membrane proteins. Journal of Proteomics 264:104620

163. Li Y, Merkel CD, Zeng X et al. (2019) The N-cadherin interactome in primary cardiomyocytes as defined using quantitative proximity proteomics. J Cell Sci 132

164. Guo Z, Neilson LJ, Zhong H et al. (2014) E-cadherin interactome complexity and robustness resolved by quantitative proteomics. Sci Signal 7:rs7

165. Baskaran Y, Tay FP-L, Ng EYW et al. (2021) Proximity proteomics identifies PAK4 as a component of Afadin–Nectin junctions. Nat Commun 12

166. van Itallie CM, Aponte A, Tietgens AJ et al. (2013) The N and C Termini of ZO-1 Are Surrounded by Distinct Proteins and Functional Protein Networks. J Biol Chem 288:13775–13788

167. Waschke J (2008) The desmosome and pemphigus. Histochem Cell Biol 130:21–54

168. Yang T, Gu X, Jia L et al. (2021) DSG2 expression is low in colon cancer and correlates with poor survival. BMC Gastroenterol 21:7

169. Barber AG, Castillo-Martin M, Bonal DM et al. (2014) Characterization of desmoglein expression in the normal prostatic gland. Desmoglein 2 is an independent prognostic factor for aggressive prostate cancer. PLoS One 9:e98786

170. Qin S, Liao Y, Du Q et al. (2020) DSG2 expression is correlated with poor prognosis and promotes early-stage cervical cancer. Cancer Cell Int 20:206

171. Chen Y-J, Chang JT, Lee L et al. (2007) DSG3 is overexpressed in head neck cancer and is a potential molecular target for inhibition of oncogenesis. Oncogene 26:467–476

172. Myklebust MP, Fluge Ø, Immervoll H et al. (2012) Expression of DSG1 and DSC1 are prognostic markers in anal carcinoma patients. Br J Cancer 106:756–762

173. Kljuic A, Bazzi H, Sundberg JP et al. (2003) Desmoglein 4 in hair follicle differentiation and epidermal adhesion: evidence from inherited hypotrichosis and acquired pemphigus vulgaris. Cell 113:249–260

174. Saaber F, Chen Y, Cui T et al. (2015) Expression of desmogleins 1-3 and their clinical impacts on human lung cancer. Pathol Res Pract 211:208–213

175. Kottke MD, Delva E, Kowalczyk AP (2006) The desmosome: cell science lessons from human diseases. J Cell Sci 119:797–806

176. Brennan D, Mahoney MG (2009) Increased expression of Dsg2 in malignant skin carcinomas: A tissue-microarray based study. Cell Adhesion & Migration 3:148–154

177. Simpson CL, Patel DM, Green KJ (2011) Deconstructing the skin: cytoarchitectural determinants of epidermal morphogenesis. Nat Rev Mol Cell Biol 12:565–580

178. Mahoney MG, Hu Y, Brennan D et al. (2006) Delineation of diversified desmoglein distribution in stratified squamous epithelia: implications in diseases. Experimental Dermatology 15:101–109

179. Faix J, Rottner K (2022) Ena/VASP proteins in cell edge protrusion, migration and adhesion. J Cell Sci 135

180. Li K, Zhang J, Tian Y et al. (2020) The Wnt/β-catenin/VASP positive feedback loop drives cell proliferation and migration in breast cancer. Oncogene 39:2258–2274

181. Dertsiz L, Ozbilim G, Kayisli Y et al. (2005) Differential expression of VASP in normal lung tissue and lung adenocarcinomas. Thorax 60:576–581

182. Wang J, Zhang J, Wu J et al. (2012) MicroRNA-610 inhibits the migration and invasion of gastric cancer cells by suppressing the expression of vasodilator-stimulated phosphoprotein. Eur J Cancer 48:1904–1913

183. Galler AB, García Arguinzonis MI, Baumgartner W et al. (2006) VASP-dependent regulation of actin cytoskeleton rigidity, cell adhesion, and detachment. Histochem Cell Biol 125:457–474

184. Dang Y, Chen J, Feng W et al. (2020) Interleukin 1β-mediated HOXC10 Overexpression Promotes Hepatocellular Carcinoma Metastasis by Upregulating PDPK1 and VASP. Theranostics 10:3833–3848

185. Jin R, Wang X, Zang R et al. (2020) Desmoglein-2 modulates tumor progression and osimertinib drug resistance through the EGFR/Src/PAK1 pathway in lung adenocarcinoma. Cancer Lett 483:46–58

186. Kim J, Beidler P, Wang H et al. (2020) Desmoglein-2 as a prognostic and biomarker in ovarian cancer. Cancer Biol Ther 21:1154–1162

187. Chen L, Liu Y, Xu Y et al. (2023) Up-regulation of Dsg2 confered stem cells with malignancy through wnt/β-catenin signaling pathway. Exp Cell Res 422:113416

188. Yang T, Jia L, Bian S et al. (2022) TROP2 Down-regulated DSG2 to Promote Gastric Cancer Cell Invasion and Migration by EGFR/AKT and DSG2/PG/β-Catenin Pathways. Curr Cancer Drug Targets 22:691–702

189. Gupta A, Nitoiu D, Brennan-Crispi D et al. (2015) Cell cycle- and cancer-associated gene networks activated by Dsg2: evidence of cystatin A deregulation and a potential role in cell-cell adhesion. PLoS One 10:e0120091

190. Li W, Cooper J, Zhou L et al. (2014) Merlin/NF2 loss-driven tumorigenesis linked to CRL4(DCAF1)-mediated inhibition of the hippo pathway kinases Lats1 and 2 in the nucleus. Cancer Cell 26:48–60

191. Wehling L, Keegan L, Fernández-Palanca P et al. (2022) Spatial modeling reveals nuclear phosphorylation and subcellular shuttling of YAP upon drug-induced liver injury. Elife 11

192. Liu-Chittenden Y, Huang B, Shim JS et al. (2012) Genetic and pharmacological disruption of the TEAD-YAP complex suppresses the oncogenic activity of YAP. Genes Dev 26:1300–1305

193. Dasari VR, Mazack V, Feng W et al. (2017) Verteporfin exhibits YAP-independent anti-proliferative and cytotoxic effects in endometrial cancer cells. Oncotarget 8:28628–28640

194. Noto A, Vitis C de, Pisanu ME et al. (2017) Stearoyl-CoA-desaturase 1 regulates lung cancer stemness via stabilization and nuclear localization of YAP/TAZ. Oncogene 36:4573–4584

List of Figures

List of Tables

List of Abbreviations

ACN	Acetonitrile
ACTB	Beta-actin
AJ	Adherens junctions
ALD	Alcoholic liver disease
ANKRD1	Ankyrin repeat domain 1
ASH	Alcoholic steatohepatitis
BirA	Biotin ligase
CCLE	Cancer Cell Line Encyclopedia
cDNA	Complementary DNA
CIN	Chromosomal instability
Co-IP	Co-immunoprecipitation
CTGF	Connective tissue growth factor
CTNNA1	Alpha-catenin
CTNNB1	Beta-catenin
CYR61	Cysteine-rich angiogenic inducer 61
DNTM1	DNA methyltransferase
Dox	Doxycycline hyclate
DSC	Desmocollin
DSG	Desmoglein
ECM	Extracellular matrix
EMT	Epithelial-to-mesenchymal transition
EPS8	Epidermal growth factor receptor kinase substrate 8
FA	Formic acid
fc	Fold change
GAPDH	Glyceraldehyde-3-phosphate dehydrogenase
GJ	Gap junction
GPCR	G protein-coupled receptor
HBV	Hepatitis B virus
HCC	Hepatocellular carcinoma
HCV	Hepatitis C virus
HDTVI	Hydrodynamic tail vein injection
HNF-4α	Hepatocyte nuclear factor 4-alpha
IF	Immunofluorescence
IgG	Immunoglobulin G
IHC	Immunohistochemistry
JAM	Junctional adhesion molecule
JUP	Plakoglobin
LATS1/2	Large tumor suppressor kinase 1/2
LC-MS/MS	Liquid chromatography coupled mass spectrometry analysis
MOB1	Mps one binder kinase activator-like 1
mRNA	messenger RNA

MS	Mass spectrometry
MST1/2	Mammalian STE20-like protein kinase 1/2
NAFLD	Non-alcoholic fatty acid liver disease
NASH	Non-alcoholic steatohepatitis
NCT	Nationales Zentrum für Tumorerkrankungen
NF2	Neurofibromatosis type 2; synonym: Merlin
ns	Not significant
NTC	Non-targeting control
PAGE	Polyacrylamide gel electrophoresis
PBS	Phosphate buffered saline
PCR	Polymerase chain reaction
PKP-2/3	Plakophilin 2/3
PLA	Proximity ligation assay
pYAP	Phosphorylated YAP
qPCR	Semi-quantitative real-time PCR
RNAi	RNA interference
ROBO1	Roundabout homolog 1
RUNX-1/2	Runt-related transcription factor 1/2
SAV1	Salvador family WW domain-containing protein 1
SD	Standard deviation
SDS	Sodium-dodecylsulfate
SHP1	Src homology region 2 domain-containing phosphatase
siRNA	small-interfering RNA
SMAD-2/3	Mothers against decapentaplegic homolog 2/3
SNX6	Nexin 6
STAT2	Signal transducer and activator of transcript 2
TAZ	Transcriptional co-activator with PDZ-binding motif
TEAB	Tetrahydroborate buffer
TEAD-1-4	TEA domain family members 1-4
TERT	Telomerase reverse transcriptase
TFA	Trifluoroacetic acid
TJ	Tight junctions
TMA	Tissue micro-array
VASP	Vasodilator-stimulated phosphoprotein
VGLL4	Vestigial-like protein 4
Wnt	Wingless
YAP	Yes-associated protein
ZO	Zonula occludens protein

Acknowledgements

Zunächst möchte ich mich bei Prof. Dr. Peter Schirmacher und Prof. Dr. Kai Breuhahn bedanken, die mir die Durchführung der vorliegenden Arbeit am Pathologischen Institut des Universitätsklinikums Heidelberg ermöglich haben.

Ganz besonders bedanken möchte ich mich bei Prof. Dr. Kai Breuhahn, der mir dieses spannende Projekt anvertraut und diese Dissertation begutachtet hat. Kai, vielen Dank für die jederzeit offene Tür, die konstruktiven Ratschläge und dein in mich gesetztes Vertrauen, sowie die produktive Arbeitsatmosphäre und dass du mir immer mit Rat und Tat zur Seite standest.

Des Weiteren möchte ich mich bei Prof. Dr. Peter Angel bedanken, der sich bereiterklärt hat diese Arbeit zu begutachten und vor der Biowissenschaftlichen Fakultät der Universität Heidelberg zu vertreten.

Ich möchte mich auch herzlich bei Prof. Dr. Stefan Wölfl und Prof. Dr. Ilse Hofmann für die Bereitschaft bedanken, als Prüfer in meiner Disputation zu fungieren.

Des Weiteren möchte ich Dr. Thomas Ruppert und Sabine Merker für die Durchführung und Prozessierung der Proteomik Messungen am Zentrum für Molekulare Biologie der Universität Heidelberg danken.

Für die Hilfe bei der Etablierung und Durchführung unzähliger IHC-Färbungen und die unkomplizierte Zusammenarbeit möchte ich mich bei Dr. Tanja Poth und dem IHC-Team Heike, Christine, Karin und Diana bedanken.

Des Weiteren bedanke ich mich bei Dr. Esther Herpel und Dr. Alexander Brobeil, sowie Fabio, Veronika und Marcell von der Gewebebank des NCT für die Bereitstellung und Digitalisierung von Gewebeproben.

Ganz besonders bedanken möchte ich mich bei Fabi, Thorben, Noujan, Lilija und Damaris für die vielen großartigen Momente, Gespräche und Erlebnisse bei und außerhalb der Arbeit; sei es ein Feierabend Bier, eine Runde Fußballgolf oder ein motivierendes Gespräch, durch euch wurde dir Zeit unvergesslich!

Ein großes Dankeschön geht auch an Michaela, Jenny und Eva. Vielen Dank für alles was ihr mir an Labordingen beigebracht habt und dass ihr bei Fragen und Problemen jederzeit ein offenes Ohr und eine helfende Hand für mich hattet.

Ich möchte mich auch bei allen ehemaligen und aktuellen Labormitgliedern bedanken; Yingyue, Sofia, Fabian, Patrizia, Geli, Sarah, Rossella, Jasmin, Raisa, Asli, Feli, Bianca, Kaijing und Marie, vielen Dank für die angenehme Arbeitsatmosphäre und eure Unterstützung bei allen möglichen Fragen.

Zuletzt möchte ich mich ganz besonders bei meiner Familie und vor allem Daniel bedanken. Vielen Dank dass ihr mich immer unterstützt, mich motiviert und an mich geglaubt habt!

Appendix

Supplement Table 1: Selected genes for the screening approach. All selected mRNAs which were analyzed in TCGA and LCI cohort are listed, including their function, their Ref seq number and the screening results.

			Expression		Survival		Correlation	
Protein name	**Gene name**	**Ref seq**	**TCGA**	**LCI**	**TCGA**	**LCI**	**TCGA**	**LCI**
Cadherin-1	CDH1	NM_004360.5	***	***	**	**		*
Cadherin-2	CDH2	NM_001792.5	***	***		**		
Cadherin-3	CDH3	NM_001792.5		***				
Cadherin-4	CDH4	NM_001794.5	***	***				
Cadherin-5	CDH5	NM_001795.5	*					
Cadherin-6	CDH6	NM_004932.4		***				
Cadherin-7	CDH7	NM_004361.5	*	**		***		
Cadherin-8	CDH8	NM_001796.5	***	***				
Cadherin-9	CDH9	NM_016279.4	***	*				
Cadherin-10	CDH10	NM_006727.5	**	**	***	*	***	
Cadherin-11	CDH11	NM_001797.4	**	*				
Cadherin-12	CDH12	NM_004061.5	***					
Cadherin-13	CDH13	NM_001257.5	***	***		***		
Cadherin-15	CDH15	NM_004933.3	**	***	*	*		***
Cadherin-16	CDH16	NM_004062.4		**				
Cadherin-17	CDH17	NM_004063.4		***				
Cadherin-18	CDH18	NM_004934.5	**	***	***			
Cadherin-19	CDH19	NM_021153.4	***	***	*			
Cadherin-20	CDH20	NM_031891.4		**				
Cadherin-22	CDH22	NM_021248.3		***				
Protocadherin-16	DCHS1	NM_003737.4	**	***				
Desmocollin-1	DSC1	NM_024421.2		***				
Desmocollin-2	DSC2	NM_024422.6	***	***		*		
Desmocollin-3	DSC3	NM_001941.5	***	***		*		
Desmoglein-1	**DSG1**	**NM_001942.4**	***	***	**	**	***	***
Desmoglein-2	**DSG2**	**NM_001943.5**	**	***	**	***	***	***
Desmoglein-3	DSG3	NM_001944.3		***				
Catenin alpha-1	CTNNA1	NM_001903.5	***	***	*	*		
Catenin alpha-2	CTNNA2	NM_001282597.3	***	***	**	**	***	*
Catenin alpha-3	CTNNA3	NM_013266.4	***	***	***	**	**	***
Catenin beta-1	CTNNB1	NM_001904.4		***				
Catenin delta-1	CTNND1	NM_001085458.2	***	**				
Src substrate cortactin	CTTN	NM_005231.4	***	***	*	**		*
Junction plakoglobin	JUP	NM_002230.4						
Afadin	MLLT4	NM_001386888.1	**	***	*			
Nectin-1	PVRL1	NM_002855.5	***	***	*			
Nectin-2	PVRL2	NM_001042724.2		***				
Nectin-3	PVRL3	NM_015480.3	***	*	*			
Nectin-3	PRR3	NM_025263.4	***	***				
Nectin-4	PRR4	NM_007244.3	***	***				
Wiskott-Aldrich syndrome protein	WAS	NM_000377.3	***	***	**	**		**

Vasodilator-stimulated phosphoprotein	**VASP**	**NM_003370.4**	*	*	***	***	***	*
Merlin	NF2	NM_000268.4	***	*		*		
Vinculin	VCL	NM_014000.3	*	*	**	*	*	
Tight-junction protein ZO-1	TJP1	NM_001330239.4		***				
Actin-related protein 2	ACTR2	NM_005722.4		***				
Actin-related protein 3	ACTR3	NM_005721.5		***				

Expression: Expression of genes in HCC compared to expression in non-tumorous Liver (Mann-Whitney U test). Survival: Correlation of gene expression in HCC with patient survival (Log-rank test). Correlation: Correlation of gene expression in HCC with YAP target gene (CIN4) expression (Spearman correlation). Green marked areas indicate intersecting set of genes, which were selected for further selection steps. The selected candidates are bold. * $P \leq 0.05$, ** $P \leq 0.01$, *** $P \leq 0.001$.

Supplement Table 2: Relevant BioID targets of DSG1 after selection.

Rank	Gene names	Protein names	Protein ID	Log_2 fc	$-Log_{10}$ *P*
1	DSG1	Desmoglein-1	Q02413	11,641	5,698
2	EPS8	Epidermal growth factor receptor kinase substrate 8	Q12929	5,009	2,942
3	FRMPD3	FERM and PDZ domain-containing protein 3	Q5JV73	4,669	3,052
4	BAIAP2	Brain-specific angiogenesis inhibitor 1-associated protein 2	Q9UQB8	4,526	2,734
5	BAIAP2L1	Brain-specific angiogenesis inhibitor 1-associated protein 2-like protein 1	Q9UHR4	4,405	2,567
6	VBP1	Prefoldin subunit 3	P61758	4,194	2,215
7	HIST2H3A	Histone H3.2	Q71DI3	3,878	2,202
8	SNX6	Sorting nexin-6	Q9UNH7	3,856	2,657
9	MB21D2	Protein MB21D2	Q8IYB1	3,787	2,526
10	RIPK1	Receptor-interacting serine/threonine-protein kinase 1	Q13546	3,521	3,638
11	SH3RF2	Putative E3 ubiquitin-protein ligase SH3RF2	Q8TEC5	3,360	2,664
12	PAK4	Serine/threonine-protein kinase PAK 4	O96013	3,217	2,016
13	TNRC6A	Trinucleotide repeat-containing gene 6A protein	Q8NDV7	2,958	2,032
14	UBASH3B	Ubiquitin-associated and SH3 domain-containing protein B	Q8TF42	2,933	1,895
15	POC1B	POC1 centriolar protein homolog B	Q8TC44	2,922	1,899
16	TNRC6B	Trinucleotide repeat-containing gene 6B protein	Q9UPQ9	2,899	1,765
17	PKP4	Plakophilin-4	Q99569	2,847	1,584
18	USP54	Inactive ubiquitin carboxyl-terminal hydrolase 54	Q70EL1	2,839	1,928
19	PFDN6	Prefoldin subunit 6	O15212	2,731	1,608
20	RAB11FIP1	Rab11 family-interacting protein 1	Q6WKZ4	2,554	1,845
21	NOL6	Nucleolar protein 6	Q9H6R4	2,478	2,531
22	SCYL2	SCY1-like protein 2	Q6P3W7	2,449	2,063
23	SNX5	Sorting nexin-5	Q9Y5X3	2,339	2,819
24	BMP2K	BMP-2-inducible protein kinase	Q9NSY1	2,327	1,524
25	XRN1	5-3 exoribonuclease 1	Q8IZH2	2,324	1,688

26	CCDC8	Coiled-coil domain-containing protein 8	Q9H0W5	2,274	2,117
27	TAB2	TGF-beta-activated kinase 1 and MAP3K7-binding protein 2	Q9NYJ8	2,102	1,861
28	YEATS2	YEATS domain-containing protein 2	Q9ULM3	2,072	2,358
29	DNAJB6	DnaJ homolog subfamily B member 6	O75190	1,879	1,858
30	KIRREL	Kin of IRRE-like protein 1	Q96J84	1,859	1,464
31	PLK1	Serine/threonine-protein kinase PLK1	P53350	1,766	1,430
32	XPR1	Xenotropic and polytropic retrovirus receptor 1	Q9UBH6	1,720	1,376
33	MAGEC2	Melanoma-associated antigen C2	Q9UBF1	1,713	1,893
34	GOLGA5	Golgin subfamily A member 5	Q8TBA6	1,611	1,685
35	SRGAP2B	SLIT-ROBO Rho GTPase-activating protein 2B	P0DMP2	0,810	1,355
36	EIF2S3	Eukaryotic translation initiation factor 2 subunit 3	P41091	0,791	1,737

Supplement Table 3: Relevant BioID targets of DSG2 after selection.

Rank	Gene names	Protein names	Protein ID	Log_2 fc	$-Log_{10}$ *P*
1	SHC1	SHC-transforming protein 1	P29353	5.104	3.703
2	SNAP29	Synaptosomal-associated protein 29	O95721	3.836	3.680
3	ANKS1A	Ankyrin repeat and SAM domain-containing protein 1A	Q92625	3.743	3.347
4	YKT6	Synaptobrevin homolog YKT6	O15498	3.299	2.268
5	SLC3A2	4F2 cell-surface antigen heavy chain	P08195	3.116	1.511
6	VPS13B	Vacuolar protein sorting-associated protein 13B	Q7Z7G8	3.046	2.650
7	ROBO1	Roundabout homolog 1	Q9Y6N7	2.911	3.694
8	TNKS1BP1	182 kDa tankyrase-1-binding protein	Q9C0C2	2.837	1.851
9	RDX	Radixin	P35241	2.818	2.477
10	TP53BP2	Apoptosis-stimulating of p53 protein 2	Q13625	2.723	2.583
11	EHD1/3	EH domain-containing protein 1/3	Q9H4M9;Q9NZN3	2.722	3.886
12	CXADR	Coxsackievirus and adenovirus receptor	P78310	2.702	1.850
13	CD44	CD44 antigen	P16070	2.614	2.195
14	SEP06	Septin-6	Q14141	2.576	2.997
15	TKT	Transketolase	P29401	2.568	2.047
16	CSE1L	Exportin-2	P55060	2.527	1.173
17	AKAP2	A-kinase anchor protein 2	Q9Y2D5	2.400	1.958
18	LGALS1	Galectin-1	P09382	2.357	3.848
19	SIPA1L3	Signal-induced proliferation-associated 1-like protein 3	O60292	2.288	2.013
20	REPS1	RalBP1-associated Eps domain-containing protein 1	Q96D71	2.240	2.606
21	SLITRK4	SLIT and NTRK-like protein 4	Q8IW52	2.217	1.919
22	KIAA1522	Uncharacterized protein KIAA1522	Q9P206	2.152	1.373
23	CTNNB1	Catenin beta-1	P35222	2.149	2.335
24	DOCK7	Dedicator of cytokinesis protein 7	Q96N67	2.140	2.269
25	SLC7A5	Large neutral amino acids transporter small subunit 1	Q01650	2.027	2.662
26	ARHGAP39	Rho GTPase-activating protein 39	Q9C0H5	2.001	1.198
27	CEP89	Centrosomal protein of 89 kDa	Q96ST8	1.937	1.416
28	RAPGEF6	Rap guanine nucleotide exchange factor 6	Q8TEU7	1.885	1.506
29	DCBLD2	Discoidin. CUB and LCCL domain-containing protein 2	Q96PD2	1.824	1.621
30	DENND4C	DENN domain-containing protein 4C	Q5VZ89	1.798	1.451

31	PSD3	PH and SEC7 domain-containing protein 3	Q9NYI0	1.748	1.588
32	BCAR1	Breast cancer anti-estrogen resistance protein 1	P56945	1.726	1.595
33	SHB	SH2 domain-containing adapter protein B	Q15464	1.717	1.165
34	PACS1	Phosphofurin acidic cluster sorting protein 1	Q6VY07	1.633	3.672
35	**LATS2**	**Serine/threonine-protein kinase LATS2**	**Q9NRM7**	**1.626**	**1.298**
36	LDHA	L-lactate dehydrogenase A chain	P00338	1.517	1.281
37	CDC42BPB	Serine/threonine-protein kinase MRCK beta	Q9Y5S2	1.433	2.041
38	RASSF7	Ras association domain-containing protein 7	Q02833	1.382	1.233
39	**NF2**	**Merlin**	**P35240**	**1.303**	**1.252**
40	GAB1	GRB2-associated-binding protein 1	Q13480	1.297	1.298
41	FRMD4A	FERM domain-containing protein 4A	Q9P2Q2	1.235	1.230
42	CRK	Adapter molecule crk	P46108	1.192	2.163
43	INADL	InaD-like protein	Q8NI35	1.167	2.024
44	AHNAK	Neuroblast differentiation-associated protein AHNAK	Q09666	1.129	2.893

Supplement Table 4: The 150 most abundant targets of VASP after selection.

Rank	Gena name	Protein name	Protein ID	Log_2 fc		$-Log_{10}$ *P*	
				VASP-N	VASP-C	VASP-N	VASP-C
1	VASP	Vasodilator-stimulated phosphoprotein	P50552	10.251	10.608	7.332	6.052
2	ENAH	Protein enabled homolog	Q8N8S7	8.890	9.054	5.802	5.896
3	RAPH1	Ras-associated and pleckstrin homology domains-containing protein 1	Q70E73	8.866	7.377	7.057	5.971
4	PALLD	Palladin	Q8WX93	9.742	7.026	7.101	5.489
5	DNMBP	Dynamin-binding protein	Q6XZF7	7.663	7.462	5.230	4.615
6	LPP	Lipoma-preferred partner	Q93052	8.766	6.868	5.163	4.490
7	TRIM9	E3 ubiquitin-protein ligase TRIM9	Q9C026	6.929	7.136	5.665	5.410
8	TRIM67	Tripartite motif-containing protein 67	Q6ZTA4	7.438	6.503	5.078	4.652
9	CYFIP1	Cytoplasmic FMR1-interacting protein 1	Q7L576	8.455	6.044	5.888	4.566
10	ZYX	Zyxin	Q15942	7.921	5.603	4.899	3.839
11	SYNPO	Synaptopodin	Q8N3V7	7.357	5.786	6.144	4.742
12	SH3KBP1	SH3 domain-containing kinase-binding protein 1	Q96B97	6.464	6.230	4.557	3.973
13	NHS	Nance-Horan syndrome protein	Q6T4R5	6.714	5.909	6.180	4.642
14	FGFR1OP	FGFR1 oncogene partner	O95684	5.756	8.415	6.677	6.215
15	APBB1IP	Amyloid beta A4 precursor protein-binding family B member 1-interacting protein	Q7Z5R6	6.737	5.334	5.591	4.898

16	CPSF3	Cleavage and polyadenylation specificity factor subunit 3	Q9UKF6	5.944	6.093	6.038	5.233
17	TJP2	Tight junction protein ZO-2	Q9UDY2	6.807	5.188	6.356	4.585
18	VCL	Vinculin	P18206	8.504	4.699	5.203	3.370
19	LIMD1	LIM domain-containing protein 1	Q9UGP4	6.284	5.003	6.390	4.524
20	ECD	Protein SGT1	O95905	5.594	6.376	4.681	4.539
21	PDLIM5	PDZ and LIM domain protein 5	Q96HC4	6.137	4.655	4.948	3.842
22	DBNL	Drebrin-like protein	Q9UJU6	6.443	4.461	6.114	3.932
23	XIRP2	Xin actin-binding repeat-containing protein 2	A4UGR9	5.625	5.222	3.403	3.523
24	KIAA1522	Uncharacterized protein KIAA1522	Q9P206	6.544	4.383	6.275	4.351
25	SHANK2	SH3 and multiple ankyrin repeat domains protein 2	Q9UPX8	6.443	4.411	6.904	3.072
26	ABLIM1	Actin-binding LIM protein 1	O14639	5.925	4.601	5.917	4.414
27	ARHGAP35	Rho GTPase-activating protein 35	Q9NRY4	5.714	4.830	3.984	3.739
28	INPPL1	Phosphatidylinositol 3,4,5-trisphosphate 5-phosphatase 2	O15357	5.530	4.841	4.694	3.780
29	MLLT4	Afadin	P55196	5.790	4.351	5.491	4.024
30	SVIL	Supervillin	O95425	5.911	4.319	3.118	2.341
31	CAMSAP1	Calmodulin-regulated spectrin-associated protein 1	Q5T5Y3	5.625	4.440	4.426	3.225
32	PXN	Paxillin	P49023	5.215	5.255	3.709	3.654
33	DBN1	Drebrin	Q16643	5.740	4.293	4.452	3.604
34	TP53BP2	Apoptosis-stimulating of p53 protein 2	Q13625	5.871	4.151	4.498	3.168
35	SYNJ2	Synaptojanin-2	O15056	5.969	3.909	3.408	2.315
36	CEP55	Centrosomal protein of 55 kDa	Q53EZ4	5.288	4.536	4.230	4.092
37	IRAK1	Interleukin-1 receptor-associated kinase 1	P51617	5.598	4.073	6.175	3.941
38	DLGAP5	Disks large-associated protein 5	Q15398	5.452	4.217	6.024	4.043
39	PPP6R3	Serine/threonine-protein phosphatase 6 regulatory subunit 3	Q5H9R7	5.456	4.201	4.401	4.287
40	ACTN4	Alpha-actinin-4	O43707	5.492	4.130	3.658	2.766
41	TJP1	Tight junction protein ZO-1	Q07157	5.385	4.241	5.173	3.909
42	CTNND1	Catenin delta-1	O60716	5.574	4.002	4.706	3.486
43	ATG2B	Autophagy-related protein 2 homolog B	Q96BY7	4.681	5.415	3.532	3.865
44	UBASH3B	Ubiquitin-associated and SH3 domain-containing protein B	Q8TF42	5.124	4.380	4.507	3.636

45	RIPK1	Receptor-interacting serine/threonine-protein kinase 1	Q13546	4.728	5.089	5.292	4.580
46	ABI1	Abl interactor 1	Q8IZP0	5.443	3.881	5.894	3.216
47	RTN3	Reticulon-3	O95197	4.452	5.914	2.863	4.509
48	WASF2	Wiskott-Aldrich syndrome protein family member 2	Q9Y6W5	6.612	3.386	5.036	2.637
49	STAT2	Signal transducer and activator of transcription 2	P52630	4.655	4.447	4.494	3.939
50	PAK2	Serine/threonine-protein kinase PAK 2;PAK-2p27;PAK-2p34	Q13177	5.411	3.767	5.525	3.689
51	XIAP	E3 ubiquitin-protein ligase XIAP	P98170	4.841	4.252	4.597	3.667
52	LRRC16A	Leucine-rich repeat-containing protein 16A	Q5VZK9	5.485	3.678	4.709	3.274
53	TNS3	Tensin-3	Q68CZ2	5.014	3.992	3.384	2.648
54	LMO7	LIM domain only protein 7	Q8WWI1	5.056	3.882	3.323	2.476
55	SYNJ1	Synaptojanin-1	O43426	5.038	3.893	4.573	3.837
56	PTPN13	Tyrosine-protein phosphatase non-receptor type 13	Q12923	4.616	4.265	3.909	3.234
57	NPLOC4	Nuclear protein localization protein 4 homolog	Q8TAT6	4.558	4.327	4.593	3.952
58	DFNA5	Non-syndromic hearing impairment protein 5	O60443	5.307	3.628	5.373	3.568
59	BCAR1	Breast cancer anti-estrogen resistance protein 1	P56945	5.123	3.730	5.277	3.414
60	PPP1R13L	RelA-associated inhibitor	Q8WUF5	5.325	3.565	6.223	2.363
61	MB21D2	Protein MB21D2	Q8IYB1	4.898	3.816	5.837	4.420
62	BRAP	BRCA1-associated protein	Q7Z569	4.586	4.220	4.925	4.053
63	KANK2	KN motif and ankyrin repeat domain-containing protein 2	Q63ZY3	4.626	4.127	3.254	2.695
64	PTPN14	Tyrosine-protein phosphatase non-receptor type 14	Q15678	5.719	3.167	4.700	2.593
65	SCRIB	Protein scribble homolog	Q14160	5.218	3.548	6.036	3.183
66	EPS15	Epidermal growth factor receptor substrate 15	P42566	4.927	3.692	5.251	3.771
67	EHBP1	EH domain-binding protein 1	Q8NDI1	5.607	3.164	5.624	3.259
68	PDLIM7	PDZ and LIM domain protein 7	Q9NR12	5.305	3.409	4.005	2.700
69	STRAP	Serine-threonine kinase receptor-associated protein	Q9Y3F4	4.524	4.091	3.800	4.145

70	MYLK	Myosin light chain kinase, smooth muscle	Q15746	5.055	3.559	4.797	3.437
71	HBS1L	HBS1-like protein	Q9Y450	4.476	3.903	3.060	2.877
72	ARFGAP1	ADP-ribosylation factor GTPase-activating protein 1	Q8N6T3	4.651	3.726	3.363	2.796
73	SNX9	Sorting nexin-9	Q9Y5X1	5.732	2.860	6.098	3.299
74	PSMD2	26S proteasome non-ATPase regulatory subunit 2	Q13200	3.907	5.045	2.890	3.334
75	CCDC88A	Girdin	Q3V6T2	4.852	3.416	4.493	2.136
76	NHLRC2	NHL repeat-containing protein 2	Q8NBF2	4.637	3.589	4.874	3.477
77	C1orf198	Uncharacterized protein C1orf198	Q9H425	4.707	3.434	5.885	3.458
78	PEAK1	Pseudopodium-enriched atypical kinase 1	Q9H792	4.529	3.670	5.278	3.342
79	LIMA1	LIM domain and actin-binding protein 1	Q9UHB6	4.884	3.301	4.125	2.988
80	ARHGEF28	Rho guanine nucleotide exchange factor 28	Q8N1W1	3.827	4.682	3.339	3.224
81	PARD3	Partitioning defective 3 homolog	Q8TEW0	5.050	3.049	4.364	2.741
82	FAM21A	WASH complex subunit FAM21A	Q641Q2	3.917	4.263	4.288	3.012
83	CLMN	Calmin	Q96JQ2	3.622	4.717	2.421	2.952
84	AARS	Alanine--tRNA ligase, cytoplasmic	P49588	3.992	3.895	4.089	3.645
85	ACTN1	Alpha-actinin-1	P12814	4.175	3.808	5.052	3.751
86	SH3GL1	Endophilin-A2	Q99961	4.685	3.224	3.782	2.401
87	AAK1	AP2-associated protein kinase 1	Q2M2I8	4.773	3.110	5.228	3.360
88	FAM135A	Protein FAM135A	Q9P2D6	4.350	3.630	4.718	3.637
89	PPP1R18	Phostensin	Q6NYC8	5.187	2.767	5.855	2.480
90	TMOD3	Tropomodulin-3	Q9NYL9	4.440	3.441	4.806	3.319
91	PPP2R3A	Serine/threonine-protein phosphatase 2A regulatory subunit B subunit alpha	Q06190	4.467	3.402	4.283	3.039
92	REPS1	RalBP1-associated Eps domain-containing protein 1	Q96D71	6.111	2.302	5.766	2.880
93	KIAA1524	Protein CIP2A	Q8TCG1	4.670	2.978	4.021	3.046
94	MICAL3	Protein-methionine sulfoxide oxidase MICAL3	Q7RTP6	4.591	3.097	5.326	3.334
95	TWF2	Twinfilin-2	Q6IBS0	4.700	2.909	4.426	2.889
96	R3HCC1L	Coiled-coil domain-containing protein R3HCC1L	Q7Z5L2	4.035	3.622	4.989	3.713
97	SCYL3	Protein-associating with the carboxyl-terminal domain of ezrin	Q8IZE3	3.896	3.830	3.428	3.149

98	TNKS1BP1	182 kDa tankyrase-1-binding protein	Q9C0C2	4.720	2.775	3.858	1.845
99	PKN2	Serine/threonine-protein kinase N2	Q16513	3.955	3.662	4.314	3.284
100	MRE11A	Double-strand break repair protein MRE11A	P49959	4.419	3.117	3.632	2.377
101	DLG5	Disks large homolog 5	Q8TDM6	4.200	3.214	3.394	2.579
102	ARFGAP3	ADP-ribosylation factor GTPase-activating protein 3	Q9NP61	4.158	3.276	4.531	3.409
103	KIF5B	Kinesin-1 heavy chain	P33176	4.541	2.789	3.444	2.272
104	EIF4H	Eukaryotic translation initiation factor 4H	Q15056	3.747	3.719	4.261	3.784
105	TES	Testin	Q9UGI8	4.449	2.875	3.654	2.502
106	SPAG5	Sperm-associated antigen 5	Q96R06	3.929	3.432	3.234	2.698
107	TNRC6B	Trinucleotide repeat-containing gene 6B protein	Q9UPQ9	5.399	2.151	6.005	1.933
108	CACYBP	Calcyclin-binding protein	Q9HB71	3.456	3.779	3.244	3.302
109	DVL2	Segment polarity protein dishevelled homolog DVL-2	O14641	3.774	3.557	2.328	1.987
110	SNAP29	Synaptosomal-associated protein 29	O95721	4.183	2.926	3.044	2.322
111	PDLIM1	PDZ and LIM domain protein 1	O00151	4.519	2.684	4.174	2.562
112	CNN3	Calponin-3	Q15417	5.148	2.188	4.581	1.708
113	YTHDF2	YTH domain-containing family protein 2	Q9Y5A9	3.443	3.770	4.785	4.452
114	LSG1	Large subunit GTPase 1 homolog	Q9H089	1.783	6.391	2.138	5.005
115	DENND4C	DENN domain-containing protein 4C	Q5VZ89	3.909	3.196	4.591	3.065
116	CIAPIN1	Anamorsin	Q6FI81	4.790	2.318	4.519	1.556
117	MAP4K4	Mitogen-activated protein kinase kinase kinase kinase 4	O95819	4.425	2.677	4.327	2.693
118	**YAP1**	**Transcriptional coactivator YAP1**	**P46937**	**4.842**	**2.299**	**5.803**	**4.183**
119	ANKRD17	Ankyrin repeat domain-containing protein 17	O75179	4.978	2.211	5.312	1.894
120	ALMS1	Alstrom syndrome protein 1	Q8TCU4	3.213	3.858	2.465	2.215
121	TFCP2	Alpha-globin transcription factor CP2	Q12800	2.165	4.899	4.520	4.404
122	HS1BP3	HCLS1-binding protein 3	Q53T59	3.963	2.957	3.591	2.410
123	TAB2	TGF-beta-activated kinase 1 and MAP3K7-binding protein 2	Q9NYJ8	4.384	2.673	4.818	2.576
124	ANKHD1	Ankyrin repeat and KH domain-containing protein 1	Q8IWZ3	4.462	2.542	5.116	2.844
125	PRMT7	Protein arginine N-methyltransferase 7	Q9NVM4	4.422	2.614	2.746	1.603

126	ABR	Active breakpoint cluster region-related protein	Q12979	1.645	5.713	1.255	3.586
127	USP15	Ubiquitin carboxyl-terminal hydrolase 15	Q9Y4E8	3.949	2.902	3.176	2.450
128	SUGT1	Suppressor of G2 allele of SKP1 homolog	Q9Y2Z0	2.997	3.861	3.283	4.295
129	NUMB	Protein numb homolog	P49757	4.002	2.728	5.470	3.588
130	BUB1B	Mitotic checkpoint serine/threonine-protein kinase BUB1 beta	O60566	3.443	3.379	3.817	2.932
131	STRN4	Striatin-4	Q9NRL3	3.975	2.743	4.533	3.115
132	ARHGEF10	Rho guanine nucleotide exchange factor 10	O15013	1.497	5.213	2.170	4.329
133	NUDC	Nuclear migration protein nudC	Q9Y266	3.900	2.868	4.524	4.095
134	IGBP1	Immunoglobulin-binding protein 1	P78318	3.972	2.748	3.728	2.332
135	KIF11	Kinesin-like protein KIF11	P52732	3.415	3.373	3.748	3.083
136	RIC8A	Synembryn-A	Q9NPQ8	3.871	2.854	4.305	3.225
137		Uncharacterized protein FLJ45252	Q6ZSR9	4.343	2.389	5.452	2.499
138	AFAP1L2	Actin filament-associated protein 1-like 2	Q8N4X5	4.099	2.478	3.602	2.209
139	PASK	PAS domain-containing serine/threonine-protein kinase	Q96RG2	1.852	4.259	1.002	2.579
140	ABI2	Abl interactor 2	Q9NYB9	3.184	3.396	4.520	3.669
141	LASP1	LIM and SH3 domain protein 1	Q14847	4.292	2.305	6.221	2.951
142	ANKS1A	Ankyrin repeat and SAM domain-containing protein 1A	Q92625	5.073	1.683	4.005	2.035
143	SYNRG	Synergin gamma	Q9UMZ2	3.740	2.799	3.080	2.068
144	PTPN12	Tyrosine-protein phosphatase non-receptor type 12	Q05209	4.560	2.047	4.647	1.912
145	FGD6	FYVE, RhoGEF and PH domain-containing protein 6	Q6ZV73	4.049	2.394	5.298	3.056
146	DAB2	Disabled homolog 2	P98082	3.987	2.435	4.031	2.516
147	AKAP13	A-kinase anchor protein 13	Q12802	2.255	3.814	3.612	2.004
148	AGFG1	Arf-GAP domain and FG repeat-containing protein 1	P52594	4.055	2.338	3.666	2.435
149	NUDT5	ADP-sugar pyrophosphatase	Q9UKK9	3.099	3.362	2.134	2.901
150	MIB1	E3 ubiquitin-protein ligase MIB1	Q86YT6	4.963	1.587	5.224	1.687